UTS UNIVERSITY OF TECHNOLOGY SYDNEY

Hyphenated Elemental Mass Spectrometry for the Biosciences

by Sarah Meyer

Thesis submitted in fulfilment of the requirements for the degree of

Doctor of Philosophy: Science

under the supervision of Dist. Prof. Philip Doble, Dr. David Bishop, Dr. David Clases, and Dr. Raquel Gonzalez de Vega

University of Technology Sydney
Faculty of Science

July 2022

Certificate of Authorship

I, Sarah Meyer, declare that this thesis is submitted in fulfilment of the requirements for the award of Doctor of Philosophy: Science, in the Faculty of Science at the University of Technology Sydney.

This thesis is wholly my own work unless otherwise referenced or acknowledged. In addition, I certify that all information sources and literature used are indicated in the thesis.

This document has not been submitted for qualifications at any other academic institution.

This research is supported by the Australian Government Research Training Program.

Signature: Production Note:
Signature removed prior to publication.

Date: 19th of July 2022

Acknowledgements

I would like to thank all the people who supported, motivated, and inspired me along my path and who contributed to this work in multiple ways.

First, I would like to thank my supervisor Dist. Prof. Philip Doble for the opportunity to do my PhD in Australia in his group. Thank you for being a great mentor and supervisor, for your support, advice, and encouragements, for teaching me everything about CE, the challenging projects, and your funny and charismatic nature. I am very grateful for the last 3.5 years and have developed myself so much, both scientifically and personally.

Moreover, I would like to acknowledge my supervisors David Bishop, David Clases and Raquel Gonzalez de Vega. Dave – thank you for supporting me with all imaging and ICP-MS questions, and especially for being a great supervisor during my first visit that inspired me to come back to UTS for my PhD. David – for motivations and encouragements, for scientific and personal discussions, for teaching me everything you know, especially about single particle ICP-MS and ICP-MS operation modes, and last but not least for being a great friend. My experience at UTS would not have been the same without you. Raquel – for all the meetings, support, and advice, for always being available for me, for being a competent advisor for everything that has to do with immunohistochemistry, and for your friendship. I miss and wish you all the best for your future.

I would like to make a special mention to Ariane Roseblade, Matt Padula and technical staff members Anthea Harris, Dayanne Bordin and Tom Lockwood. Ariane – for being a great, fun, and smart person to be around, for bouncing ideas off each other, and for having a similar obsession with pretty Origin figures and

Excel spreadsheets. Matt – for your support in the protein project and for providing me with protein standards and surfactants. Anthea, Dayanne and Tom – for keeping the instruments running in the teaching and research labs, for somehow always finding spare parts or rare chemical equipment that is useful for my research, and for your willingness to help in many situations.

Furthermore, I gratefully acknowledge the philanthropic support from George Miklos and the Miklos Family.

Thank you to the members of the research group: David G., Dylan, Jacob, Jake, Karen, Monique, Prashina, Siobhan, and Tash for all the good times and making me feel welcome. I would like to mention Mika and Tom especially for the scientific discussions, regular check-ins, for your help, and all the restaurant and bar recommendations.

A special thank you to my fellow PhDs at UTS: Alisha, Amber, Ana, Blake, Brooke, Caleb, Camilla, Ciara, Dan, Eda, Edward, Freddy, Helen, Minh, Oksana, Sandi, Sharni, Simon, and Tom G. for the lunch breaks, birthday cakes, wine dates, picnics, good chats, weekend get-aways, being there in challenging times, and for making me feel so welcome even though I am such a busy bee running around.

I would further like to acknowledge Prof. Dr. Uwe Karst for inspiring me to get into analytical chemistry and for supporting me along my way, as well as my fellow students from Münster: Arne, Carina, Jordi, Patrick B., Patrick H., Niklas, Sabsi and Sommel for making the time in Münster so valuable and being the best friends I could wish for.

Thank you to all my friends outside from uni, specifically Aileen, Jessica M, Maike and Naomi - I know I can count on you and call at any time, in any situation.

A huge thank you goes to Diane and Van Wallace for your acceptance, interest, support, and being my Australian family. I don’t take this for granted and really appreciate you both.

Mein größter Dank gehört meiner Familie: meinem Bruder Nicolas, meinen Eltern Martina und Norbert Meyer sowie meine Großeltern Elfriede und Ewald Meyer, und Gerta und Josef Becker. Ich weiß, es nicht einfach für euch ist, dass ich nach Australien gegangen und daher ich bin euch dankbar, dass ihr mich meinen Weg gehen lasst. Ohne euch und eure Unterstützung wäre diese Arbeit nicht möglich gewesen. Danke für das Vertrauen, den bedingungslosen Rückhalt und eure Fürsorge. Euch ist diese Arbeit gewidmet.

Finally, I would like to thank my partner Cheyne Wallace, who has been an unwavering support since the day I have met you. You have such amazing listening and problem-solving skills, and often a great answer for all kinds of questions. Thanks for your encouragements, understanding, for showing me the fun side of life, and accepting me as the person I am. As they say in Bondi: “You are my rock, babe.”

List of Publications

Sarah Meyer, David Clases, and Philip A. Doble, *A Simple, Low-Cost and Robust CE-ICP-MS Interface for the Analysis of Gadolinium-based Contrast Agents in Biological Samples*, in preparation.

Sarah Meyer, David Clases, Raquel Gonzalez de Vega, Matthew P. Padula and Philip A. Doble, *Separation of Intact Proteins by Capillary Electrophoresis*, Analyst (**2022**), 147, 13, 2988-2996.

Sarah Meyer, Raquel Gonzalez de Vega, Xiaoxue Xu, Ziqing Du, Philip A. Doble, and David Clases, *Characterisation of Upconversion Nanoparticles by Single-Particle ICP-MS Employing a Quadrupole Mass Filter with Increased Bandpass*, Anal. Chem. (**2020**), 92, 22, 15007–15016.

Sarah Meyer, Callum Clarke, Robson Oliveira dos Santos, David Bishop, Marco A. Krieger and Lucas Blanes, *Developing self-generated calibration curves using a capillary-driven wax-polyester lab on a chip device and thermal gates*, Microchemical Journal 146 (**2019**) 709-712.

“Studies derived from manganese-based atomic research have resulted in a profound new understanding of cancer radiotherapy. The data obtained are totally unexpected. They are of fundamental importance and will certainly have deep implications for patient treatment.”

Edmond H. Fisher

Nobel prize in Physiology and Medicine, 1992

Table of Contents

List of Figures

List of Tables

Abbreviations

A1 β-CN	A1 β-casein
A2 β-CN	A2 β-casein
α-CN	α-casein
α-Lac A	α-lactalbumin a
BFS	bare fused silica capillaries
BGE	background electrolyte
BPM	bandpass mode
BSA	bovine serum albumin
β-Lg	β-lactoglobulin
β-Lg A	β-lactoglobulin a
β-Lg B	β-lactoglobulin b
CA	citric acid
CE	capillary electrophoresis
CEI	capillary electrophoresis interface
CIC	compound-independent calibration

CK	creatine kinase
CMC	critical micellar concentration
CTAB	cetyltrimethylammonium bromide
DC	direct current
DIHEN	direct injection high efficiency nebulizer
DMT1	divalent metal transporter 1
DNA	deoxyribonucleic acid
DOTA	1,4,7,10-tetraazacyclododecane-1,4,7,10-tetraacetic acid
DTPA	diethylenetriaminepentaacetic acid
DTTA	diethylenetriaminetetra-acetic acid
EBI	elemental bioimaging
EOF	electroosmotic flow
Fab	fragment antigen binding
Fc	fragments crystallizable
FFT	fast fourier transform
Fpn	ferroportin
FWHM	Full width at half maximum
GBCA	gadolinium-based contrast agent
Gd-BT-DO3A	gadobutrol (Gadovist®)
Gd-DOTA	gadoteric acid (Dotarem®)

Gd-DTPA	gadopentetic acid (Magnevist®)
Gd-DTPA-BMA	gadodiamide (Omniscan®)
Gd-EOB-DTPA	gadoxetic acid (Primovist®)
GC	gas chromatography
His	histidine
HPLC	high performance liquid chromatography
HPMC	hydroxypropylmethylcellulose
HSA	human serum albumin
ICP-MS	inductively coupled plasma-mass spectrometry
IgG	sheep igg antibody
IHC	immunohistochemistry
iMSI	immuno-mass spectrometry imaging
IR	ionising radiation
LA	laser ablation
LOD	limit of detection
LOQ	limit of quantification
m/z	mass-to-charge ratio
Mb	myoglobin
MeCAT	metal coded affinity tags
MRI	magnetic resonance imaging

MW	molecular weight
NCX	sodium-calcium exchanger
NP	nanoparticle
NRAMP	natural resistance-associated macrophage protein
NSF	nephrogenic systemic fibrosis
OIO	optimised ion optics
PBS	phosphate buffered saline
PDMS	dimethyl polysiloxane
pI	isoelectric point
PM	plasma membrane
RF	radio frequency
RNase	ribonuclease a
ROI	regions of interest
ROS	reactive oxygen species
rpm	revolutions per minute
RSD	relative standard deviation
sDL	size detection limit
SDS	sodium dodecyl sulfate
SEC	size exclusion chromatography
SLG	scan line gain

SLS	scan line slope
SM	standard mode
SMIL	successive multiple ionic polymer layers
SP	single-particle
SQ or Q	single quadrupole
TEM	transmission electron microscopy
Tf	transferrin
TfR	transferrin receptor
TQ or QQQ	triple quadrupole
TRIS	tris(hydroxymethyl)aminomethan
UCNPs	upconversion nanoparticles
UV	ultraviolet
ZIP	zrt- and irt-like proteins
ZnT10	zinc transporter 10

Abstract

The underlying biological mechanisms of widespread radioresistance of many human tumours remain elusive despite decades of investigations. Research efforts have largely focussed on the genomics/proteomics-based enzymology of DNA repair and free radical scavenging enzymes such as the superoxide dismutases. A recent novel hypothesis is that radiation resistance is predominantly underpinned by non-enzymatic complexes of manganese and small molecular metabolites. These complexes are thought to act as free radical scavengers which provide metabolic radioprotection that render cells variably resistant to the products of ionising radiation.

Multiple influx and efflux metal transporters are involved in manganese homeostasis and are potentially differentially expressed on the surface of cancer cells, leading to variable concentrations of manganese within tumours. Uncovering the mechanisms of tumour radioresistance requires complementary, reliable, and well characterised methods to spatially quantify manganese and its transporter proteins. Laser ablation-inductively coupled plasma-mass spectrometry (LA-ICP-MS) provides a single technological platform to construct quantified images of elements and may be extended to measure biomolecules via incorporation of immunoassays. However, high quality and reproducible analyses require quality assurance across all steps of the workflow including the characterisation of antibodies, nanoparticles and antibody tagging protocols. Accordingly, this thesis introduces a portfolio of methods of hyphenated ICP-MS for quality assurance of elemental and biomolecule analyses.

Chapter 2 introduces novel and universal workflows for the analysis of intact proteins via capillary electrophoresis (CE) and presents guidelines for the targeted selection of appropriate background electrolytes via consideration of the target proteins' isoelectric point. Neutral dimethyl polysiloxane capillaries with dynamic coatings of cationic cetyltrimethylammonium bromide or anionic sodium dodecyl sulfate, and bare fused silica capillaries were systematically evaluated for the analysis of seven model proteins over a wide pH range. Multiple capillary and background electrolyte combinations were suitable for the analysis of each protein. The concept was demonstrated by the analysis of caseins and whey proteins in milk which separated the most abundant proteins, including the isoforms of A1 and A2 β-casein and β-lactoglobulin A and B.

Chapter 3 presents the development of a simple, robust, and cost-effective interface to hyphenate CE and ICP-MS to enhance the sensitivity and specificity for the analysis of limited volume and complex biological samples. The interface components were thoroughly investigated to highlight crucial aspects that need to be considered when developing and assembling a CE-ICP-MS interface. The interface's functionality, linearity and robustness were evaluated by separation and quantification of gadolinium-based contrast agents in urine samples collected after magnetic resonance imaging (MRI) examination.

Chapter 4 combined these advancements to determine labelling efficiencies of metal conjugated antibodies by CE-ICP-MS, which are widely used in cytometry and imaging for the identification and examination of protein expression. The number of lanthanide ions per protein was measured in seven MAXPAR™ polymer conjugated antibodies. Variable numbers of lanthanides were observed between different antibodies, as well as antibodies of the same kind, highlighting the importance of quality control workflows. The CE-ICP-MS method was also applied to 15 nm gold nanoparticles to demonstrate feasibility to distinguish un-conjugated and antibody conjugated nanoparticles.

Chapter 5 details novel methods of single-particle ICP-MS to characterise the composition, size distribution and particle-particle interactions of (upconversion)

nanoparticles. The optimization of ion extraction, ion transport, and the operation of the quadrupole with increased mass bandwidth improved the signal-to-noise ratios significantly and decreased the size detection limits for all nanoparticle dispersions investigated. Gold nanoparticles were analysed as a model system to demonstrate the effects of increasing ion transmission, subsequently the methods were applied to determine stoichiometries and size distributions of three types of lanthanide-doped upconversion nanoparticles. A Poisson model was further applied to assess particle−particle interactions in the nanoparticle dispersions.

Chapter 6 deployed these advanced techniques to demonstrate immuno-mass spectrometry imaging and elemental bioimaging of manganese transporters and transition metals in human melanomas. The transporter protein ZIP8 was visualised with an ^{153}Eu polymer labelled anti-ZIP8 antibody, and the expression levels of the ZIP14 transporter protein were localised with an immunoassay of an unlabelled primary antibody with a secondary antibody-nanoparticle conjugate. Manganese, copper, zinc, and iron distributions were imaged on consecutive sections of the microarray and co-localised with the ZIP8 and ZIP14 expressions. The results show a variable correlation of transition elements and proteins, demonstrating the complex interplay between metals and their respective transporters.

Chapter 1

Introduction and Scope of the Thesis

1.1 Manganese and tumour radioresistance

1.1.1 Cancer and cancer treatment

Cancer may be defined as a group of diseases arising from uncontrolled growth and division of cells. Malignant tumours can invade surrounding tissues and may spread to distant parts in the body via the bloodstream or the lymphatic system. This process is known as metastasis and accounts for the majority of cancer deaths [1,2].

Successful cancer treatment relies upon early tumour discovery and adequate classification for customised treatment regimens [1]. The four main approaches of treatment are radiotherapy, chemotherapy, immunotherapy, and surgery and can be used individually or in combination. Radiation therapy is the most commonly employed modality and contributes to 40% of all cancer cures [3].

Radiotherapy aims to destroy cancer cells without damaging the surrounding healthy tissue by precise delivery of prescribed doses of ionising radiation (IR). Most patients receive external radio treatment where gamma rays, x-rays or charged particles are delivered to the cancer using linear accelerators and collimators [4]. The radiation source is programmed to move around the body to deliver IR from several directions to minimise exposure to healthy tissue. In the alternative but less commonly used brachytherapy, radioactive pellets are placed into or near the tumour region and delivers high IR doses to the target area [5].

IR damages the deoxyribonucleic acid (DNA) within a cell. This damage may be induced directly through interactions of IR with the DNA itself, causing single and double-strand breaks [6,7]; or indirectly due to the generation of reactive oxygen species (ROS) [8] that react with the DNA. The main ROS formed after radiation are the superoxide radical $O_2^{\bullet -}$, hydrogen peroxide H_2O_2 and the hydroxyl radical $HO^{\bullet -}$. However, the outcome of radiation treatment varies between and within cancer types and although several theories exist, the exact reasons are not known [9].

1.1.2 Manganese and radioresistance

Many cancers are variably resistant to radiotherapy: some patients die within months, while others with the same tumour type and equal radiation treatment, survive for years. A novel and promising hypothesis is that radiation resistance is predominantly caused by non-enzymatic complexes of manganese with small molecular metabolites. These complexes are thought to act as free radical scavengers which provide metabolic radioprotection that render cells variably resistant to the products of IR [9].

The ROS scavenging ability of manganese complexes was first observed by Archibald and Fridovich in 1981 [10]. They reported that *Lactobacillus plantarum* bacteria, which are devoid of superoxide dismutases, showed a resistance to the superoxide radical $O_2^{\bullet-}$. They measured millimolar manganese concentrations within *Lactobacillus plantarum* bacteria and found that the superoxide radical $O_2^{\bullet-}$ scavenging activity was due to Mn(II)-complexes with small molecules present in cells of *Lactobacillus plantarum* [11].

In order to find relations between metal content and radioresistance, Daly *et. al.* undertook a study with *Deinococcus radiodurans* bacteria which are resistant to large doses of IR [12]. They found that the intracellular ratio of manganese to iron was much higher in *Deinococcus radiodurans* compared to radiosensitive bacteria, and that the radioresistance depended on the concentration of Mn^{II} added to the growth media. Furthermore, growing *Deinococcus radiodurans* in the absence of manganese significantly lowered their IR resistance [13].

Krisko and Radman investigated bacterial radioresistance and demonstrated that protein damage was the predominant factor that led to cell death. They explained that *Deinococcus radiodurans* efficiently protected its proteome with complexes of manganese and cytosolic low molecular weight compounds [14]. Other studies have reported that bacteria radioresistance is attained by the non-enzymatic activity of Mn(II)-complexes with small molecules present in the cell including peptides, amino acids, nucleosides, orthophosphate and organic acids [15,16].

The first study specifically targeted to investigate the role of manganese in context with cancer was conducted by Doble and Miklos in 2018 [9]. They spatially analysed the distribution of manganese in tissue sections of seven different cancer types with clinically inferred information on radio responsiveness and patient outcomes by laser ablation-inductively coupled plasma-mass spectrometry (LA-ICP-MS). They found associations between high manganese levels and low patient survival in the most radioresistant cancer types (glioblastoma and melanoma); as well as the opposite scenario, low manganese concentrations and high patient survival in the most radiosensitive tumour types (testis). The full list of investigated tumour types, the clinically inferred radio response and patient survival after radiation treatment is summarised in Table 1-1. Doble and Miklos observed a direct association between manganese levels and radioresponsiveness, whilst no such relation existed for metals like copper, iron, or zinc.

Table 1-1: Clinically inferred radiation responsiveness and patient survival after radiation treatment in different tumour categories [9].

Broad tumour category	**Clinically inferred radiation responsiveness**	**Patient survival after radiation treatment**
Brain	Radioresistant	Low
Mesothelioma	Radioresistant	Low
Melanoma	Radioresistant	Intermediate, variable
Small cell lung	Initially radiosensitive	Low
Breast	Variably radiosensitive	High if tumour localised
Prostate	Variably radiosensitive	High if tumour localised
Testis	Radiosensitive	High

1.1.3 Manganese transporters

Metals are involved in many essential physiological processes in the human body. These are highly regulated and multiple influx and efflux metal transporters are involved in manganese homeostasis. These are potentially differentially expressed on the surface of cancer cells, leading to variable concentrations of manganese within tumours [17,18]. This section provides an overview of manganese influx and efflux transporter proteins that have been identified in the literature.

Cellular manganese influx mechanisms

Several transporter proteins have been shown to be involved in manganese uptake in its divalent oxidation state (Mn^{II}) and include the divalent metal transporter 1 (DMT1), the Zrt- and Irt-like proteins (ZIP) ZIP8 and ZIP14, a

manganese citrate transporter, calcium channels and transporter proteins for the neurotransmitters choline and dopamine. In its trivalent oxidation state (Mn^{III}), the metal ion is presumed to be transported via the transferrin (Tf) mechanism [19].

DMT1. DMT1 (also known as DCT1, NRAMP2 or solute carrier (SLC)11A2) belongs to the family of natural resistance-associated macrophage protein (NRAMP) [20,21] and is named from its capability to transport divalent cations including Fe^{II}, Zn^{II}, Mn^{II}, Co^{II}, Cd^{II}, Cu^{II}, Ni^{II} and Pb^{II} [20,22]. The function of DMT1 as a divalent metal cation transporter was first observed in Belgrade rats [20] and since then several studies have proven the ability for manganese uptake into mammalian cell [18,21,23]. DMT1 is located at the plasma membrane (PM) and the active manganese transport occurs via a proton gradient [18,22,24].

ZIP8 and ZIP14. ZIP8 and ZIP14 are zinc transporter proteins encoded by the SLC39 gene family, comprising of 14 members [25]. While most members only transport zinc, ZIP8 and ZIP14 also transport manganese, iron and cadmium [26]. Knockout studies have shown reduced manganese uptake when ZIP8 and ZIP14 were not expressed [27]. Although these transporter proteins are closely related, differences were observed in the magnitude of manganese transport and the tissue where the proteins were expressed [24]. ZIP8 expression levels were highest in lung, testis and kidney, whereas the highest ZIP14 transcript levels were found in liver, duodenum and kidney [28]. ZIP8 and ZIP14 are located at the PM of cells and both function as divalent ion/bicarbonate symporters, transporting metals across a HCO_3^- gradient [24,25,28].

Citrate, calcium, choline, and dopamine transporters. There is evidence that several other molecules transport Mn^{II}. Manganese citrate crosses the blood-brain-barrier at a much faster rate than can be explained by diffusion, leading to the assumption that a transport mechanism exists where manganese is bound to citrate [23]. Some calcium channels located at the PM of cells were also determined to be permeable to manganese [29–32]. Another possible entrance route for manganese into the brain is using the transporter proteins of the

neurotransmitter choline and dopamine. Both transporters have been shown to be inhibited by manganese [24,33,34].

Transferrin and Transferrin Receptor (TfR). A substantial portion of biological free manganese is transported as Mn^{III} via the Tf mechanism [19,24,35–37]. The glycoprotein Tf is an iron transporter in the blood-plasma and can also carry manganese, although at a much slower rate [37]. The Tf-metal-complex is not able to cross the PM of cells due to its size. The endocytosis occurs by binding iron or manganese to the TfR which is located on the cell surface. Studies suggest a mechanism, where the TfR works along with DMT1. First the pH in the endosome is lowered, inducing the release of Mn^{III} from Tf and its reduction to Mn^{II}. DMT1 then transports Mn^{II} into the cytoplasm [19,24].

Cellular manganese efflux mechanisms

The efflux of Mn^{II} from cells is regulated by various mechanisms, including the zinc transporter 10 (ZnT10), ferroportin (Fpn) and the sodium-calcium exchanger (NCX).

SLC30A10. A third zinc transporter protein involved in manganese homeostasis is ZnT10, which is encoded by the SLC30A10 gene. The SLC30 family consists of ten members, with most of them (SLC30A1-A8) responsible for the transport of zinc from cells. Only SLC30A10 shows evidence to regulate the efflux of manganese from the cytosol to the exterior of the cell [26]. Overexpression studies as well as knockout studies support this assumption, reporting reduced manganese levels due to overexpression of the SLC30A10 gene [38] and evaluated manganese levels caused by loss-of-function mutations in SLC30A10 [26]. The transporter protein is localised at the PM of cells and various studies conclude that SLC30A10 and SLC39A14 (also ZIP14) may act cooperatively to regulate manganese excretion [24,26,39,40].

Ferroportin. Fpn (also known as FPN1, IREG1, MTP1 or SLC40A1) is a transmembrane protein belonging to the ferroportin family [34]. Fpn is

fundamental for eliminating iron from cells and has also been shown to take part in manganese efflux. Decreased intracellular manganese levels were observed in human embryonic kidney cells (HEK293T) after induction of Fpn [41]. These observations were confirmed by investigations of *Xenopus laevis* oocytes that expressed Fpn resulting in lower manganese accumulations [42].

Sodium-calcium exchanger. NCX is an antiporter membrane protein with the role of maintaining Ca^{II} homeostasis in cells. Due to the similar chemical properties of Ca^{II} and Mn^{II} it is reasonable to assume that NCX also transports manganese [24]. Evidence for manganese transport by NCX was first observed in myocardial cells [43,44]. Recent studies demonstrate elevated manganese levels due to an inhibition of NCX channels in immortalised mouse striatal neuroprogenitors [45]. The efflux of Ca^{II} (and possibly Mn^{II}) from cells occurs in exchange of three hydrogen ions. Due to the efflux of two positive charges and the influx of three negative charges, an electrochemical gradient arises, which constitutes the driving force for the ions' transport trough the PM [46].

Dysregulation of manganese transporters

Dysregulation of metal transporters are reasonably assumed in fast growing-cancer cells with presumably altered metal metabolism. Several studies have been conducted comparing protein expression levels in healthy and cancerous tissue and dysregulations in cancer were found for DMT1 [47], members of the ZIP and ZnT family [48,49], and Fpn [50]. However, these results were not discussed in relation to manganese and require further investigations including influencing factors such as the tissue origin and proliferation activity.

1.2 Spatial analysis of biological tissues via LA-ICP-MS

Many functional biological processed rely on the interactions of metals with biomolecules, and function through the up- and downregulation of specific proteins [51]. The fundamental understanding of these processes requires knowledge of the spatial localisation of metals and proteins, as well as an accurate determination of protein levels. The following section presents an introduction of suitable techniques for elemental and molecular imaging via LA-ICP-MS.

1.2.1 Elemental bioimaging

Numerous techniques are available for the spatial analysis of elements in biological tissues, collectively grouped under elemental bioimaging (EBI). These techniques pose different advantages and limitations, and the choice of method must be evaluated via consideration of the application. Several comprehensive reviews on EBI methods and applications have been published over the years [52–54].

The leading technique for spatial elemental analyses is LA-ICP-MS, which was introduced by Gray in 1985 for the analysis of rock samples [55]. The first precise mapping of biological tissue was done by Wang in 1994 [56]. LA-ICP-MS offers multi-element analysis and combines high lateral resolution (<5 µm) with high sensitivity (µg·g level) and has been applied to biological, pharmaceutical, and medical investigations, as well as metallurgy, archaeology, and material science [57,58]. Here, a focussed laser beam ablates the sample line-by-line, and the produced plume of matter is transported into the ICP-MS, where the particles are ionised, filtered, and detected. The amount of ablated material directly correlates with the detection limits requiring a compromise between image resolution and sensitivity [59].

Another important advantage of LA-ICP-MS is the possibility to perform spatially resolved quantification. Several suitable calibration techniques have been

developed, critically evaluated and compared [58,60,61]. External calibration is the most applied method, using a range of different materials aimed to mimic the density and ablation characteristics of the sample. Matrix-matched standards have been fabricated with homogenised tissue [62–66], gelatine [67], polymers [68], and agarose gel [69] that is spiked with known amounts of the target element, however even the most accurately prepared matrix-matched standards cannot compensate heterogeneities within the tissue. The issue of inhomogeneities has been addressed by employing internal standards [66,70,71] and online isotope dilution analysis [72,73].

The low-cost single quadrupole ICP-Q-MS is the most commonly used mass analyser, and accounted for more than 95% off all ICP-MS installations in 2008 [74]. It is the most frequently employed instrumentation in the field of LA-ICP-MS imaging [75], however some biologically relevant elements are affected by spectral interferences, limiting the applicability of the single quadrupole system. The abundance of polyatomic interferences is generally lower in dry plasmas as used in LA-ICP-MS compared to wet plasmas [76], nonetheless they are still present for many biologically relevant trace elements [77]. Some applications use high mass resolution sector field instruments to distinguish between the target element signal and interferences [78,79]. However, sector field instruments are expensive and ion transmission is compromised by high mass resolution. Alternative approaches use a triple quadrupole technology (ICP-QQQ-MS), where polyatomic interferences are removed in a collision/reaction cell by chemically induced dissociation or kinetic energy discrimination [80,81]. For example, hydrogen may be introduced as a collision gas to remove argon oxide ($^{40}Ar^{16}O^{+}$) interferences when analysing iron. Oxygen gas may be used to produce an $^{16}O^{+}$ mass shift for analytes that are difficult to detect at low concentrations, including phosphorus, sulfur, selenium and silicon in organic matrices [65,82].

1.2.2 Immuno-mass spectrometry imaging

The spatial analysis of biomolecules via LA-ICP-MS is facilitated by integrating immunohistochemistry (IHC) into the imaging workflow. Together with EBI, immuno-mass spectrometry imaging (iMSI) can provide important information on the molecular basis of diseases and the processes within cells [83].

IHC exploits antibodies to identify and visualise antigens (proteins) in biological tissues via specific affinity to a selected epitope. Antibody labelling with a chemical marker was first reported in 1941 [84]; nowadays the technique is important in analytical biochemistry and diagnostics, and is routinely used for investigations of tissue morphology, subcellular structures, and cell types [83]. In chromogenic IHC, the antibodies are tagged with a chemically bound enzyme that forms a precipitate when reacting with a substrate for visualization [85]. Alternatively, antibodies may be labelled with fluorophores [86]. However, these modalities only allow qualitative information and different analytes are required to be visualised on consecutive tissue sections, hampering the comparability of protein expression and locations.

These issues above can be overcome by iMSI, which uses metal-conjugated antibodies and LA-ICP-MS for the visualisation of the target analytes. The metal tags are preferably lanthanides or metals that are not found in biological specimens [83,86]. IMSI enables spatial and quantitative analysis of protein expression within tissue sections and improves the comparability as protein expressions may be normalised [83]. More than 30 antibodies may be imaged simultaneously by multiplexing with differently tagged antibodies [87]. IMSI offers a wide dynamic range of 10^5 which surpass chromogenic and fluorescent IHC by 1000 and 100-fold, respectively. Additionally, mass tags do not degrade and samples can be stored indefinitely before analysis [86]. However, IHC is known to cause wash out effects on endogenous metals, requiring acquisition of the elemental distribution from a parallel tissue section. Beyond that, integration of IHC and chemical imaging is not trivial and requires laborious optimization. A comprehensive guide focusing on the technical challenges of IHC and LA-ICP-

MS imaging has been published [83]. iMSI has been widely used to investigate metal-protein interactions and protein expression levels in diseases such as Parkinson's disease [88,89], Wilson disease [90], and plays a significant role for cancer research, prognosis, and treatment. IHC based assays are used for cancer biomarker identification and detection as well as classifications of the tumour type and stage [86,91]. Reviews on the history of ICP-MS based immunoassays and their application can be found in the literature [92].

Antibody labelling can be performed with metal coded affinity tags (MeCAT), and molecules that contain metal complexing functional groups such as diethylenetriaminetetraacetic acid (DTTA) and 1,4,7,10-tetraazacyclododecane-1,4,7,10-tetraacetic acid (DOTA) or MAXPAR™ polymeric tags. While MeCAT, DTTA and DOTA only bind one single lanthanide atom per tag [83], MAXPAR™ polymeric tags can be loaded with more than 100 atoms per polymer leading to improved sensitivity [93]. Lanthanide ions are especially suited tags for iMSI of biological samples due to the negligible background, and an ionization efficiency of almost 100%. Silver and gold nanoparticles (NPs) are an attractive alternative to lanthanide labels, due to their simple synthesis, low cost, and commercially available pre- labelled secondary antibodies. NPs consist of several thousand atoms and can further improve the sensitivity for specific applications, however non-specific precipitation within tissue sections can cause high background signals, steric hindrance between antibody-NP conjugates can occur, and multiplexing is impeded. Every labelling method possesses different advantages and limitations which should be evaluated with regard to the application and required sensitivity [83].

1.3 Analysis of proteins via CE and CE-ICP-MS

Capillary electrophoresis (CE) is an ideal technique for elemental speciation and the study of metal-protein interactions due to the high separation efficiency, the wide mass range, the simple sample pre-treatments, and the low sample volumes required for analysis. The technique becomes even more powerful when CE is coupled to a highly sensitive detector such as an ICP-MS and can provide insights into cellular processes. For more than 30 years, efforts have been made to use CE for biomolecule analysis, yet the investigation of intact proteins is still challenging due to interactions with the capillary walls, leading to sample loss, band broadening and low reproducibility. This section gives an introduction into the fundamentals of CE, discusses the challenges and advancements of CE-ICP-MS hyphenation, and provides an overview on biomolecule analysis and strategies to facilitate protein separation.

1.3.1 Fundamentals of CE

Electrophoresis as a separation technique was introduced by Tiselius in the 1930s [94,95]. He developed an electrophoresis tube apparatus that was filled with an electrolyte and separated a mixture of two proteins under the influence of an electrical field. In 1948 Tiselius was awarded the Nobel Prize in Chemistry for his research. Major improvements and early work on open tube electrophoresis was facilitated by Hjérten in 1967 [96]. Bare fused silica (BFS) capillaries were first employed by Jorgenson and Lukacs in 1981 [97].

CE separates analytes based on their different mobilities in an electric field. The typical CE set up is shown in Figure 1-1 A and is quite simple. A BFS capillary (length between 30 and 100 cm, internal diameter between 25 and 100 µm) is immersed into two vials containing a background electrolyte (BGE). Also submerged are two electrodes that are connected to a high voltage power supply. For analysis, the capillary is filled with an aqueous BGE, a sample is injected on the anodic side of the capillary and a high voltage is applied, causing the bulk solution to move towards the cathode where the detector is located. The induced

movement is called the electroosmotic flow (EOF) and is essential for the simultaneous analysis of positive, neutral, and negative analytes in typical CE applications.

The EOF is caused by negatively charged inner capillary walls as depicted in Figure 1-1 B. In BGEs with pH values above 3, the silanol groups of the BFS capillary are deprotonated, resulting in a negative surface charge ($Si\text{-}O^-$). The inner surface charge successively becomes greater with increasing pH values. The counter ions (in this case cations) of the BGE accumulate on the $Si\text{-}O^-$ groups and form a layer tightly bound to the silica surface (Stern Layer), which partially shields the negative charges on the surface. Above this static layer, a second layer consisting of solvated cations is formed and balances the remaining negative $Si\text{-}O^-$ groups. These cations are mobile and comprise the diffuse part of the electrical double layer. Upon voltage application across the capillary, the solvated cations start moving towards the cathode, dragging the bulk solution in the capillary with them. Compared to hydrodynamic systems, the flow profile of the EOF is flat (Figure 1-1 C). The force of the flow is equally distributed along the capillary and is responsible for the high resolution obtained with CE.

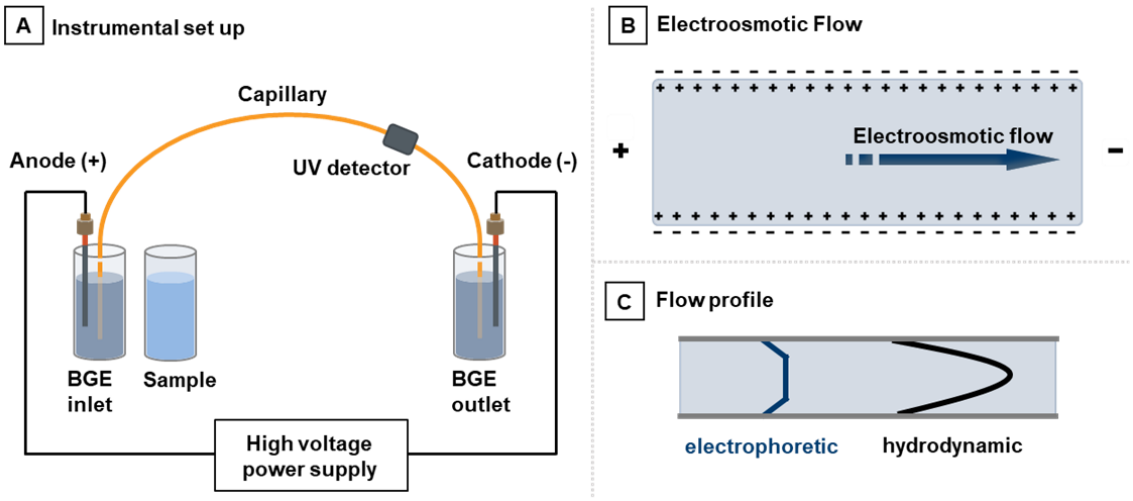

Figure 1-1: The typical CE set up is simple and consists of a BFS capillary immersed into two BGE vials, two electrodes that are connected to a high voltage power supply, and a ultraviolet (UV) detector on cathode side (**A**). The application of a high voltage results in the formation of the EOF, which is the movement of the bulk solutions towards the cathode (**B**). Compared to a hydrodynamic flow profile, the flow profile of the EOF is flat, resulting in narrow peak shapes (**C**).

The flow rate of a BGE moving through the capillary is called the electroosmotic flow velocity v_{EOF} and is a function of the electroosmotic mobility μ_{EOF}, and the applied electric field strength E, as given in equation (2.1).

$$v_{EOF}=\mu_{EOF}\cdot E \tag{2.1}$$

The electroosmotic mobility μ_{EOF} is defined by equation (2.2)

$$\mu_{EOF}=\frac{\varepsilon\zeta}{4\pi\eta} \tag{2.2}$$

where ε is the BGEs dielectric constant, ζ the zeta potential, and η the BGEs viscosity. The zeta potential ζ is defined by the exponentially decreasing charge density of the diffuse layer from the capillary walls to the inner of the capillary and dependant on the BGEs properties. The zeta potential and EOF velocity in BFS capillaries increase with increasing pH values but are inversely correlated to the ionic strength of the BGE.

The second mechanism of electrophoresis when a potential is applied over the capillary is the analytes' response to the electric field. Cations will migrate towards the cathode, anions towards the anode, and neutral species remain stationary. The velocity an analyte travelling towards the electrode of opposite charge is called the electrophoretic velocity v_{ep} and is given by equation (2.3)

$$v_{ep}=\mu\cdot E \tag{2.3}$$

where μ is the analytes effective mobility and E the magnitude of the applied electric field. The analytes electrophoretic mobility μ is defined by equation (2.4) when the electrical force is equal to the frictional force

$$\mu=\frac{q}{6\pi\eta r}\cdot E \tag{2.4}$$

where q is the solutes charge, η the viscosity of the BGE, and r the analytes radius. Consequently, small and highly charged species travel with high mobilities

towards the electrode of opposite charge, whereas large and minimally charged species have low mobilities in the electric field.

In presence of an EOF, the total velocity of an analyte v_{tot} results from the vector sum of the electrophoretic velocity v_{ep} and the velocity of the EOF v_{EOF} as given in equation (2.5),

$$v_{tot}=v_{ep}+v_{EOF} \tag{2.5}$$

and is the reason why cations, neutrals species (as one peak) and most anions eventually reach the detected located on the outlet side of the CE system. Figure 1-2 visualises electroosmotic mobility and the electrophoretic mobilities of the analytes (A) along with the resulting electropherogram and typical migration orders (B).

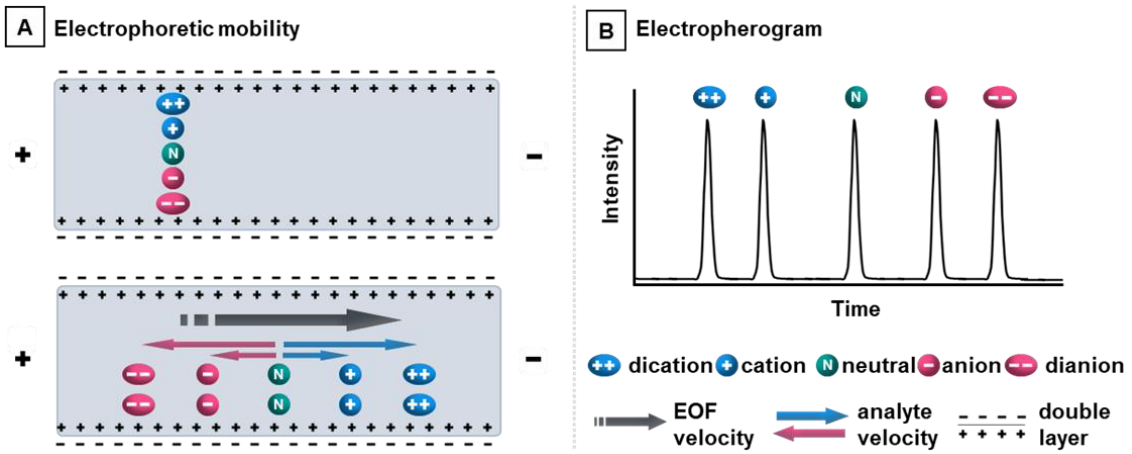

Figure 1-2: Electroosmotic mobility and electrophoretic mobility of differently charged analyte ions in BFS capillaries (**A**). Resulting electropherogram with typical migration order (**B**).

1.3.2 Introduction to CE-ICP-MS

Metalloproteins are involved in crucial biological reactions such as water oxidation and photosynthesis [98], and many endogenous proteins harness metal ions for their structural stabilisation as well as to maintain their functionality [99]. Certain metal ions and elemental species are associated with diseases and toxicity [100], emphasising the requirements for speciation analysis and the study of metal-protein interactions. This knowledge can help understanding chemical

and biochemical reactions and can then provide insights into metal transport, transformation, metabolic pathways, bioavailability, and toxicity [101].

The speciation analysis of complex biological samples requires both efficient separation methods, and highly sensitive (element specific) detectors. Separation techniques such as gas chromatography (GC), high performance liquid chromatography (HPLC) or CE have been coupled with mass spectrometers to pursue these biological investigations [102–104]. CE-ICP-MS is a particularly suited modality, as CE offers excellent separation efficiency over a wide mass range, uses low sample/solvent volumes, and requires little to no sample pre-treatments. When combined with the advantages of ICP-MS, including high sensitivity, multi element detection and compound independent quantification, the technique is preferred for investigations of various analytes in complex biological matrices [101,105].

However, coupling CE and ICP-MS can be difficult due to the necessity of a closed electrical contact, the low flow rate within the separation capillary, and the high gas flows in the ICP-MS [106]. An interface that reliably hyphenates the two techniques is required to (1) uphold an effective electrical connection during the CE separation, to (2) overcome incompatibilities between the flow rate of the EOF and the uptake requirements of the nebulizer, to (3) suppress laminar flows caused by the force of the nebulizer that could impair the CE separation, and to (4) ensure a high sample transport efficiency into the ICP-MS [107,108].

The first CE-ICP-MS interface was designed by Olesik *et al.* in 1995 [108], which has been further advanced by numerous researchers and groups. Approaches that have been developed to ensure a reliable electrical contact during the CE separation utilise silver coated separation capillaries [108], platinum wires [109,110], stainless steel unions [111–113], three and four piece connections for electrode grounding, nebulizer and make up flow capillaries (if employed) [114–116], sheathing solutions [117], and electrodes inserted into electrolyte reservoirs [118,119]. A variety of interface designs have been proposed to overcome the flow rate imbalance between CE and ICP-MS and to reduce the suction effect of

the nebulizer. Chan *et al.* published multiple studies that improved sheathless interface design to address the above issues [109,110]; other groups added make up flows to increase the flow entering the nebulizer using peristaltic or syringe pumps [120], self-uptake or hydrodynamic force; the Barnes group applied a negative pressure to the inlet site of the separation capillary to counterbalance nebulizer suction [121]. The analytical performance of the hyphenated system is strongly dependant on the nebulization efficiency and self-aspiration rate, justifying the many efforts and developments that have been made for efficient nebulizer and spray chamber designs. These include commercially available systems such as the CETAC Capillary Electrophoresis Interface (CEI)-100 Nebulizer [122,123], the Burgener MiraMist Nebulizer [124], and the Meinhard Direct Injection High Efficiency Nebulizer (DIHEN) [117], as well as homemade prototypes [125–129]. More in-depth information on the progression of CE-ICP-MS and the various designs can be found in the literature [101,130–134].

The scope of possible CE-ICP-MS applications is wide and under exploited. Besides using the technique for elemental speciation [128,129] and the study of metal-ligand interactions [105,135], the hyphenated system has been employed to investigate interactions of metallodrugs and biomolecules [136,137], for NP analysis [128,138], and the indirect quantification of proteins and nucleotides [114].

1.3.3 Strategies for protein analysis via CE

CE is an excellent modality for the separation of proteins, is suitable for wide mass ranges, has many available separation modes, has various biological compatible BGEs at different pH values, and has facile sample pre-treatment requirements. The low sample consumption especially makes CE the preferred method for the analysis of expensive and volume limited (biological) standards, surpassing separation techniques such as GC and HPLC.

However, analysing intact proteins via CE remains challenging due to varying isoelectric points (pIs) and different regions of polarity within the biomolecule.

Hydrophilic and hydrophobic interactions between the fused silica capillary walls and the macromolecule can lead to potential sample loss, band broadening, peak tailing, and poor reproducibility [139,140]. Still, most CE protein separation are conducted on BFS capillaries.

Strategies to overcome protein-capillary wall interactions include the use of high and low pH values. At high pH values, the capillary walls and the proteins are negatively charged inducing repulsive interactions, whereas low pH values lead to neutral capillary walls and globally positively charged proteins. Additionally, increasing the ionic strengths of the BGE as well as the addition of ion pairing reagents, surfactants or organic solvents has been shown to reduce capillary wall interactions [140,141].

Modifications of the inner capillary walls are widely performed to improve protein analyses and can be categorised as dynamic and permanent coatings. Dynamic coatings are prepared by adding a coating agent to the BGE, allowing facile optimization of the separation selectivity and improved repeatability as the coating is maintained during each analysis. However, undesired interactions between the additive and the analyte or matrix may impair the separation efficiency. The more labour-intensive static-covalent and static-adsorbed coatings offer a higher stability and are prepared by polymerisation or silanisation reactions within the capillary, or by physical adsorption of a coating agent [140]. Coatings with different polarities have been developed, and the most frequently applied neutral coatings are poly(vinyl alcohol) [142] and linear polyacrylamide [139,143] coatings. Cationic modifications are possible using polyethylenimine [144], polybrene [145] and polyarginine [146] or the application of successive multiple ionic polymer layers (SMIL) [147]. Anionic coatings have been produced with bilayers of polybrene and dextran sulfate [148] or polybrene and poly(vinyl sulfonic acid) [149]. Further information on capillary coatings and their application for the analysis of proteins can be found in comprehensive reviews by Horvath and Dolník [150] and Huhn *et al*. [140].

An interesting alternative to BFS capillaries for protein analysis are GC capillary columns. GC columns are produced from the same fused silica, have a polyimide coating, are routinely manufactured for the large application base of GC, and can be obtained at low cost. The capillary walls are internally coated with a bonded liquid film of neutral dimethyl polysiloxane (PDMS) and (phenyl)-methylpolysiloxane, or highly polar polyethylene glycol. Only a few applications of GC capillary columns for CE are found in the literature and include the analysis of anions [151–153] and various biologically relevant molecules [154–157]. While some researchers report highly reliable and reproducible results, others had issues with the selection of suitable separation conditions.

1.4 Advanced ICP-MS operation modes

1.4.1 Triple quadrupole ICP-MS operation modes

With the introduction of triple quadrupole ICP-MS instruments in 2012, novel, interesting, and powerful ICP-MS operations modes became available. The ICP-QQQ-MS consists of three serially installed mass analysers, the first quadrupole (Q1), an octupole-based collision/reaction cell (referred to as Q2), and the second quadrupole (Q3). The triple quadrupole instrument can be operated in three different modes - the single quadrupole mode, the mass shift mode, and the bandpass mode - making it well suited for a large variety of applications [158].

The single quadrupole mode gives the option for running the ICP-QQQ-MS similar to a single-quadrupole ICP-MS where Q1 functions as mass filter.

The mass shift mode is suitable for analytes that are difficult to detect via ICP-MS as, for example, sulfur. In this approach, Q1 is set to the mass-to-charge ratio (m/z) of the precursor ion ($^{32}S^{+}$), this then enters the collision/reactions cell where it forms a product with the introduced reaction gas (i. e. oxygen gas) and Q3 filters on the m/z of the product ion ($^{32}S^{16}O^{+}$), allowing the adduct to pass through to the detector. A variety of different metals and heteroatoms have been analysed in

biological, environmental, and organic matrices using either oxygen [158–163] or other reaction gases [159,164,165] to produce a mass shift.

In bandpass mode the scanning properties of Q1 are altered, letting multiple m/z pass through the system [159]. This improves ion transmission and reduces selectivity and is suitable for samples where unit mass resolution is not required. The resolution only needs to be high enough to resolve the elements of interest in the sample [166]. Q1 mass filtering may be manipulated by changing the scan line slope (SLS) and scan line gain (SLG) factors [159]. The principle can be best explained by looking into the operation principle of the quadrupole. As visualised in Figure 1-3 A, a quadrupole mass analyser consists of four metallic rods that are operated with a set of static voltages (direct current (DC) voltages) and alternating voltages (radio frequency (RF) voltage). Specific DC/RF combinations stipulate stable trajectories for a target m/z in the quadrupole that then can reach the detector whereas other ions will hit the metallic rods. The two-dimensional motion of ions through the quadrupole can be described by the Mathieu equations, their graphical solution is depicted in the Mathieu stability diagram in Figure 1-3 B. Each m/z has triangular shaped stability region in which each combination of DC and RF voltage assign stable trajectories through the quadrupole. They have regions of overlap, where technically multiple m/z would be able to pass the quadrupole, but also regions where only one m/z would be stable. This is where the scan line (teal coloured line) of standard ICP-MS tunes achieve an 1 amu mass resolution. In bandpass mode, this scan line is shifted by changing the SLG and SLS factors towards a region with more overlap, allowing multiple m/z to pass simultaneously [167]. This concomitantly produces increased ion transmission and higher sensitivities. Associated drawbacks, as for example the elevated occurrence of interferences can be compensated by employing the two additional multipoles, Q2 and Q3 [158].

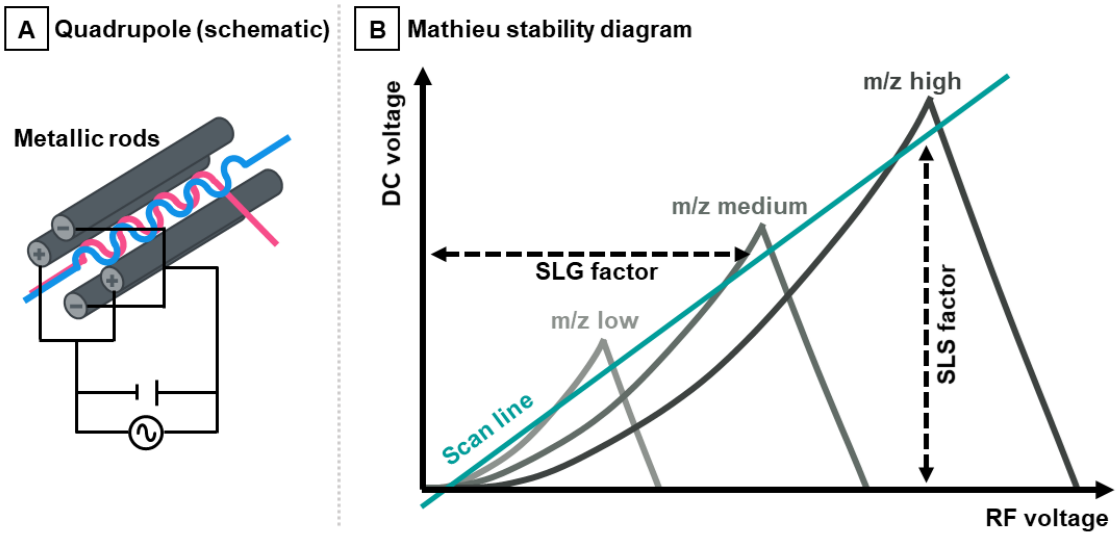

Figure 1-3: Schematic set-up of a quadrupole (**A**) and Mathieu stability diagrams (**B**). A quadrupole consists of four metallics rods and is operated with a set of DC and RF voltages. The Mathieu stability diagram gives an overview of DC/RF combinations that stipulate stable trajectories for a target ion through the quadrupole.

The bandpass mode has been applied for the analysis of sulfur in organic matrices [158], in LA-ICP-MS applications [65,168], for the analysis of contrast agents used in diagnostic imaging in environmental samples [169], and in the scope of this thesis, for the characterisation of NPs [166].

1.4.2 Single-particle ICP-MS

The ongoing instrumental advancements for rapid detection as well as constantly improving processing methods have opened new strategies for the characterisation of all kinds of nanostructures [170–173]. Single-particle (SP) ICP-MS has evolved as important technique for the characterisation NPs and the basic principle of the technique was introduced by Degueldre *et al.* in 2003 [174].

The concept of SP ICP-MS relies on the separate introduction and detection of NPs in the ICP-MS. At low particle concentrations, NPs enter the plasma individually, are atomised, ionised, and produce separate ion clouds which are focussed on the detector. This leads to the detection of discrete signals with an intensity according to the particles size. When an ICP-MS with a fast integration

time is used, these single-particle peaks are described by multiple points, which allows integration and leads to improved signal-to-noise ratios. Thousands of NPs can be detected per minute, allowing a facile and rapid determination of the elemental compositions, size distributions, and particle number concentrations [175,176]. Figure 1-4 shows a time resolved scan of a NP suspension (A), the resulting signal distribution which consists of two populations, the background and noise (left) and the NP signal (right) (B), as well as the size distribution (C).

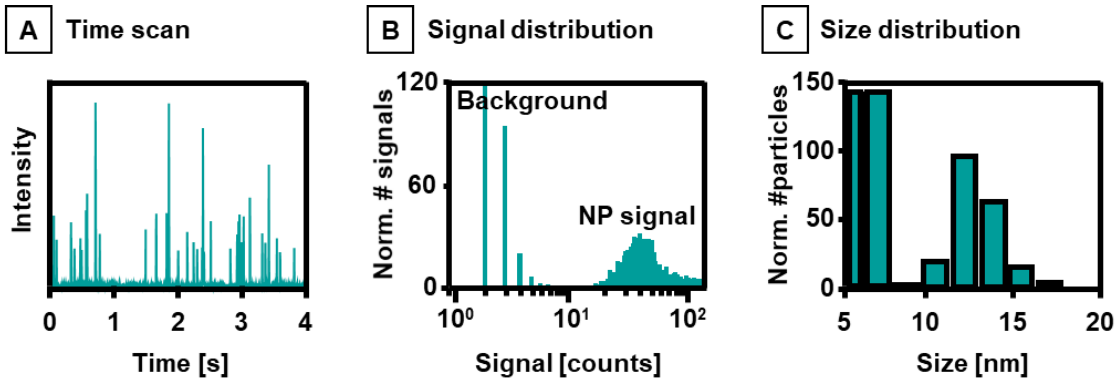

Figure 1-4: The SP ICP-MS analysis of dilute NP suspensions leads to the detection of discrete signals (**A**). After collecting a sufficient number of NPs, the signal distribution (**B**) and size distribution (**C**) can be calculated using basic statistical tools.

NPs with dimensions between 1 and 100 nm have tremendous potential for applications in medicine, chemistry, biology, and physics. Consequently, there are several reviews focusing on the applications, developments, potential and limitations of SP ICP-MS [175,177–179].

1.5 Aims and scope

Many cancers are variably resistant to radiation therapy. Some patients die within months, while others with the same tumour type and radiation protocol survive for years. A novel hypothesis is that tumour radioresistance is sustained by non-enzymatic complexes of manganese with small molecular metabolites, protecting cells from the products of IR. Multiple influx and efflux metal transporters are involved in manganese homeostasis and are possibly abnormally expressed on the surface of cancer cells, causing varying concentration of manganese within tumours.

EBI is an established technique for the spatial analysis of metal distributions in biological tissues. Proteins may be visualised via iMSI utilising a metal labelled antibody which acts as proxy for the target protein. However, the number of metals per antibody varies significantly, impeding the comparability of protein expression levels. To generate reliable and high-quality interpretable data, the number of metal labels per antibody needs to be determined after every labelling protocol. Accordingly, this thesis introduces several methods to determine the labelling characteristics of metal labelled antibodies and lays the foundation for investigating the underlying mechanism of resistance to radiotherapy. The specific aims and objectives are:

Aim 1: The development of a universal workflow for the separation of intact proteins by CE.

a) To assess the feasibility of applying GC PDMS capillaries for CE.
b) To coat PDMS capillaries with cationic and anionic surfactants and determine the stability of these coatings.
c) To evaluate the suitably of CTAB-PDMS, SDS-PDMS, and BFS capillaries for the analysis of model proteins with different pIs and MWs in BGEs over a wide pH range.
d) To outline guidelines for the targeted selection of CE separation conditions by knowledge of the protein's pI and MW.

e) To demonstrate the concept via analysis of caseins and whey proteins in milk.

Aim 2: The development of a simple and robust CE-ICP-MS interface.

a) To construct a simple CE-ICP-MS interface via consideration of nebulizer design, capillary dimensions, make up flows, and electrical contacts.
b) To develop a CE-ICP-MS method for the separation of gadolinium-based contrast agents (GBCAs) as model analytes.
c) To evaluate the interface's functionality, linearity, and robustness for compound-independent quantification of gadoxetic acid in urine samples.

Aim 3: The characterisation of metal labelled antibodies via CE-ICP-MS.

a) To develop a workflow for the determination of the labelling degree of lanthanide-polymer conjugated antibodies.
b) To determine the number of metals per antibody in gadolinium-polymer labelled antibodies.
c) To develop a quality control method to verify a successful conjugation of antibodies with NPs.

Aim 4: The characterisation of NPs by SP ICP-MS.

a) To developed novel methods with increased ion transmission for SP ICP-MS analyses.
b) To evaluate and use these methods for an improved size characterisation of gold NPs.
c) To determine the size distribution and composition of UCNPs.
d) To develop a statistical model to determine particle-particle interactions.

Aim 5: The imaging of manganese transporters and transition metals in human melanoma samples.

a) To assess the feasibility of applying concomitant iMSI and EBI to spatially localise the transporter proteins ZIP8 and ZIP14, and transitions metals in human melanomas.
b) To compare different antibody staining methods for protein expression image quality.
c) To spatially compare transporter protein expression and transition metal concentrations in tumour areas.

Chapter 2

Separation of Intact Proteins by Capillary Electrophoresis

Based on:

Sarah Meyer, David Clases, Raquel Gonzalez de Vega, Matthew P. Padula and Philip A. Doble, *Separation of Intact Proteins by Capillary Electrophoresis*, Analyst (**2022**), 147, 13, 2988-2996.

2.1 Introduction

Every third protein in functional physiological processes is presumed to require a metal as co-factor, and the intracellular metal concentrations, protein expression, as well as the incorporation in metalloprotein is understood to be tightly regulated [180,181]. Accordingly, reliable, and validated technologies are required to quantitively assess and understand these processes. CE offers excellent potential for investigations of complex biological samples due to the high separation efficiency, wide mass range and the requirements of low sample volumes. This chapter addresses Aim 1, the development of a universal workflow for the separation of intact proteins by CE and lays the foundation for developments of quality control workflows and eventually the analysis of cellular components in the future.

Proteomics may be defined as the study of the entirety of proteomes. The proteome is a collection of proteins produced in a species or organ and typically contains many thousands of proteins of potential interest that require identification and quantification to gain insights into fundamental biological processes and biomarker discovery [182]. Separations by CE are often hampered by undesirable electrostatic and hydrophobic interactions between proteins and the BFS capillary surface [141,150,183,184], leading to potential sample loss, band broadening, peak tailing, and poor reproducibility [139,140].

Regardless, most CE protein separations are performed using BFS capillaries. The net charge of any given protein may be inferred by consideration of the pI and the pH of the BGE. When the pH of the BGE is below that of the pI, the protein will have a net positive charge, and at pH values above, a net negative charge. Furthermore, at BGE pH values above 3, the silanol groups at the surface of the capillary are deprotonated and negatively charged, typically limiting the selection of suitable BGEs to a narrow pH range. At high pH, electrostatic interactions are minimised by the repulsive negative charges on both the capillary surface and protein. This limited pH selection renders some protein analyses unfeasible due to solubility or stability issues, or insufficient electrophoretic

mobility when the pH of the BGE is close to the pI of the protein of interest. Attempts to mitigate adsorption include increasing the ionic strength of the BGE to compete with proteins for available binding sites on the capillary surface; the addition of ion pairing reagents and surfactants to the BGE to lower the net protein charge [140]; or by inclusion of organic solvents into the BGE [141].

Modifications of the BFS capillary surface have also shown some success at preventing protein interactions to improve the separation efficiency and reproducibility, and the practicable pH range for separation. These approaches typically involve the addition of dynamic coating reagents to the BGE; or the manufacture of static coatings by chemically modifying the capillary surface, or adsorption of a coating agent. These coatings must be compatible with the sample matrix, be stable over time, and allow the use of a variety of BGEs with a wide range of concentrations. Ideally, they should be easy to prepare and inexpensive [140].

Various neutral, cationic, and anionic BGE additives have been employed to dynamically coat the surface of BFS capillaries. The charge on the surface of the capillary may be neutralised by addition of non-ionic polymeric surfactants including polyoxyethylene ether (Brij-35) [185], or hydroxypropylmethylcellulose (HPMC) [186], which mask the silica surface and deactivate the silanol groups, and slow down or eliminate the EOF. Suitable cationic additives include polyamines [187], and quaternary ammonium surfactants, which electrostatically bind to the capillary surface and suppress or reverse the EOF. Anionic additives, such as dextran sulfate [188] or poly(vinyl sulfonic) acid) [189] generate a negative charge at the surface of the capillary over a wide pH range. These dynamic coatings offer facile optimisation of separation selectivity as the modifier is added to the BGE, and improved repeatability by continuous regeneration of the coating during each analysis. However, separation efficiencies may be negatively impacted by undesirable interactions between the additive and the analyte or matrix [140].

Static-covalent and static-adsorbed coatings offer greater stability than their dynamic counterparts. Static-covalent coatings are typically manufactured *in-situ* by polymerisation or silanisation reactions. Static-adsorbed coatings are prepared by flushing the capillary with polymers containing cationic amine functional groups, or polymers with a polyacrylamide backbone. The high charge density of these reagents produce sufficiently stable coatings by strong electrostatic adsorption to the silanol surface of the capillary [190]. Other examples of cationic coating reagents include polyethylenimine [144], polybrene [191] and polyarginine [146], or the application of successive multiple ionic polymer layers (SMIL) [147]. Anionic coatings may also be fabricated with bilayers of polybrene and dextran sulfate [148] or polybrene and poly(vinyl sulfonic acid) [149]. Similarly, neutral capillary surfaces may be prepared with poly(vinyl alcohol) [192], and linear polyacrylamide [139,143]. Further details and applications of capillary coatings are available in comprehensive reviews by Horvath and Dolník [150] and Huhn *et al*. [140].

An area of investigation that has had little attention is the transfer of the column technology of gas chromatography. GC capillary columns are manufactured from the same fused silica and outer polyimide coating typically employed with CE separations, are easily obtained, and of low cost. GC capillary columns are internally coated with a bonded liquid film of varying polarities such as neutral dimethyl polysiloxane (PDMS) and (phenyl)-methylpolysiloxane, or highly polar polyethylene glycol. Reports of the application of GC columns for CE include the analysis of anions [151–153], low-molecular-mass RNA [154], amino acids [155], nucleotides and Coenzyme A compounds [156], cysteine and thiols [193], proteins in white wine [194], glycoproteins [157], and oligosaccharides [195]. While some groups reported reliable and reproducible outcomes, others experienced difficulties with BGE pH selection, concentration, or incompatible additives.

The analysis of intact proteins remains challenging due to the variety of molecular weights (MWs), hydrophobicities, and pIs, rendering the selection of suitable CE

conditions tedious and/or ad-hoc. This chapter introduces a novel and universal experimental workflow for the analysis of intact proteins with any MW or pI, as well as guidelines for targeted selection of appropriate BGEs. Here, we evaluated the suitability of neutral GC PDMS (DB-1) capillaries with dynamic coatings of cationic cetyltrimethylammonium bromide (CTAB) or anionic sodium dodecyl sulfate (SDS), and BFS capillaries, for the separation of seven model proteins with a range of MWs and pIs using six different BGEs with pH values between 3.0-9.5. Finally, we applied the workflow and guidelines to select the most suitable BGE for the analysis of caseins and whey proteins in cow's milk.

2.2 Experimental section

2.2.1 Chemicals and consumables

Ultrapure water was obtained from an Arium® Pro system (Sartorius Stedim Plastics GmbH, Germany). The proteins, bovine serum albumin (fraction V), α-casein (from bovine milk), β-casein (from bovine milk), creatine kinase (from rabbit muscle), human serum albumin, α-lactalbumin (from bovine milk), β-lactoglobulin (from bovine milk), β-lactoglobulin A (from bovine milk), β-lactoglobulin B (from bovine milk), myoglobin (from equine heart), ribonuclease a (from bovine pancreas), and transferrin (human, 98%, low endotoxin) were purchased from Sigma Aldrich (Castle Hill, New South Wales, Australia). An immunoglobulin G (IgG) antibody (raised in sheep) was acquired from Abcam (Melbourne, Victoria, Australia). Citric acid (CA), tris(hydroxymethyl)aminomethane (TRIS), di-sodium hydrogen orthophosphate dodecahydrate ($Na_2HPO_4 \cdot 12\ H_2O$), sodium dihydrogen orthophosphate ($NaH_2PO_4 \cdot 2\ H_2O$), sodium tetraborate decahydrate, CTAB, SDS, and acetone were obtained from Sigma Aldrich (Castle Hill, New South Wales, Australia). Reduced fat (lite) milk was bought from a local supermarket (Coles, Sydney, Australia). The BFS capillary was purchased from CM Scientific (Silsden, United Kingdom) and the DB-1 capillary (part number 126-1012, internal diameter

0.05 mm, film thickness 0.2 µm) was acquired from Agilent Technologies (Mulgrave, Victoria, Australia).

2.2.2 Capillary dimensions and coatings

The experiments for the systematic study were performed via consideration of three capillary configurations; a CTAB coated PDMS capillary (effective length 51 cm, total length 59 cm, internal diameter 50 µm), a SDS coated PDMS capillary (effective length 56 cm, total length 64 cm, internal diameter 50 µm), and a BFS capillary (effective length 56 cm, total length 64 cm, internal diameter 50 µm). The analyses of the milk samples were executed using a CTAB coated PDMS capillary with an increased capillary length (effective length 110 cm, total length 102 cm, internal diameter 50 µm).

Prior to using PDMS capillaries for the first time, they were conditioned with the respective surfactant to establish a consistent coating of the PDMS capillary walls. The capillaries were flushed with 1 mM CTAB (or 1 mM SDS) for 4 hours and subsequently equilibrated with 0.1 mM CTAB (or 0.01 mM SDS) for 2 hours.

2.2.3 BGE, standards and sample preparation

BGE preparation

All BGE components were freshly prepared at tenfold concentration in ultrapure water and filtered using a syringe filter (Agilent Captiva Econo Filter, PES, 13 m, 0.2 µm). The BGEs were prepared by freshly mixing and diluting the appropriate stock solutions. The BGEs were degassed, and the pH value was measured (Oakton pH 550 pH meter, Oakton Instruments, Vernon Hills, IL, USA) at room temperature before each analysis. 0.1 mM CTAB or 0.01 mM SDS were added to the BGE for the dynamic coating of the DB-1 capillary. The surfactants were not added to the BFS capillary BGEs. A summary of all prepared BGEs and pH values is given in Table 2-1. For the milk analysis, the BGEs (BGE M-I and

BGE M-II) were used in 2-fold concentration for sufficient conductance in the longer capillary.

Table 2-1: BGE composition and experimental pH values. All BGEs have the same basic composition. For the CTAB and SDS capillary, 0.1 mM CTAB and 0.01 mM SDS were added to the BGE, respectively. (- not used for systematic evaluation.)

	BGE composition	**pH (BGE with CTAB)**	**pH (BGE with SDS)**	**pH (BGE, no surfactant)**
BGE **I**	10 mM CA + 5 mM TRIS (+ surfactant)	3.2	3.0	3.1
BGE **II**	10 mM CA + 15 mM TRIS (+ surfactant)	4.5	4.5	4.5
BGE **II**	10 mM CA + 25 mM TRIS (+ surfactant)	5.9	6.1	6.2
BGE **IV**	10 mM Phosphate (+ surfactant)	7.0	7.0	7.0
BGE **V**	10 mM CA + 60 mM TRIS (+ surfactant)	8.2	8.4	8.3
BGE **VI**	10 mM Tetraborate (+ surfactant)	9.3	9.6	9.3
BGE **M-I**	20 mM CA + 10 mM TRIS (+ surfactant)	3.2	-	-
BGE **M-II**	20 mM CA + 20 mM TRIS (+ surfactant)	3.8	-	-

Standard preparation

All protein standards were first prepared as 1000 µg·mL^{-1} stock solutions in ultrapure water. Prior to analysis the protein stock solutions were further diluted to 200 µg·mL^{-1} in ultrapure water and 3.3% (v/v) acetone was added as EOF marker.

Milk sample preparation

160 µL of milk was diluted with 1840 µL ultrapure water and centrifuged at maximum speed for 20 minutes (LabCo Mini High Speed Centrifuge Refrigerated, 5 °C, 15 000 rpm) and stored at 5 °C. Prior to analysis the supernatant was diluted 2-times with ultrapure water and 3.3% (v/v) acetone was added as an EOF marker. Protein identification in the milk sample was performed by individual spiking each protein standard and visual evaluation of the resultant electropherograms.

2.2.4 CE experimental parameters

The CE analyses were performed using an Agilent CE 7100 system (Agilent, Santa Clara, CA, USA). The cassette temperature was 30 °C and the sample storage carousel was maintained at 20 °C. Absorption was monitored at 200 nm for proteins and 240 nm for acetone with an acquisition rate of 10 Hz. Prior to each analysis, the capillary was rinsed with the BGE for 2 minutes for the systematic study, and 5 minutes for the milk analysis. The sample was injected by applying a pressure of 0.725 psi for 10 s and separated at -30 kV (CTAB-PSMD capillary) or +30 kV (SDS-PDMS capillary, BFS capillary) for 8 to 80 minutes. Analyses were performed in triplicate to determine standard deviations.

2.2.5 Data analysis

The electropherograms were integrated using the Agilent ChemStation software. The migration time for the EOF marker acetone, and the proteins were obtained using the peak maximum at 240 nm and 200 nm, respectively. The electroosmotic mobility μ_{EOF} and the apparent mobility of the analyte μ_a were calculated using equation 2.1 and 2.2. The effective mobility μ_e was calculated using equation 2.3 [196].

$$\mu_{EOF} = \frac{l_{eff}\, L_{tot}}{t_{mig,\,EOF}\, V_{sep}} \tag{2.1}$$

$$\mu_a = \frac{l_{eff}\, L_{total}}{t_{mig,\,a}\, V_{sep}} \tag{2.2}$$

$$\mu_e = \mu_a - \mu_{EOF} \tag{2.3}$$

where l_{eff} was the effective capillary length (length to detector), L_{tot} was the total capillary length, t_{mig} was the migration time of the analyte or EOF marker, and V_{sep} was the voltage applied for the separation.

2.3 Results and discussion

2.3.1 Suitability of PDMS capillaries

Typical CE applications use BFS capillaries with internal diameters of 10-75 µm and capillary lengths of 20-100 cm [197]. Fortunately, GC capillary columns are available with CE compatible internal diameters of 50-100 µm and lengths between 5-100 m [198]. Accordingly, GC columns may be purchased off-the-shelf and cut to size as required. A window for UV detection may be simply fabricated by burning away the capillary polyimide outer coating at the appropriate position for custom fits to any CE instrument. GC analyses separate volatile molecules using an inert gas as the mobile phase. The injection of water

is usually avoided on polar GC columns to maintain repeatability and to prevent adsorption of water molecules on the inner capillary thin film. Neutral GC capillaries are unaffected by exposure to water. The successful transfer of GC capillary columns for CE applications requires the internal coating to be resilient to the BGE at varying pH values, and stability of the coating during electrophoresis at high voltages to provide a constant current. Therefore, we evaluated the stability of a neutral PDMS capillary using various aqueous buffers that encompassed standard CE pH working ranges from approximately 3 to 9. The PDMS capillary was cut to a length of 60 cm and flushed with each of the buffers for 10 minutes prior to applying high voltage. The current remained stable in all buffers in a single PDMS capillary for over 100 hours of operation. Table 2-2 lists the recorded average currents and relative standard deviation (RSD) for the six BGEs when applying a voltage of +30 kV to the inlet electrode for 10 minutes. The recorded currents varied due to different ionic strengths between 5 and 24 µA, the RSDs, however, were below 0.5% for each BGE. This result indicated that the PDMS film was stable in aqueous buffers and was a candidate for evaluation of the separation of intact proteins.

Table 2-2: Average current and RSD recorded using BGE I to BGE VI and a PDMS capillary. The acquisition time was 10 minutes, and a voltage of +30 kV was applied.

	Average current [µA]	**RSD [%]**
BGE **I**	5.94	0.48
BGE **II**	10.54	0.12
BGE **III**	19.58	0.18
BGE **IV**	19.48	0.39
BGE **V**	23.80	0.23
BGE **VI**	19.88	0.30

2.3.2 Dynamic coating of PDMS capillaries

The suitability of the PDMS capillary was initially evaluated with a standard solution consisting of an EOF marker, acetone, the amino acid, histidine (His), and the small protein, transferrin (Tf), using BGE I (10 mM CA, 5 mM TRIS, pH 3.2) at +30 kV applied to the inlet electrode. Via consideration of the pI of 7.6 (His) [199] and 5.4 (Tf) [200], it was expected that both analytes were positively charged at pH 3.2, and would migrate towards the detector placed at the cathode.

As anticipated, an EOF was not observed due to the neutral capillary surface, and His migrated as a sharp peak at 6.5 minutes. However, despite having a net positive charge, a peak for Tf was not observed during the acquisition because of complete hydrophobic adsorption on the neutral capillary coating (Figure 2-1 A, top). The capillary was then flushed for 10 minutes with the same BGE, this time with the addition of CTAB (10 mM CA, 5 mM TRIS, 0.1 mM CTAB, pH 3.2). The polarity of the voltage was reversed to -30 kV at the inlet electrode. 10 minutes of initial equilibration with the new BGE was sufficient to generate a stable and rapid anodic EOF as measured by the acetone peak at 2.8 minutes, the Tf migrated as a distinct peak at 4.8 minutes, and His migrated as a narrow and symmetrical peak at 5.2 minutes (Figure 2-1 A, top).

CTAB is a quaternary ammonium surfactant with a long alkyl chain of 16 carbon atoms. This hydrophobic chain adsorbed to the neutral capillary surface, whilst the positive ammonium functional group orientated towards the aqueous bulk electrolyte. This surfactant layer effectively eliminated the hydrophobic adsorption of the protein by repulsive positive charges on both the PDMS film and the protein. The CTAB in the BGE was below the critical micellar concentration (CMC) to minimise potential interactions between the surfactant and the analytes, yet at sufficient concentration for effective maintenance of the coating of the capillary. The separation of His and Tf occurred counter to the direction of the EOF. The migration time of all three analytes stabilised after the fourth injection indicating that the surfactant layer reached equilibrium in less than 50 minutes of continuous acquisition (Figure 2-1 B).

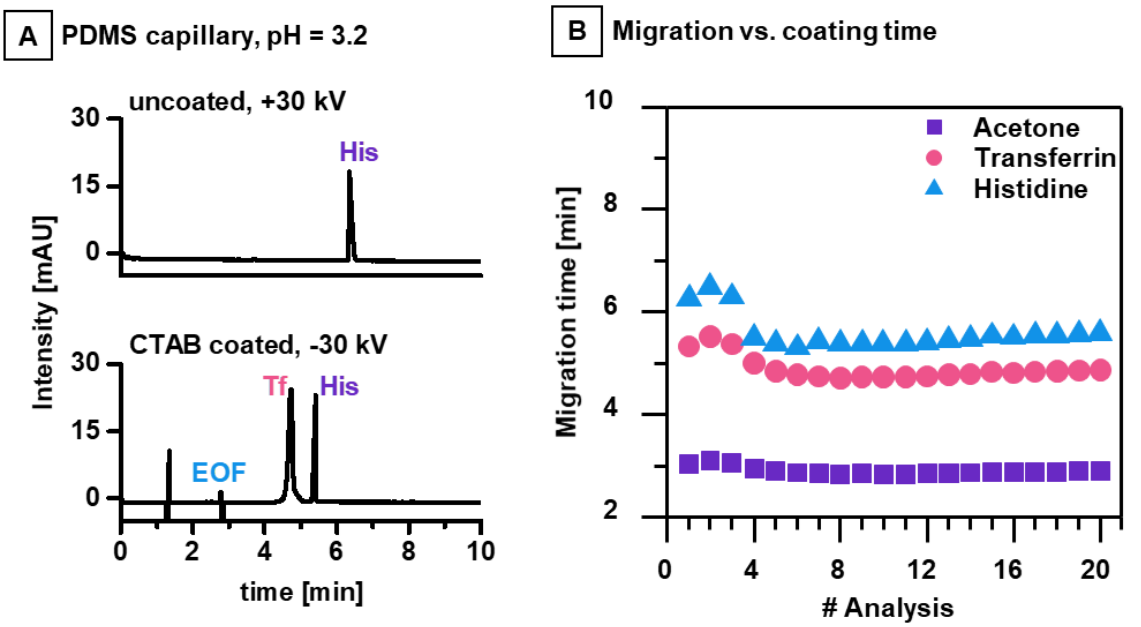

Figure 2-1: Analysis of a standard comprising of acetone, His and Tf on an uncoated and a CTAB coated PDMS capillary at pH 3.2 (**A**), and effect of the CTAB coating time on the migration time of the three compounds (**B**).

The longevity of the surfactant layer was evaluated by removal of CTAB from the BGE and successive injections of the three analytes. As shown in Figure 2-2 A, acetone, Tf and His were only observed as narrow peaks when the BGE contained CTAB (red line). Subsequent analyses without CTAB and a three-minute BGE flush before each injection resulted in adsorption of the protein to the capillary surface and increasing migration times (t_M) and larger peak widths (FWHM) of the EOF marker and His (Figure 2-2 B). This indicated that the surfactant layer was rapidly washed from the PDMS film and that incorporation of CTAB in the BGE was essential.

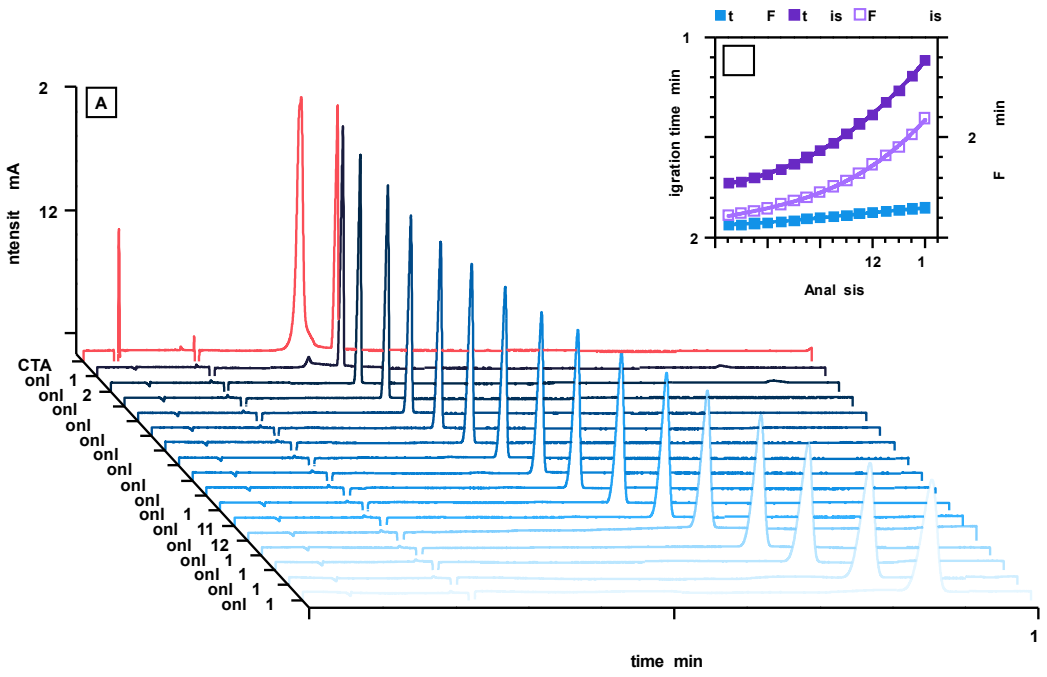

Figure 2-2: Longevity of the surfactant layer (**A**), and effect on the migration times (t_M) and peak width (FWHM) (**B**). Successive analysis of the three analytes acetone, Tf, and His after removal of CTAB from the BGE.

An equivalent reciprocal investigation was conducted above the pIs of the target analytes at pH 8.4. Application of -30 kV with BGE V (10 mM CA, 60 mM TRIS, pH 8.4) resulted in no observable peaks due to an absence of EOF, hydrophobic absorption of Tf, and insufficient mobility of His for migration within a 60 minute acquisition window (Figure 2-3 A, top). Addition of the anionic surfactant, SDS at 0.01 mM, flushing for 10 minutes, and application of +30 kV produced a stable cathodic current with the EOF and His migrating at 3.1 minutes, whilst Tf was not observed (Figure 2-3 A, bottom). In contrast to the CTAB coated capillary, repeated coating and standard injection produced ever increasing migration times for both acetone and His (Figure 2-3 B). This instability indicated that the SDS coating was compromised by adsorption of Tf, which may be resolved by coating the capillary for an extended time prior to injection. The stability of the coating was similar to that of CTAB, with rapid wash off when removed from the BGE. These observations implied that PDMS capillaries had excellent potential for tuneable analyses of proteins.

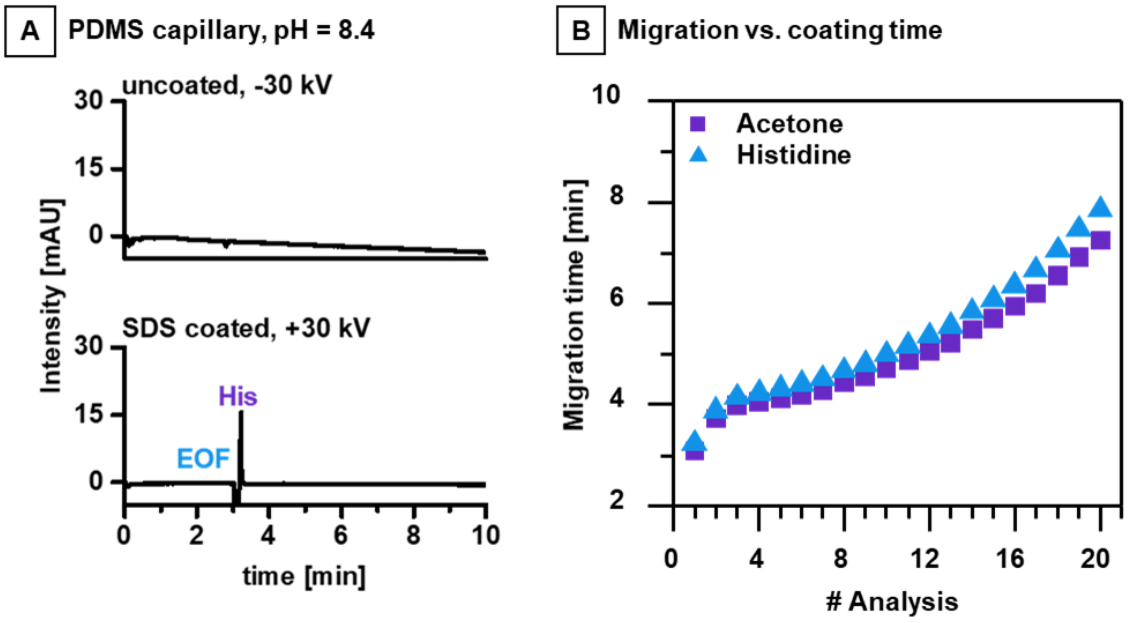

Figure 2-3: Analysis of a standard comprising of acetone, His, and Tf on an uncoated and a SDS coated PDMS capillary at pH 8.4 (**A**), and effect of the SDS coating time on the migration time of the compounds (**B**).

2.3.3 Systematic evaluation of BGEs and capillaries for protein analyses

Both surfactants remain charged across the entire practicable CE BGE pH range, allowing manipulation of pH and EOF direction for predictable control of selectivity and analyte mobility. Accordingly, we conducted a systematic evaluation of three possible scenarios; CTAB coated PDMS capillaries with anodic EOF; SDS coated PDMS capillaries with cathodic EOF; and the more traditional BFS capillaries with cathodic EOF. These three scenarios offered the possibility to tune and optimise the separation of any protein with known pI without hydrophobic or electrostatic adsorption. We chose seven model proteins (and the amino acid His) with a variety of MWs and pIs as illustrated in Figure 2-4. Exact MWs and pIs of these proteins are shown in

Table 2-3. β-lactoglobulin (β-Lg), myoglobin (Mb) and ribonuclease A (RNase) represented small proteins (<30 kDa) with pIs of 5.1, 7.1 (±0.3) and 8.6, respectively. Medium sized proteins (60-100 kDa) consisted of human serum albumin (HSA), transferrin (Tf) and creatine kinase (CK) with pIs of 4.7, 5.4, and 7.2, respectively. An immunoglobulin G antibody (IgG) was selected as a representative of large proteins (>100 kDa) with a pI of 6.0 (±1.0). Acetone was added to each protein standard for determination of the EOF. Six different BGEs were prepared and had pH values ranging from 3.0 to 9.6 as shown in Table 2-1. For clarification, the surfactants were only added to the BGEs for analyses using the PDMS capillary columns, but not for the BFS capillary.

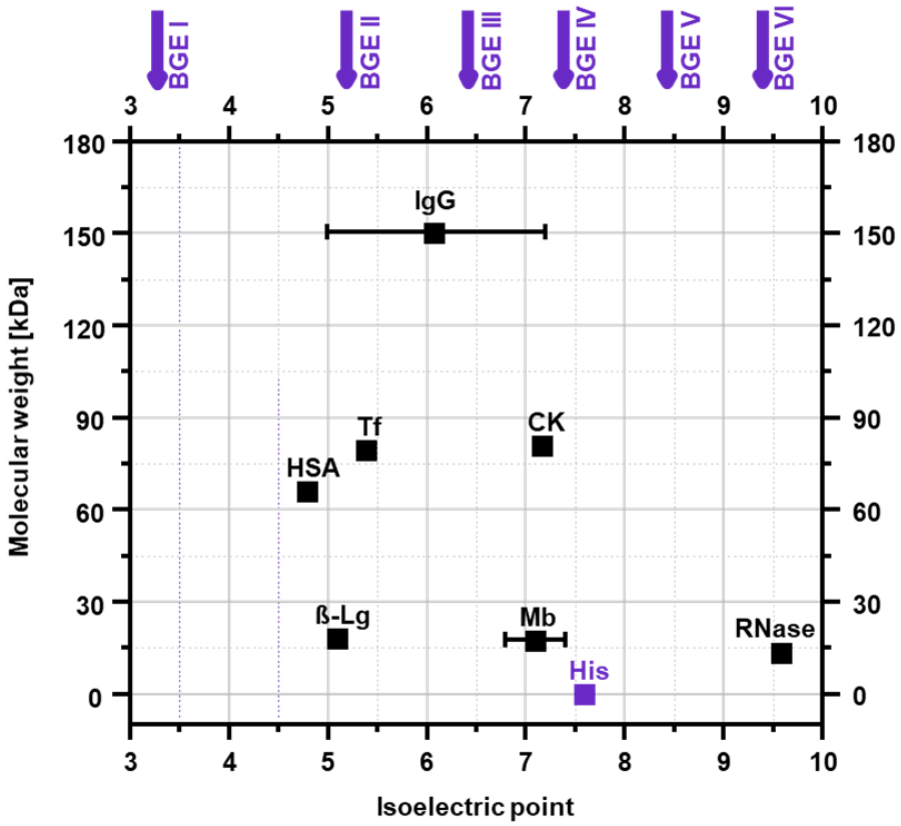

Figure 2-4: MWs and pIs of selected model proteins. The amino acid His was added as a marker due to its charge over a wide pH range. The analytes were selected to cover a wide range of MWs and pIs.

Table 2-3: MWs and pIs for analytes used in the systematic evaluation.

	Molecular weight [kDa]	Isoelectric point
β-Lactoglobulin (β-Lg)	18.3 [201]	5.1 [201]
Myoglobin (Mb)	17.6 [202] (incl. heme group)	6.8-7.4 [203]
Ribonuclease A (RNase)	13.7 [204]	9.6 [204]
Human serum albumin (HSA)	66.4 [205]	4.7 [205]
Transferrin (Tf)	79.5 [206]	5.4 [200]
Creatine kinase (CK)	81.0 [207]	7.2 [207]
IgG antibody (IgG)	150.0 [208]	5.0-7.2 [209]
Histidine (His)	0.155	7.6 [199]

The versatility of the proposed workflow may be best illustrated by evaluation of the migration behaviour of the simplest analyte, His. His has a pI of 7.6, was charged over a wide pH range and had negligible interaction with the surface of the capillaries under all separation conditions.

Consider the electropherograms obtained from the CTAB coated PDMS capillary as shown in Figure 2-5. As expected, there was stable anodic EOF (negative polarity) under all conditions due to the positive charge on the ammonium functional group of CTAB irrespective of the BGEs pH. However, the mobility of the EOF varied between the BGE systems due to necessary changes of ionic strengths of the BGEs for pH selection. At pH 3.2, His was positively charged and migrated as a sharp symmetrical peak after the EOF, i.e., counter to the direction to EOF. As the pH was increased to 4.5, the ionisation of His was suppressed and migrated as an asymmetrical peak at a considerably later migration time. At pH 5.9, the ionisation of His was further supressed with lengthy migration and

similar peak asymmetry. At pH 7.0, His had negligible charge and migrated with the EOF. At pH 8.2, His was negatively charged and migrated before the EOF peak, i.e., in the same direction as the EOF. At pH 9.3, His was fully ionised and negatively charged and migrated as a symmetrical narrow peak before the EOF. The electropherograms obtained from the reciprocal scenarios with the SDS coated PDMS capillary, or the free zone BFS capillary are shown in Figure 2-5 A1. As expected, stable cathodic EOFs (positive polarity) were generated for the SDS-PDMS combination across all BGEs, whereas the EOF was negligible for the BFS capillary at low pH due to suppression of ionisation of the silanol groups at the capillary surface. As before, the mobility of the EOF varied between the BGEs due to varying ionic strengths. The migration of His was consistent across the two systems, and opposite to that of the CTAB-PDMS combination, i.e., His migrated in the same direction as the EOF at low pH, and a counter direction at high pH. At pH 7.0, His migrated with the EOF in both systems. This predictable and tuneable manipulation of the selectively of His across all scenarios is visualised in Figure 2-5 A2, where the mobility of His was plotted against the pH of the BGE. There was excellent consistency of the mobility of His across all three capillaries. A line of best fit crossed the x-axis at approximately the pI of His, indicating that the electrophoretic mobility and therefore selectivity may be estimated via knowledge of the pI.

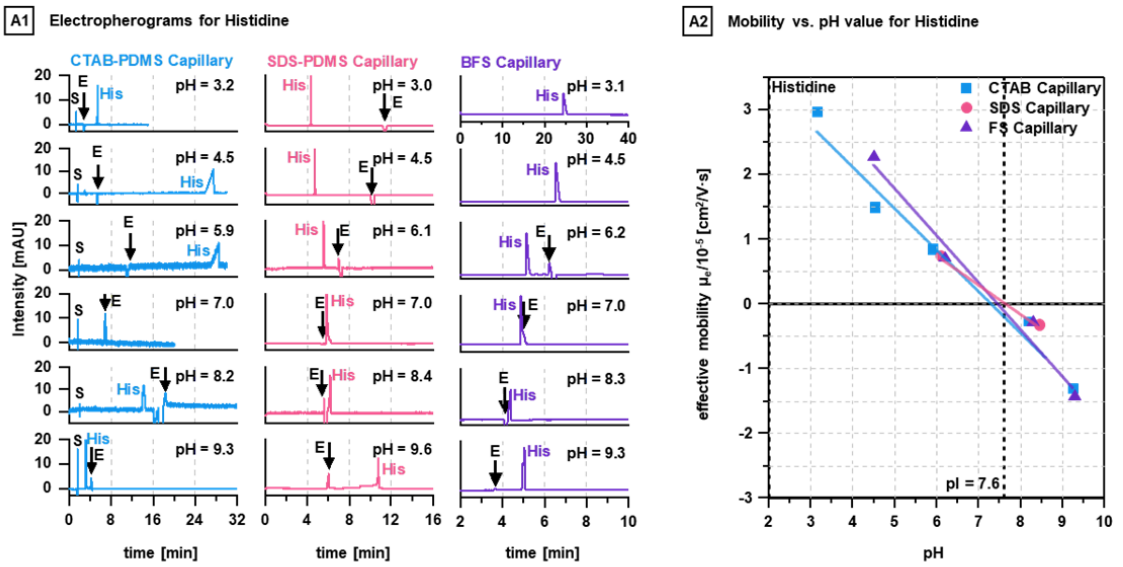

Figure 2-5: Systematic evaluation of the CTAB-PDMS, SDS-PDMS, and BFS capillary employing BGEs with pH values ranging from 3.0 to 9.6. The electropherograms (**A1**) were obtained at -30 kV for the CTAB-PDMS capillary and at +30 kV for the SDS-PDMS and BFS capillary. The arrows indicate the EOF (E) and system peaks are marked with a S. The tuneable manipulation of the selectivity may be monitored when plotting the analytes effective mobility against the pH value of the BGE (**A2**). A high consistency was observed across all three capillaries and a line of best fit crosses the x-axis at approximately the pI of the protein.

The same approach was used to evaluated Tf (pI 5.4) as shown in Figure 2-6 B1. Like His, the CTAB-PDMS system produced sharp symmetrical Tf peaks at pH 3.2 and 4.5 after the EOF, and at pH 5.9, 7.0, and 8.2 before the EOF. At pH 9.3, Tf was not detected, likely due to a global negative charge across the protein and electrostatic adsorption to the positively charged CTAB coating, or ion pair formation between the protein and free CTAB molecules from the dynamic coating formulation of the BGE. Tf was observed at BGE pHs above the pI of the protein after the EOF (counter EOF), with increasing peak symmetry with increasing pH for both the SDS-PDMS system and the BFS capillary. Interestingly, the peak symmetry in the SDS-PDMS system was generally superior to that of the BFS separation at the same pH, likely due to improved mitigation of hydrophobic adsorption. Again, the mobility of Tf was plotted against the pH of the BGEs and is shown in Figure 2-6 B2. As before, there was consistency of mobility within all three systems.

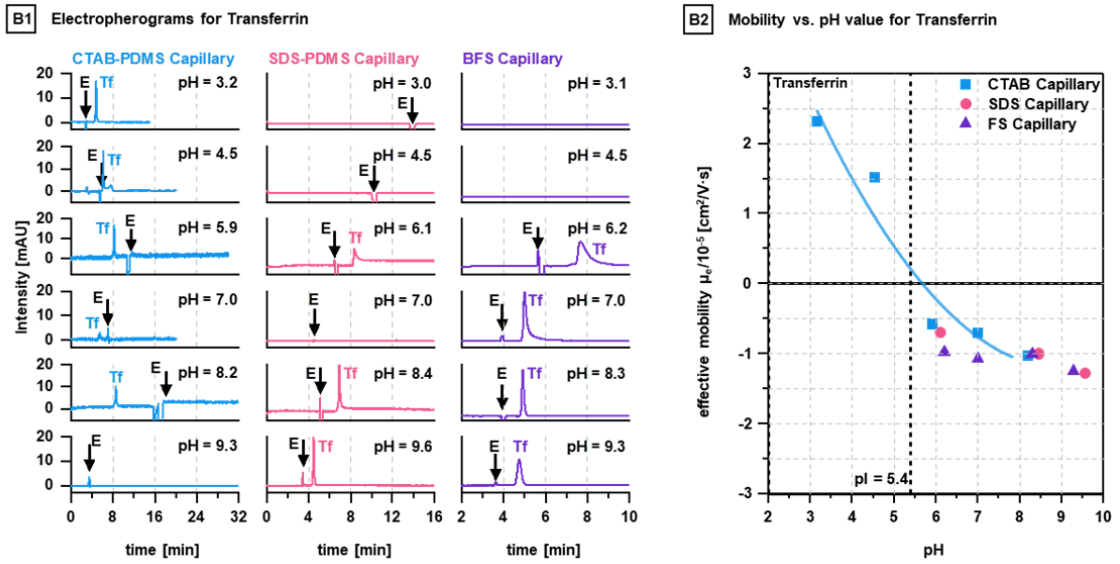

Figure 2-6: Electropherograms (**B1**) and mobility vs. pH value plots (**B2**) for Tf obtained with the CTAB-PDMS, SDS-PDMS, and BFS capillary employing BGEs with pH values ranging from 3.0 to 9.6. The arrows in the electropherograms indicate the EOF (E) and system peaks are marked with an S.

The workflow was applied to the selected panel of representative proteins that encompassed a range of MWs and pIs to demonstrate the universality of the BGEs and capillary combinations for the separation of any intact protein. Figure 2-7 to Figure 2-12 details the respective electropherograms and mobility vs. pH plots.

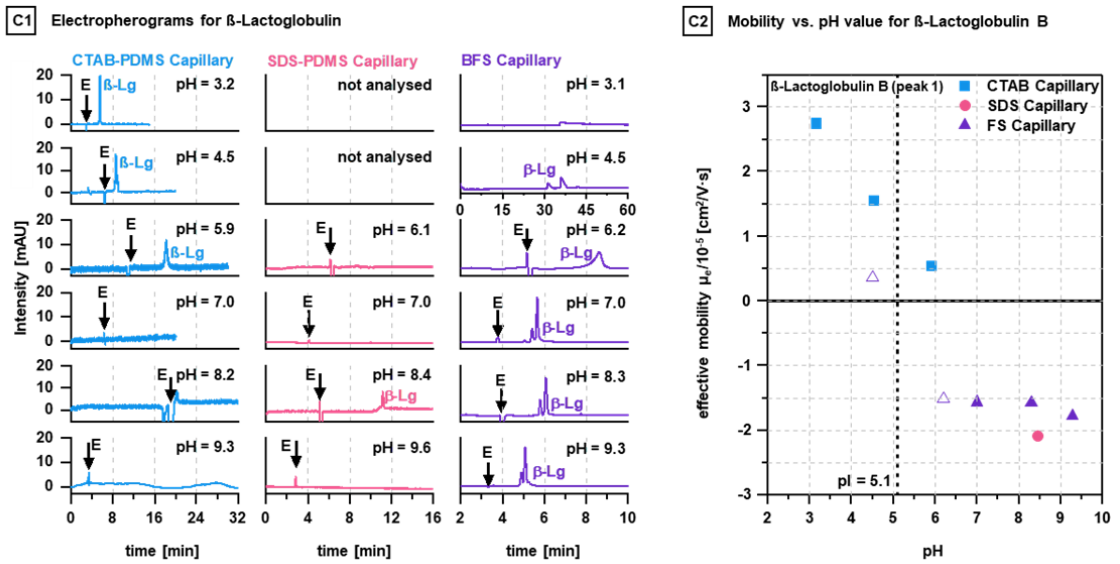

Figure 2-7: Electropherograms (**C1**) and mobility vs. pH value plots (**C2**) for β-Lg obtained with the CTAB-PDMS, SDS-PDMS, and BFS capillary employing BGEs with pH values ranging from 3.0 to 9.6. The arrows in the electropherograms indicate the EOF (E) and system peaks are marked with an S.

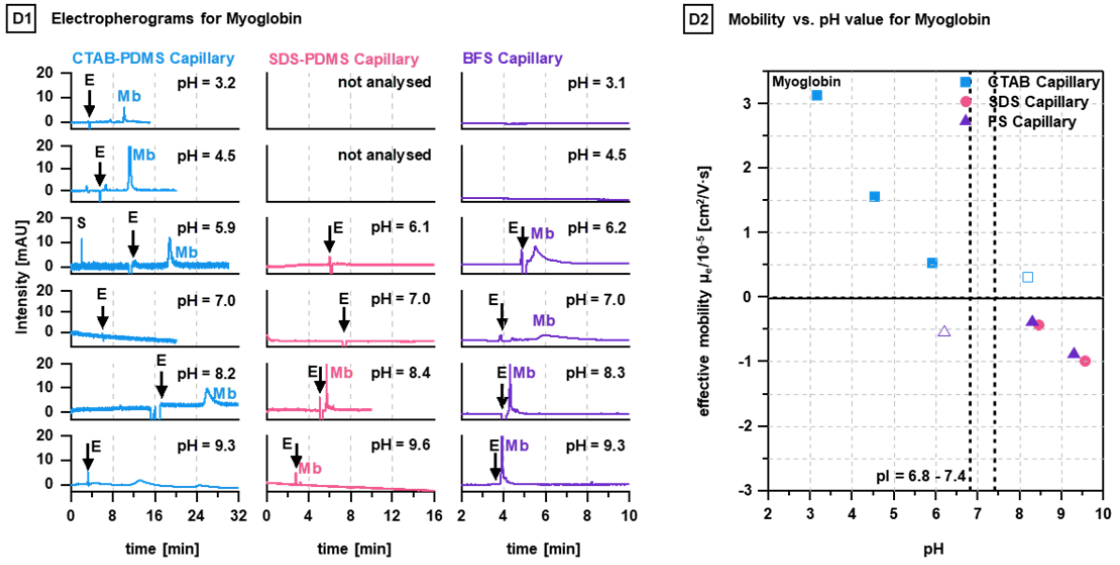

Figure 2-8: Electropherograms (**D1**) and mobility vs. pH value plots (**D2**) for Mb obtained with the CTAB-PDMS, SDS-PDMS, and BFS capillary employing BGEs with pH values ranging from 3.0 to 9.6. The arrows in the electropherograms indicate the EOF (E) and system peaks are marked with an S.

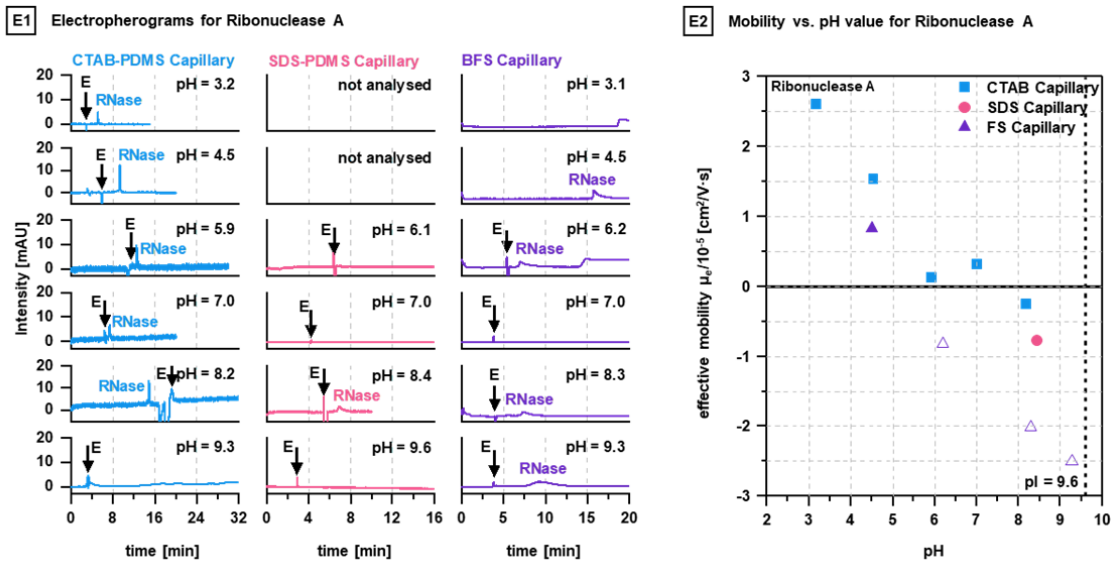

Figure 2-9: Electropherograms (**E1**) and mobility vs. pH value plots (**E2**) for RNAse obtained with the CTAB-PDMS, SDS-PDMS, and BFS capillary employing BGEs with pH values ranging from 3.0 to 9.6. The arrows in the electropherograms indicate the EOF (E) and system peaks are marked with an S.

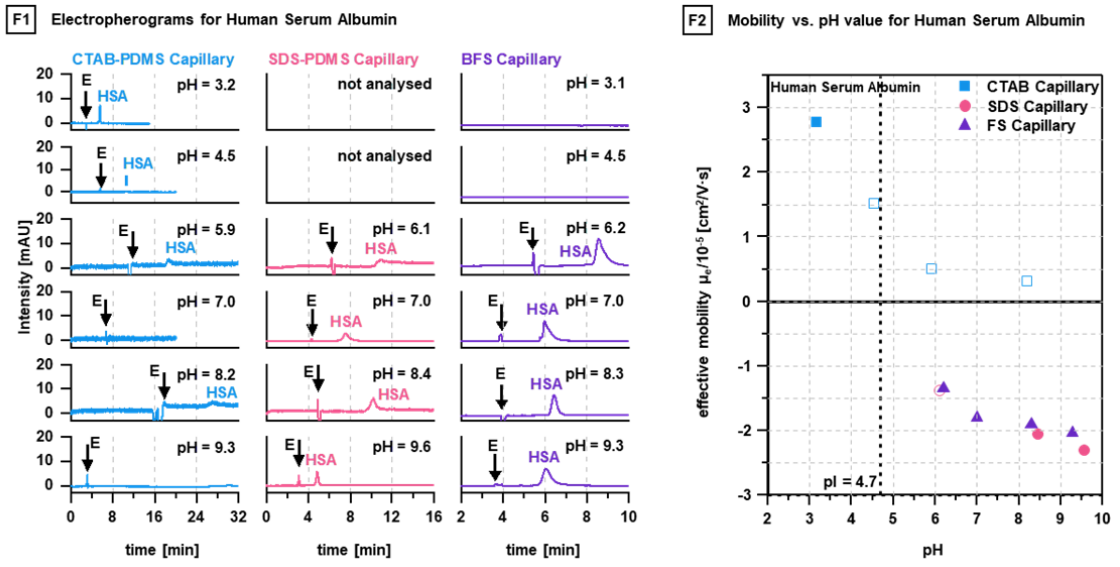

Figure 2-10: Electropherograms (**F1**) and mobility vs. pH value plots (F**2**) for HSA obtained with the CTAB-PDMS, SDS-PDMS, and BFS capillary employing BGEs with pH values ranging from 3.0 to 9.6. The arrows in the electropherograms indicate the EOF (E) and system peaks are marked with an S.

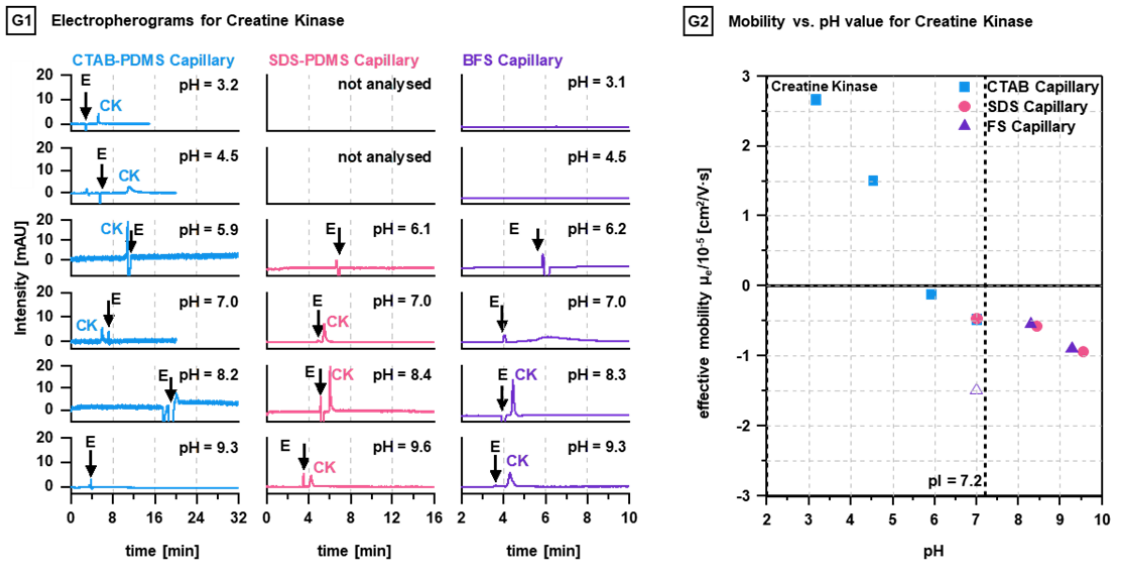

Figure 2-11: Electropherograms (**G1**) and mobility vs. pH value plots (**G2**) for CK obtained with the CTAB-PDMS, SDS-PDMS, and BFS capillary employing BGEs with pH values ranging from 3.0 to 9.6. The arrows in the electropherograms indicate the EOF (E) and system peaks are marked with an S.

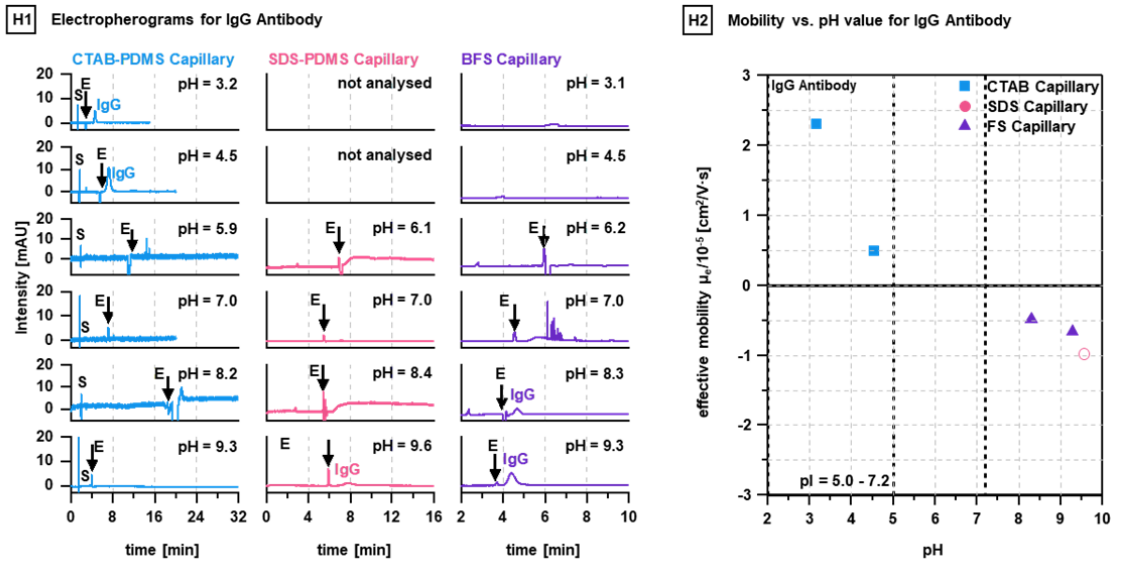

Figure 2-12: Electropherograms (**H1**) and mobility vs. pH value plots (**H2**) for IgG antibody obtained with the CTAB-PDMS, SDS-PDMS, and BFS capillary employing BGEs with pH values ranging from 3.0 to 9.6. The arrows in the electropherograms indicate the EOF (E) and system peaks are marked with an S.

Multiple suitable combinations of the three systems were apparent for all target proteins. As expected, the CTAB capillary was more suited to low pH BGEs,

whilst the SDS and BFS capillaries were superior at high pH as shown in Figure 2-13. For example, the peaks for HSA, Tf, and CK were symmetrical and adsorption free with the SDS-PDMS capillary. The BFS capillary was the better choice for all other analytes with sufficient efficiency for separation of the two isoforms of β-Lg A and β-Lg B. These differences were likely due to various interactions between the buffer components and the proteins. Regardless, the simple mechanism of separation proposed here is an effective practical approach for unprecedented control of EOF at all pH values, minimisation of unwanted adsorption of proteins, and facile method development and manipulation of selectivity.

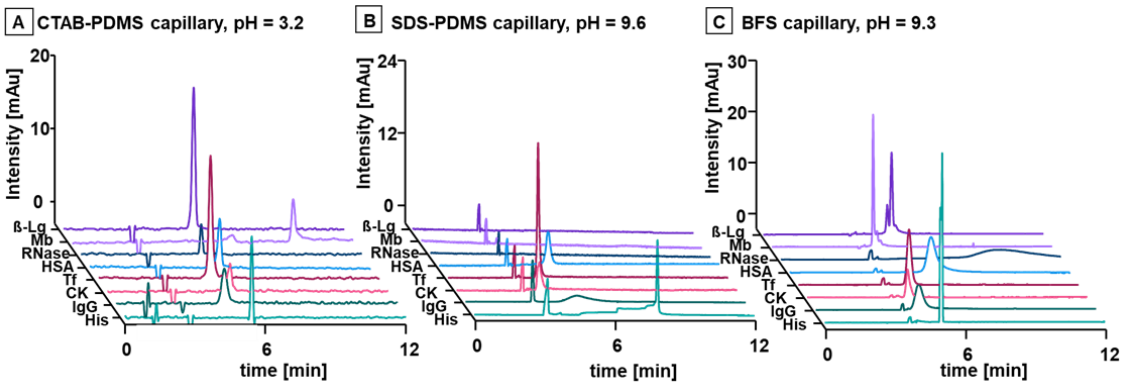

Figure 2-13: CE analysis of eight model analytes with various MWs and pIs at low (**A**, CTAB-PDMS capillary) and high pH (**B**, SDS-PDMS capillary; **C**, BFS capillary). A fast EOF and symmetrical peaks for all analytes were produced with the CTAB-PDMS capillary (**A**). The peaks HSA, Tf and CK were symmetrical and adsorption free with the SDS capillary (**B**). The BFS capillary was superior for all other analytes with a sufficient separation efficiency for the isoforms β-Lg A and β-Lg A (**C**).

2.3.4 Proof-of-principle: Analysis of proteins in milk

To showcase the possibilities to predict the behaviour and separation of proteins, the workflow was applied to the analysis of proteins in cow's milk. The total protein content of cow's milk typically varies between 3.0-3.5%, of which 80% are genetic variants of casein (CN) and 15% are whey proteins [210]. The major caseins are isoforms of α-casein (α-CN), β-casein (β-CN) and κ-casein (κ-CN) [211]. Prominent whey proteins are isoforms of α-lactalbumin A (α-Lac A) and β-Lg [212]. The pIs of these proteins range between 4.4 and 5.1 and are listed

together with their respective MWs in Table 2-4. Consideration of the proteins pIs and the outcomes of the systematic evaluation, indicated that the most suitable CE separation was a combination of an acidic BGE and the CTAB capillary.

Table 2-4: MWs and pIs for proteins identified in milk.

	Molecular weight [kDa]	**Isoelectric point**
α-Lactalbumin A (α-Lac A)	14.1 [213]	4.4 [190]
β-Lactoglobulin A (β-Lg A)	18.4 [213]	5.1 [190]
β-Lactoglobulin B (β-Lg B)	18.3 [213]	5.2 [190]
α-Casein (α-CN)	22.1-23.7 [213]	4.6 [214]
A1 β-Casein (A1 β-CN)	24.0 [213]	4.6 [214]
A2 β-Casein (A2 β-CN)	24.0 [213]	4.8-5.1 [213]
Bovine Serum Albumin (BSA)	66.3 [213]	4.7-4.9 [213]

Figure 2-14 A shows the analysis of the milk sample with BGE M-I (20 mM CA, 10 mM TRIS, 0.1 mM CTAB, pH 3.2) utilising a CTAB capillary with a total length of 110 cm and an effective length of 102 cm. The capillary length was extended to improve protein separation efficiency, and the BGE concentration was adjusted to maintain sufficient ionic strength for constant current (two-fold concentration compared to BGE I). The initial BGE M-I provided baseline separation of casein and whey proteins consisting of isoforms of A1 β-CN and A2 β-CN, BSA, α-CN and α-Lac. However, the two isoforms of β-Lg A and β-Lg B were only partially separated. The pIs of β-Lg A and β-Lg B are 5.1 and 5.2, slightly higher than the other proteins of interest. Accordingly, the pH of the BGE was increased to 3.8 (BGE M-II, 20 mM CA, 20 mM TRIS, 0.1 mM CTAB) to impart a charge difference

between the two isoforms. Baseline separation of β-Lg A and β-Lg B was observed with slightly less separation of the other components (Figure 2-14 B).

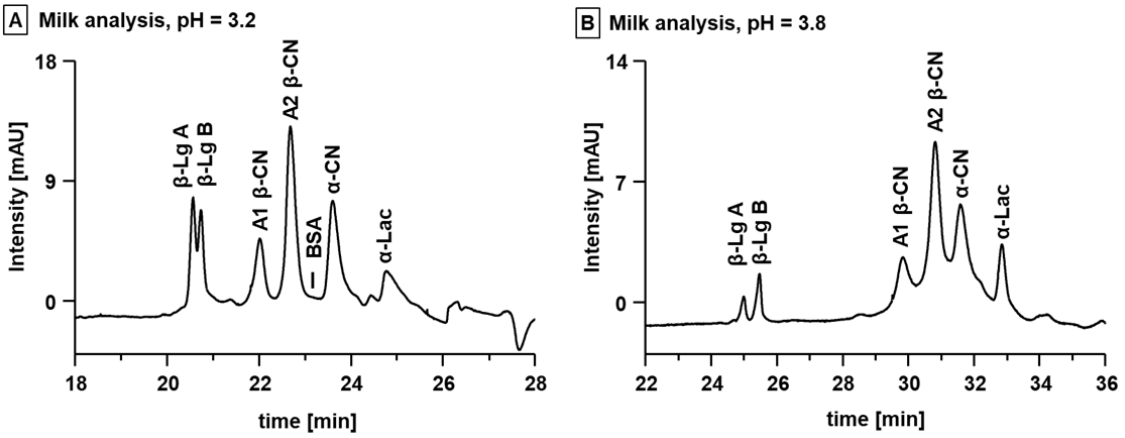

Figure 2-14: Simultaneous analysis of caseins and whey proteins in fresh cow's milk employing a CTAB-PDMS capillary (total length 110 cm, effective length 102 cm) and two BGEs. BGE M-I (pH 3.2) is suitable for the separation of the two isoforms A1 β-CN and A2 β-CN, BSA, α-CN and α-Lac (**A**). The analysis of the two isoforms β-Lg A and β-Lg B requires BGE M-II (pH 3.8) with a slightly higher pH value due the higher pI of the analytes (**B**).

The proteins in the milk sample were identified via spiking individual protein standards to the sample. The individual electropherograms are depicted in Figure 2-15.

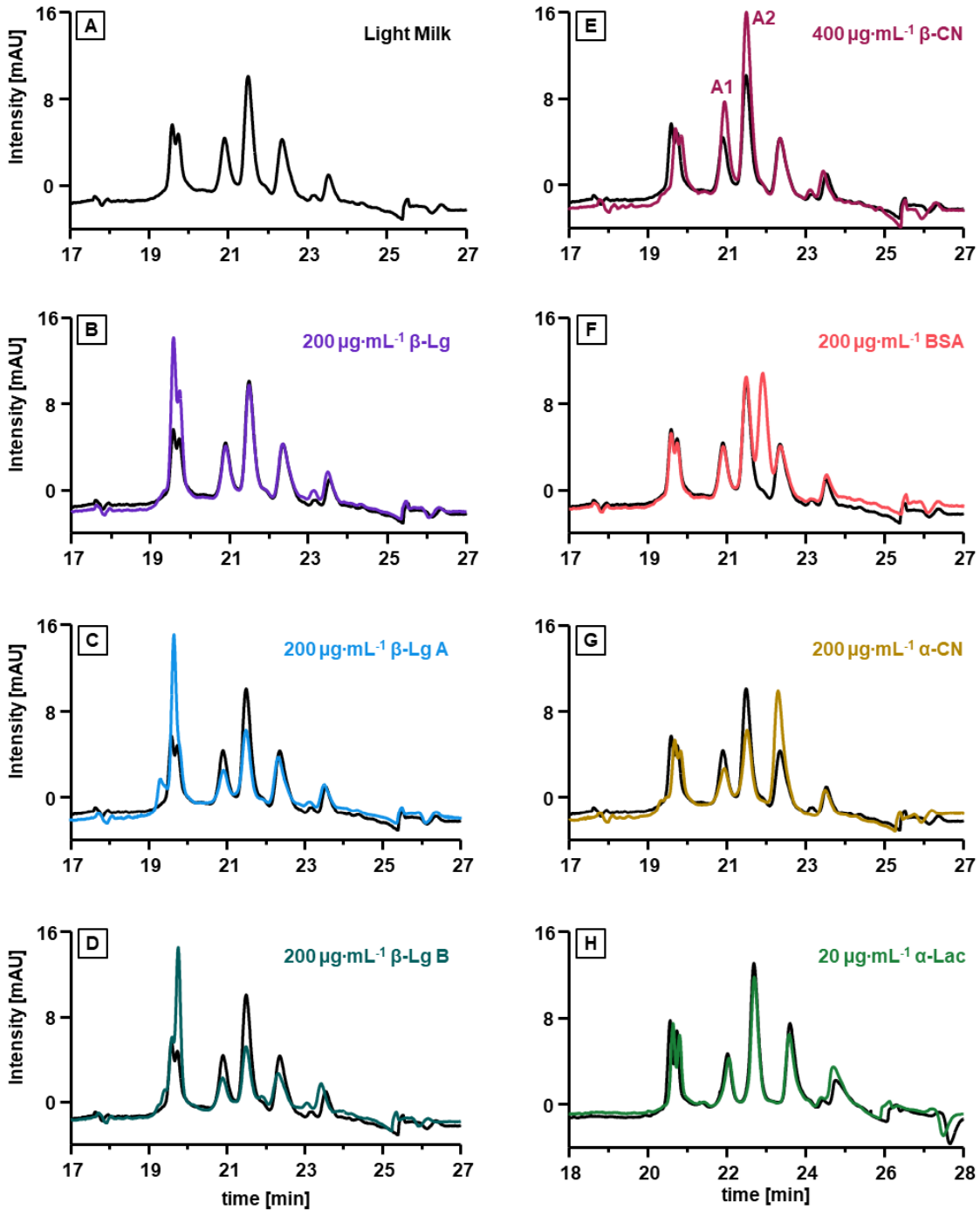

Figure 2-15: Protein identification in fresh cow's milk. The milk samples were spiked with the individual protein standards in their appropriate concentrations (**A-H**).

2.4 Conclusion

This chapter presented a novel and universal workflow for the analysis of intact proteins with any MW or pI via CE and introduced guidelines for the selection of appropriate BGEs based on the knowledge of the proteins' pI.

The suitability of GC PDMS capillaries with dynamic coatings of CTAB and SDS, and BFS capillaries were evaluated for the analysis of seven model proteins in six BGEs with pH values between 3.0-9.6. The CTAB-PDMS capillary was most suited for low pH BGEs with a low concentration of 0.1 mM CTAB added to the BGE. The SDS-PDMS capillary and BFS capillary were superior at high pH BGEs, with 0.01 mM SDS added to the BGE for the SDS-PDMS capillary. Multiple capillary and BGE combinations were applicable for separation of each of the model proteins with MWs between 13.7-150 kDa and pIs ranging from 4.7-9.6.

The proteins' effective mobility was plotted against the BGEs pH value, and a line of best fit crossed the x-axis at approximately the pI of the protein, while fast mobilities were observed at pH values distant from the proteins pI. This was consistent across all capillaries, indicating that the electrophoretic mobility and therefore selectivity may be estimated via knowledge of the pI.

Finally, the guidelines were used to select the most suitable capillary-BGE combination for the analysis of caseins and whey proteins in cow's milk.

Chapter

Development of a CE-ICP-MS Interface

Based on:

Sarah Meyer, David Clases, and Philip A. Doble, *A Simple, Low-Cost and Robust CE-ICP-MS Interface for the Analysis of Gadolinium-based Contrast Agents in Biological Samples*, in preparation.

3.1 Introduction

The sensitivity of CE with UV or conductivity detection is often not suitable for the analysis of limited volume and complex biological samples. Hyphenation of CE with highly sensitive detectors such as ICP-MS potentially opens a new vista of applications in the biosciences including the measurement of NPs, exogenous metals, metallo-therapeutics, as well as quality assurance of protein tagging protocols (the limits of detection (LODs) for the individual detectors are 10^{-5}-10^{-8} mol·L^{-1} for UV, 10^{-7}-10^{-8} mol·L^{-1} for conductometry, and 10^{-8}-10^{-9} mol·L^{-1} for MS) [196]. However, coupling these two modalities is challenging as many experimental aspects require careful consideration to ensure compatible nebulizer flow rates, appropriate selection of capillary dimensions, mitigation of nebulizer back pressures, and reliable electrical connections. Accordingly, this chapter addresses Aim 2, the development of a simple and robust CE-ICP-MS interface. Here, we selected gadolinium-based contrast agents (GBCAs) as model compounds to evaluate the performance of the interface and measured the excretion profile in urine of the commonly administered liver specific GBCA gadoxetic acid in a 27-year-old healthy female patient.

MRI is an invaluable and established method for medical diagnostics allowing generation of non-invasive images of the body [215]. More than 30 million of all MRI examinations worldwide are assisted using GBCAs. The first GBCA, gadopentetic acid (Gd-DTPA, Magnevist®) entered the global marked in 1988 with several more gadolinium chelates following in later years [216]. These include generic contrast agents such as gadoteric acid (Gd-DOTA, Dotarem®), gadobutrol (Gd-BT-DO3A, Gadovist®), and gadodiamide (Gd-DTPA-BMA, Omniscan®), and other GBCAs specifically for imaging the liver such as gadoxetic acid (Gd-EOB-DTPA, Primovist® in Europe, Eovist® in the USA) [217]. The molecular structures of these GBCAs are depicted in Figure 3-1.

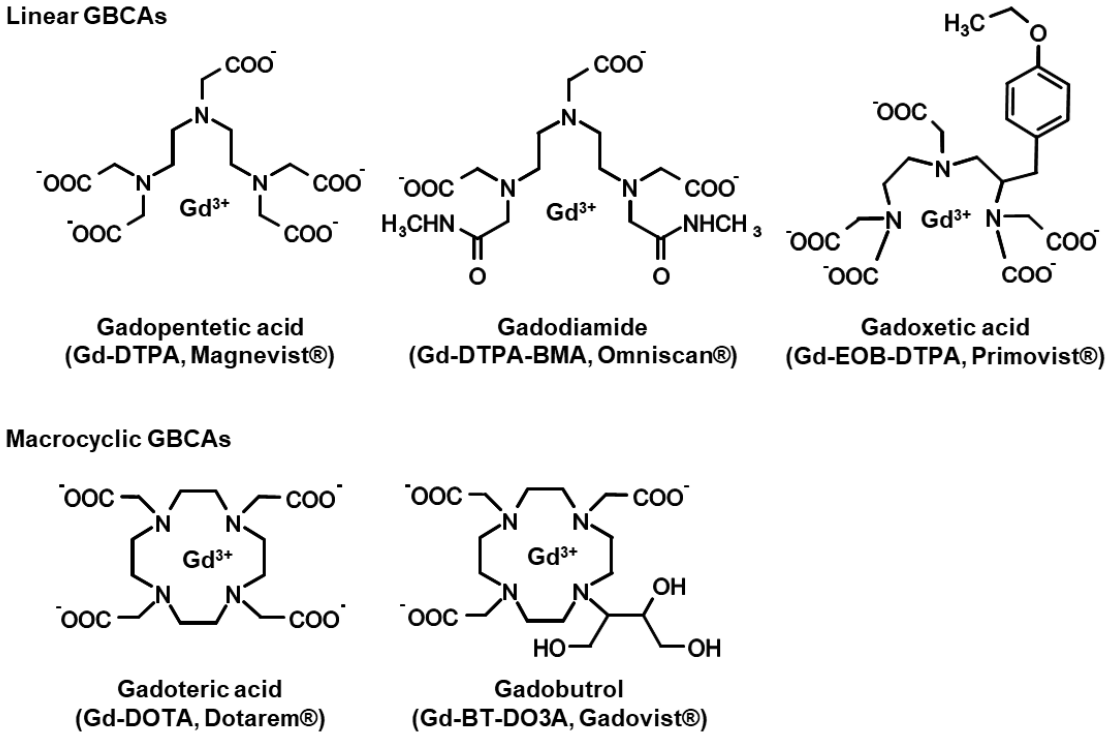

Figure 3-1: Molecular structures of the GBCAs used in this study. Gadopentetic acid, gadodiamide, and gadoxetic acid are linear complexes (**top**). Gadoteric acid and gadobutrol and are macrocyclic chelates (**bottom**).

Most GBCAs are administered intravenously during the MRI investigation and are excreted predominantly unmetabolised by glomerular filtration in the kidneys. The plasma half-live for the generic GBCAs is about 96 minutes (gadopentetic acid) in healthy individuals, while the plasma half-life of gadoxetic acid is 56 minutes. This liver-specific contrast agent is excreted via two pathways, the biliary and the renal route, which accounts for its faster elimination. [217–220] GBCAs have generally been considered safe for patients with normal kidney function, however there are numerous reports of nephrogenic systemic fibrosis (NSF) in patients suffering from end-stage renal failure [221]. Recent studies have proposed that there is a risk of gadolinium retention in healthy people, requiring sensitive and specific methods to monitor excretion profiles for at-risk individuals [221–225]. Various approaches are been described for GBCA analysis in biological and environmental samples and include imaging techniques [226–229], chromatographic [169,230], and electrophoretic separations [231–233].

CE-ICP-MS combines the advantages of CE, including a high separation efficiency, wide mass range, and low sample/solvent consumption with the excellent selectivity, sensitivity, and fast response time of ICP-MS. The large number of available separation modes, the various compatible background electrolytes with different pH values, and facile sample pre-treatment makes CE-ICP-MS the ideal method for the analysis of metals and their complexes in a multitude of biological matrices [101,105]. ICP-MS also allows compound-independent calibration (CIC) and quantification, bypassing the requirement for specific, inaccessible, or expensive standard materials [234]. Since the signal is proportional to the number of metal atoms present in a molecule, derivates of the target compound, small organic molecules [235], or inorganic salts [236,237] may be used for CIC.

Unlike facile coupling of other separation modalities such as HPLC or GC, hyphenation of CE and ICP-MS is challenging [101]. The three main considerations [238] are: (1) a CE-ICP-MS interface must maintain an effective electrical connection for stable current during electrophoretic separations, (2) the interface must balance the EOF rate with the nebulizer's specifications for production of an homogeneous aerosol, and (3) the CE-ICP-MS interface must inhibit laminar flows that arise from nebulizer pressure effects. Since the first CE-ICP-MS interface was published by Olesik *et al.* in 1995 [108], many researchers have advanced new designs and approaches to address the above considerations. These advances have been comprehensively reviewed by numerous authors [101,130–134], and generally consist of laboratory built prototypes or commercial offerings such as the CETAC CEI-100 Nebulizer [122,123], the Burgener MiraMist Nebulizer [124], and the Meinhard DIHEN [117].

CE-ICP-MS has been applied to elemental speciation [107,239,240], the study of element-ligand interactions [241–243], and indirect analysis of non-metallic compounds [244–246]. However, CE-ICP-MS has not been used for the simultaneous analysis of GBCAs in biological matrices. Accordingly, this chapter describes the development of a simple, easy to set up, low maintenance, cost

effective, and robust CE-ICP-MS interface that may be used for a variety of applications in the biosciences, including the characterisation of metal tagged proteins. We developed a method for simultaneous analysis of five commonly used GBCAs as model compounds, addressed the above considerations via modification of the commercial CEI-100, and demonstrated performance and functionality by compound-independent quantification of gadoxetic acid in urine samples after MRI examination.

3.2 Experimental section

3.2.1 Chemicals and consumables

Ultrapure water was obtained from an Arium® pro system from Sartorius Stedim Biotech (18.2 MU, Göttingen, Germany). The high purity lutetium standard for ICP-MS at 10 $mg \cdot L^{-1}$ was acquired from Choice Analytical (Thornleigh, NSW, Australia). The GBCAs were obtained from their respective pharmaceutical suppliers: gadoteric acid (Gd-DOTA, Dotarem®, 0.5 $mol \cdot L^{-1}$) from Guerbet SA (Villepinte, France), gadobutrol (Gd-BT-DO3A, Gadovist®, 1.0 $mol \cdot L^{-1}$), and gadopentetic acid (Gd-DTPA, Magnevist®, 0.5 $mol \cdot L^{-1}$) from Bayer Pharma AG (Berlin, Germany), and gadodiamide (Gd-DTPA-BMA, Omniscan®, 0.5 $mol \cdot L^{-1}$) from GE Healthcare (Chalfont St Giles, United Kingdom). Sodium tetraborate decahydrate was acquired from Sigma Aldrich (Castle Hill, New South Wales, Australia). The BFS capillaries (50 µm ID, 365 µm OD; 75 µm ID, 150 µm OD; and 75 µm ID, 365 µm OD) were purchased from Polymicro Technologies (Phoenix, AZ, USA). MicroTee PEEK 1/32” and NanoTight™ Sleeves were obtained from IDEX Health & Science (Oak Harbour WA, USA). PEEK tubing was acquired from Trajan Scientific Australia Pty Ltd (Ringwood, VIC, Australia). The stainless-steel union purchased from (Agilent Technologies (Santa Clara, CA, USA). Water and urine samples were kept in containers made of polypropylene to avoid adsorption effects of GBCAs.

3.2.2 Instrumentation

Figure 3-2 shows the in house-built CE-ICP-MS interface. All CE separations were performed on an Agilent CE 7100 system (Agilent Technologies, Santa Clara, CA, USA) using a 100 cm BFS capillary (Polymicro Technologies, Phoenix, AZ, USA) with 50 µM ID and 375 µM OD. The make-up flow was introduced and controlled using an OB1 MK3+ Microfluidic Flow Controller (Elveflow, Paris, France) and passed through a stainless-steel union which functioned as an electrode. The flow from the CE capillary, the make-up flow, and the nebulizer were connected with a T-piece. The lengths of the BFS capillaries (75 µM ID, 375 µM OD) between the stainless-steel union and the T-piece, and the nebulizer and the T-piece were 7.5 cm and 4.8 cm, respectively. A CEI-100 (Teledyne CETAC Technologies, Omaha, CE, USA) was equipped with a 75 µM ID, 150 µM OD BFS capillary with a length of 4.4 cm and used for nebulization. The analytes were detected with an 8900 series ICP-MS system (Agilent Technologies, Santa Clara, CA, USA) utilising nickel cones, s-lenses, and a torch with an injector with a diameter of 2.0 mm. The cones were cleaned twice per week.

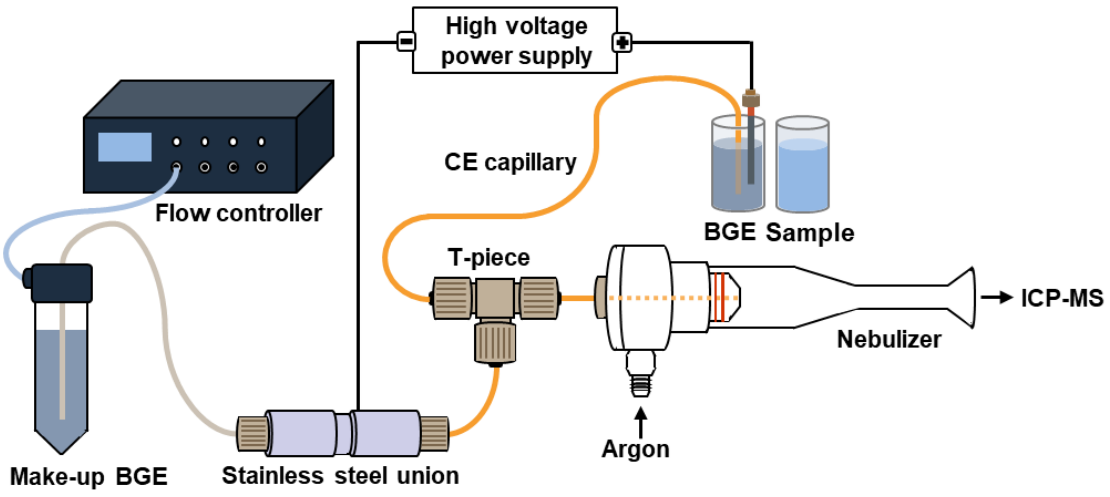

Figure 3-2: CE-ICP-MS schematic.

3.2.3 Method information

The CE analyses were carried out on a BFS capillary (total length: 100 cm, 50 µM ID, 375 µM OD) using a 5 mM sodium tetraborate BGE (pH 8.7). The cassette temperature was 30 ºC and the sample storage was 20 ºC. The capillary was rinsed for 3 minutes with the BGE before each analysis, the samples were injected hydrodynamically by applying pressure at 97 mbar for 10 s, and the separation was performed at +30 kV producing an average current of 4 µA. The make-up flow consisted of 5 mM sodium tetraborate and 100 $mg \cdot L^{-1}$ lutetium to monitor the liquid introduction and nebulization efficiency during method optimization and quantification. The optimum flow rate was determined empirically by testing different pressures applied to the BGE reservoir of the OB1 MK3+ system. In the range of 300 mbar to 700 mbar, the most suitable flow rate was determined to be 460 $nL \cdot min^{-1}$ (500 mbar) considering peak width, resolution, and analysis time.

For ICP-MS analysis, Ni cones, s-lenses, and a quartz injector torch (2.0 mm ID) were used. The applied tune parameters were the following: RF power: 1600 W; RF matching: 1.24 V; nebulizer gas flow: 1.2 $L \cdot min^{-1}$; monitored isotopes: ^{152}Gd, ^{154}Gd, ^{155}Gd, ^{156}Gd, ^{157}Gd, ^{158}Gd, ^{160}Gd, ^{175}Lu; dwell time for isotopes: 100 ms.

3.2.4 Standard and sample preparation

For method optimization, the respective GBCA standard solutions were diluted in ultrapure water to a concentration of 1000 $\mu g \cdot L^{-1}$. For species identification and the construction of calibration curves, the gadodiamide, gadobutrol, gadoteric acid, and gadopentetic acid standard solutions were diluted in ultrapure water to concentrations of 50, 100, 500, 750, 1000, 1500 and 2000 $\mu g \cdot L^{-1}$. All standards were prepared fresh daily to prevent metal exchange reactions. Ultrapure water was used to acquire a blank value.

The urine samples were obtained from a single volunteer (female, 27 years old) after MRI examination. During the MRI scan, The GBCA gadoxetic acid (Gd-

EOB-DTPA, Primovist®) was administrated to the patient intravenously in standard dose of 0.25 mol·L^{-1} (10 mL). The samples were collected in 50 mL polypropylene containers in two-hour time intervals and stored at 8 °C. Upon arrival in the laboratory the samples were aliquoted and stored at -20 °C until analysis. Prior to the quantification, the samples were defrosted and diluted in ultrapure water to fit into the calibration range. The analyses were conducted at UTS under the UTS HREC 2021-6815 ethics approval.

3.2.5 Data analysis

Data evaluation was performed using MassHunter software (Agilent Technologies) and OriginPro (OriginLab, Version 9). All data obtained was smoothed using the Savitzky-Golay filter with a filter width of 20 data points prior to further processing. The LODs and limits of quantification (LOQs) were determined using the equations 3.1 and 3.2, where σ_{S_N} was the standard deviation of the noise, and *s* the slope of the regression line. The EOF velocity v_{EOF} was calculated with equation 3.3, where $t_{mig,\ EOF}$ was the migration time of the EOF, r was the radius of the capillary, and L_{tot} was the total capillary length.

$$LOD = \frac{3\,\sigma_{S_N}}{s} \tag{3.1}$$

$$LOQ = \frac{10\,\sigma_{S_N}}{s} \tag{3.2}$$

$$v_{EOF} = \frac{t_{mig,\ EOF}}{\pi\, r^2\, L_{tot}} \tag{3.3}$$

3.3 Results and discussion

3.3.1 Interface design

The design of the CE-ICP-MS interface is shown in Figure 3-3. A make-up BGE was passed through a stainless-steel union which served as an electrode for stable current. The capillaries inside the stainless-steel union were assembled with a small gap that formed a reservoir to establish good electrical contact. The make-up flow was necessary to ensure that the total flow entering the nebulizer produces a consistent and stable aerosol. The make-up flow rate was regulated with a flow controller that applied specified pressures to a conical centrifuge tube reservoir. The lowest pressure (and make-up flow rate) was defined by current instability, whilst the upper limit was determined by excessive run times and injection pressure limitations. A T-piece was used to connect the end of the electrophoresis capillary perpendicular to that of the make-up flow capillary. The ends of the BFS capillaries at the T-piece were polished for precise connection that minimised dead volume. The capillaries lengths were minimised to mitigate band broadening and maintain resolution. This combined flow was directed to a CETAC CEI-100 total consumption nebulizer. The interface was kept in place via a customised 3D printed frame (Figure 3-3), consisting of an electrode holder, a bay for the T-piece and a locking nut where the holder was attached to the nebulizer. The total weight of the interface holder was minimised to reduce lateral forces on the glass nebulizer.

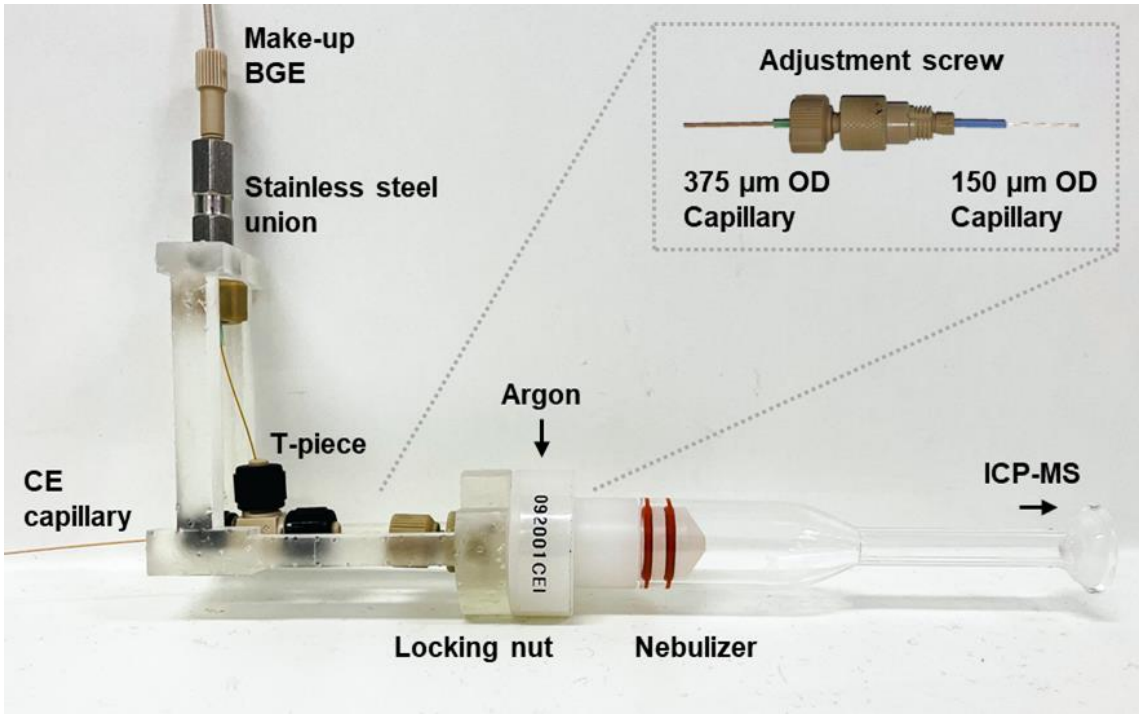

Figure 3-3: CE-ICP-MS interface kept in place with a 3D printed mounting.

The CETAC CEI-100 total consumption nebulizer was fitted with a 75 µM ID, 150 µM OD BFS capillary to minimise the backpressure on the separation and make-up flow capillaries. All transfer and nebulizer capillary ends within the CEI-100 were polished and carefully assembled for optimal sample transport into the ICP-MS. The capillary position inside the nebulizer was adjusted by monitoring the signal intensity and noise using a 100 $mg \cdot L^{-1}$ lutetium solution introduced via the make-up flow. The screw varying the capillary position inside the nebulizer was slowly turned until a uniform aerosol without sputtering was produced, and the position was hold in place with the locking nut. The most efficient nebulization was produced when the internal capillary was flush against the glass outlet of the nebulizer and the optimal nebulizer gas flow rate was 1.2 $L \cdot min^{-1}$.

3.3.2 Method optimization

Operating the CE system with a 100 cm BFS capillary and a 5 mM tetraborate BGE at +30 kV produced a stable current and suitable conditions for the separation of the GBCAs. The combined EOF and make-up flow must operate at a flow rate that was suitable for the nebulizer (<10 $\mu L \cdot min^{-1}$) [247]. Accordingly, various pressures were applied to the falcon tube reservoir whilst monitoring electrophoretic current and aerosol stability. Figure 3-4 shows the influence of various make-up flow rates between 300 and 650 mbar upon the separation of the three GBCAs gadodiamide (1, blue), gadobutrol (2, purple), and gadopentetic acid (3, teal) at 1000 $\mu g \cdot L^{-1}$. The split peak for gadodiamide in the electropherograms is due to the compound migrating with the EOF. Increasing the make-up flow pressure produced a concomitant increase in resolution of the three analytes due to increasing backpressure on the separation capillary, and increased EOF migration time. Increasing the make-up flow rate reduced the volume of the injected sample which resulted in decreased peak areas and heights. The injection pressure applied to the inlet needs to be sufficiently high to overcome the backpressure produced by the make-up flow. Considering the resolution, analysis time, and peak shapes a flow rate of 460 $nL \cdot min^{-1}$ (500 mbar) was selected for the GBCA analysis. According to equation 3.3, the EOF velocity was at least 325 $nL \cdot min^{-1}$ under these conditions. However, the equation did not account for the pressure from the make-up flow, resulting in an underestimation of the EOF flow rate.

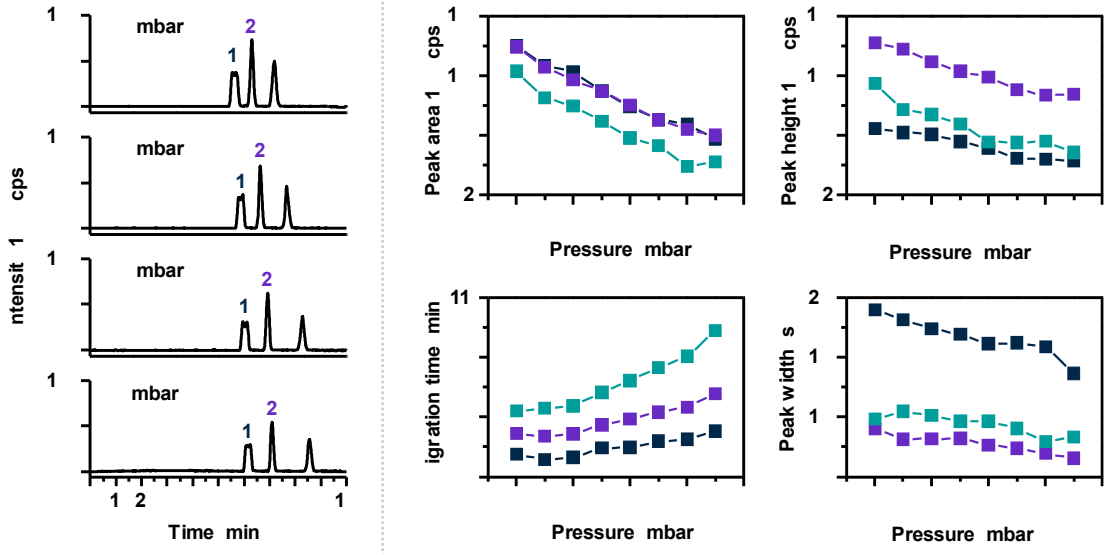

Figure 3-4: Optimization of the make-up flow rate using a 1000 mg·L^{-1} mix containing gadodiamide (**1, blue**), gadobutrol (**2, purple**), and gadopentetic acid (**3, teal**).

The injection parameters were optimised using the same GBCA solution containing gadodiamide (1, blue), gadobutrol (2, purple), and gadopentetic acid at 1000 µg·L^{-1}. Again, the split peak for gadodiamide in the electropherograms is caused by the compound migrating with the EOF. While the injection pressure was set to its maximum of 97 mbar, the injection time was varied between 10 s and 40 s. Figure 3-5 summarises the influence on resolution, peak shapes, and retention time. As expected, the peak areas and heights, and therefore the LOD and LOQ, improved with increasing injection time. However, the peak width and resolution deteriorated when the injection time was longer than 20 s, and the migration times reduced, most likely because a substantial portion of the capillary was filled with the sample. The optimal conditions were selected at 97 mbar for 10 to 20 s.

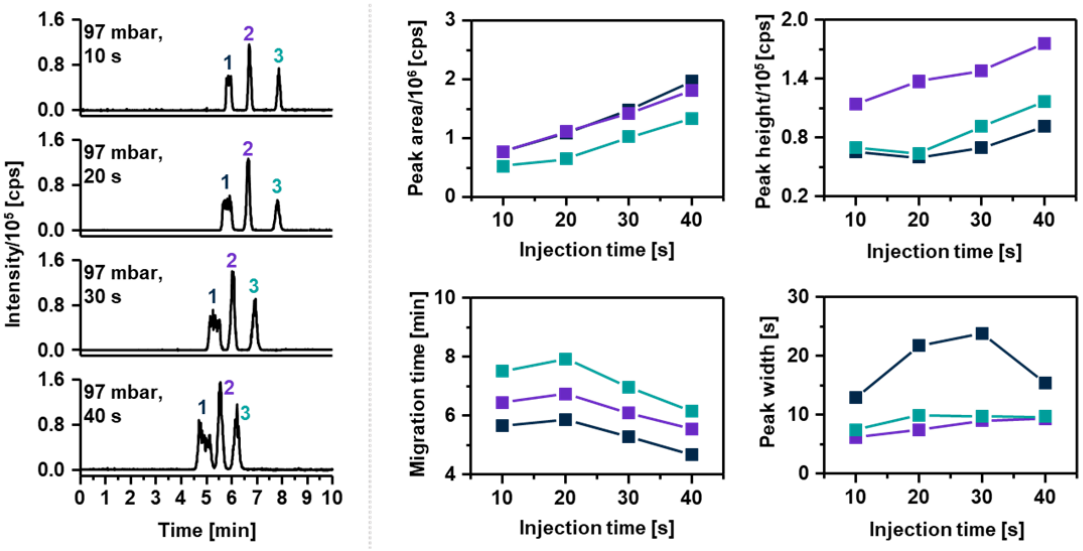

Figure 3-5: Optimization of the injection conditions using a 1000 mg·L^{-1} mix containing gadodiamide (**1, blue**), gadobutrol (**2, purple**), and gadopentetic acid (**3, teal**).

3.3.3 GBCA quantification in urine samples

The CE-ICP-MS interface and optimised method was used for the quantification of gadoxetic acid in urines samples. The samples originated from a patient with healthy kidney function and were collected in two-hour time intervals after MRI examination. Gadoxetic acid is a linear chelate which is specifically used for MRIs of the liver and is, equally to other GBCAs, excreted mostly unmetabolised. The gadoxetic acid content was analysed via CIC employing the four most frequently administered GBCAs gadodiamide, gadobutrol, gadoteric acid, and gadopentetic acid. The suitability of the CE-ICP-MS method regarding the separation power and linearity was demonstrated by spiking the four GBCA standards at a suitable concentration to a diluted urine sample as well as by obtaining calibration curves. Figure 3-6 shows the obtained electropherograms with five resolved peaks for gadodiamide (**1**), gadobutrol (**2**), gadoteric acid (**3**), gadoxetic acid (**4**), and gadopentetic acid (**5**) in less than 10 minutes.

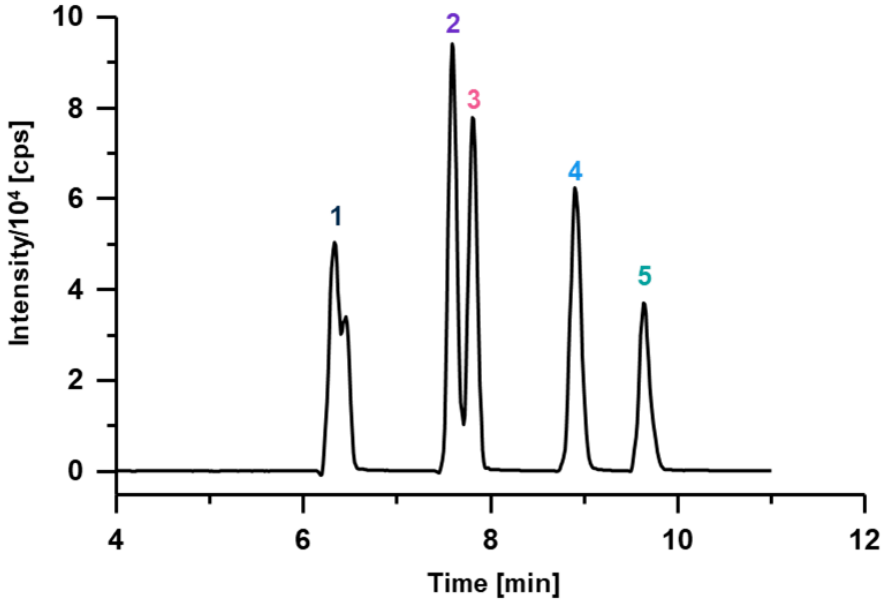

Figure 3-6: Separation of a 600 mg·L^{-1} mix of the GBCAs gadodiamide (**1**), gadobutrol (**2**), gadoteric acid (**3**), and gadopentetic acid (**5**) spiked to the gadoxetic acid (**4**) containing urine sample. The sample was injected hydrodynamically (97 mbar for 10 s). The analysis was performed at +30 kV with a 5 mM sodium tetraborate BGE and a make-up flow rate of 4.6 µg·min^{-1} (500 mbar).

The figures of merit for the four GBCA standards are summarised in Table 3-1. The R^2 values ranged between 0.9941 and 0.9984. The LODs were between 22 and 29 ng·L^{-1} and the LOQ ranged between 72 and 96 ng·L^{-1}.

Table 3-1: Figures of merit for each GBCA standard.

	R^2	**LOD [ng·L^{-1}]**	**LOQ ng·L^{-1}]**
gadodiamide	0.9981	22	72
gadobutrol	0.9984	25	83
gadoteric acid	0.9941	25	83
gadopentetic acid	0.9972	29	96

The feasibility of employing CIC was validated by reciprocal external quantification of the four GBCA standards in three concentrations positioned at the lower, medium, and higher end of the calibration curve. Table 3-2 shows the calculated recoveries for the compound-independent (black) and compound-specific (bold, red) quantification. The recoveries ranged between 84 and 102% with the best recoveries achieved using the latter two analytes gadoteric acid and gadopentetate dimeglumine. No significant difference was observed between the two quantification strategies.

Table 3-2: Calculated recoveries using species-unspecified (black) and species-specific (bold, red) quantification.

	Recovery [%] determined using			
	gadodiamide	**gadobutrol**	**gadoteric acid**	**gadopentetic acid**
gadodiamide	**91**	82	86	84
gadobutrol	99	**90**	94	91
gadoteric acid	103	92	**96**	94
gadopentetic acid	106	93	97	**97**

Since the CIC was verified to be suitable, the four GBCAs standard were used to determine the gadoxetic acid content in urines samples. For quantification, the six urine samples were diluted accordingly to fit in the range of the calibration curve. All calculated concentrations showed a gadoxetic acid excretion profile as shown in Figure 3-7. The excretion profile was fitted with an exponential curve with the highest amount of gadoxetic acid excreted within the first 2 hours. The determined GBCA concentration in urine was influenced by hydrations levels, which explained the anomalous point at 6 hours collection. Regardless, the profile was consistent with pharmacokinetic expectations [248].

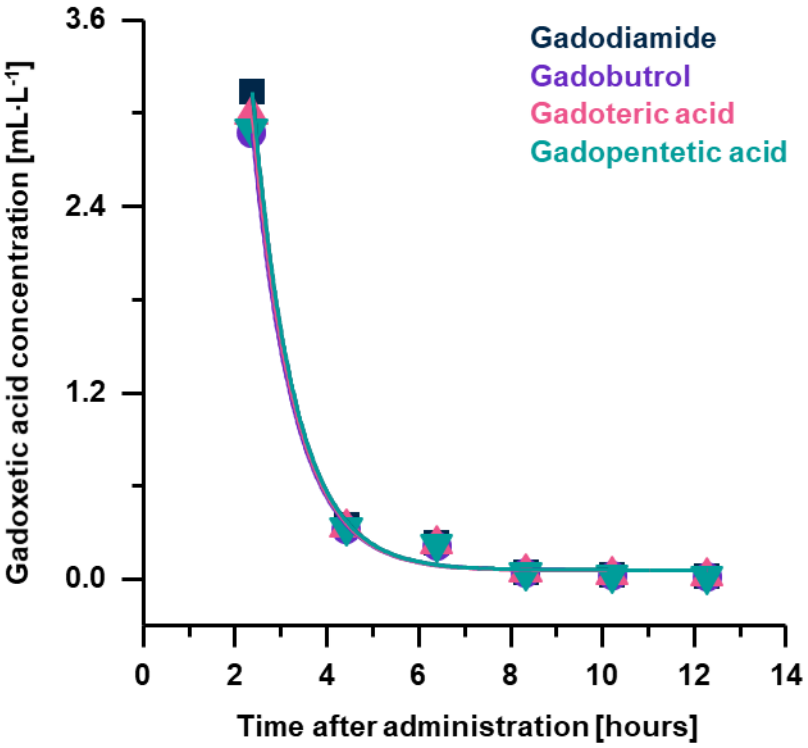

Figure 3-7: Excretion profile of gadoxetic acid in urine over a time of 12 hours, with sample collection performed every 2 hours. The gadoxetic acid content was quantified via external calibration using gadodiamide (**blue**), gadobutrol (**purple**), gadoteric acid (**magenta**), and gadopentetic acid (**teal**). The determined gadolinium gadopentetic acid concentration showed a good compliance using the four different GBCAs.

3.4 Conclusion

In this chapter, a simple, low maintenance, and robust CE-ICP-MS interface was developed which may be used for numerous applications in the biosciences. A commercial CEI-100 nebulizer was fitted with a 75 µM ID, 150 µM OD BFS capillary to minimise the backpressure on the separation and make-up flow capillaries. The remaining parts of the interface were optimised via consideration of make-up flows and electrical contacts.

A fast and sensitive method for the simultaneous analysis of five commonly used GCBAs, namely gadodiamide, gadobutrol, gadoteric acid, gadoxetic acid, and gadopentetic acid, was developed and separated the compounds in less than

10 minutes. Excellent figures of merit were obtained with R^2 values ranging between 0.9941 and 0.9984, LODs between 22 and 29 $ng \cdot L^{-1}$, and LOQs between 72 and 96 $ng \cdot L^{-1}$.

The interface's functionality and performance were demonstrated by compound-independent quantification of gadoxetic acid in six urine samples collected after MRI examination. Four different GBCAs were used for quantification of gadoxetic acid and the resulting excretion profile shows high consistency between all GBCA standards. The highest amount of gadoxetic acid was excreted within the first two hours and the profile was consistent with pharmacokinetic expectations.

Chapter

Characterisation of Metal Labelled Antibodies by CE-ICP-MS

4.1 Introduction

Protein expression is often measured by immunoassays utilising metal conjugated antibodies and forms the basis of mass cytometry and various imaging methods, including iMSI. However, the number of metal tags per antibody can differ significantly, confounding the comparison of expression levels within and between samples. This chapter synergistically combines the advancements made in the previous two chapters and addresses Aim 3, the characterisation of metal labelled antibodies via CE-ICP-MS; and lays the foundation for improved reliability and appropriately validated methods.

The function of many physiological processes is controlled by the up- and downregulation of specific proteins [51,249]. These complex biological pathways are strictly controlled within organisms, and their analyses require highly sensitive methods to simultaneously detect several proteins in a sample [181,250]. Contemporary techniques involve immunoassays with metal labelled antibodies, where the concentration of the antibody-metal conjugate is proportional to that of the target protein. The metal tags provide unprecedented sensitivity when measured by ICP-MS and is especially suitable for low abundant proteins [250–252]. Lanthanides are the ideal choice for the metal tags due to the diversity and variety of isotopes with similar chemical properties and are absent in biological specimens [250,253]. Gold and silver NPs provide an alternative tagging option and are attractive due to simple synthesis and large number of atoms per tag, potentially providing higher sensitivities. However, gold is monoisotopic, and silver has two useful stable isotopes, limiting the potential for multiplex analyses.

Antibodies are Y-shaped proteins with three functional domains, the two Fab (fragment antigen binding) regions, and the Fc (fragments crystallizable) region [254]. As the two identical Fab regions bind to the target epitope on the biomolecule, most labelling protocols aim to modify the antibody on the Fc region. Efficient protocols to attach multiple lanthanide ions on the Fc region are commercially available via MAXPAR™ metal chelating polymers and antibody conjugation kits. The polymer's multiple binding sites consist of

diethylenetriaminepentaacetic acid (DTPA) [250] with capacities of more than 100 lanthanide ions per polymer [255]. During the labelling process, the antibody's disulfide bridges are partially reduced, and the exposed free thiol groups attach to the polymer with a maleimide linker molecule as depicted in Figure 4-1. The reduction reactions may introduce minor changes to the antibodies' structure, fragmentation, or loss of the antigen affinity [256]. Furthermore, the number of lanthanide ions bound to the polymer and the number of polymers attached to the antibody varies, leading to a distributed number of lanthanide ions per antibody. These variabilities may hamper the reproducibility of the immunoassay and the comparison of protein expression levels [256].

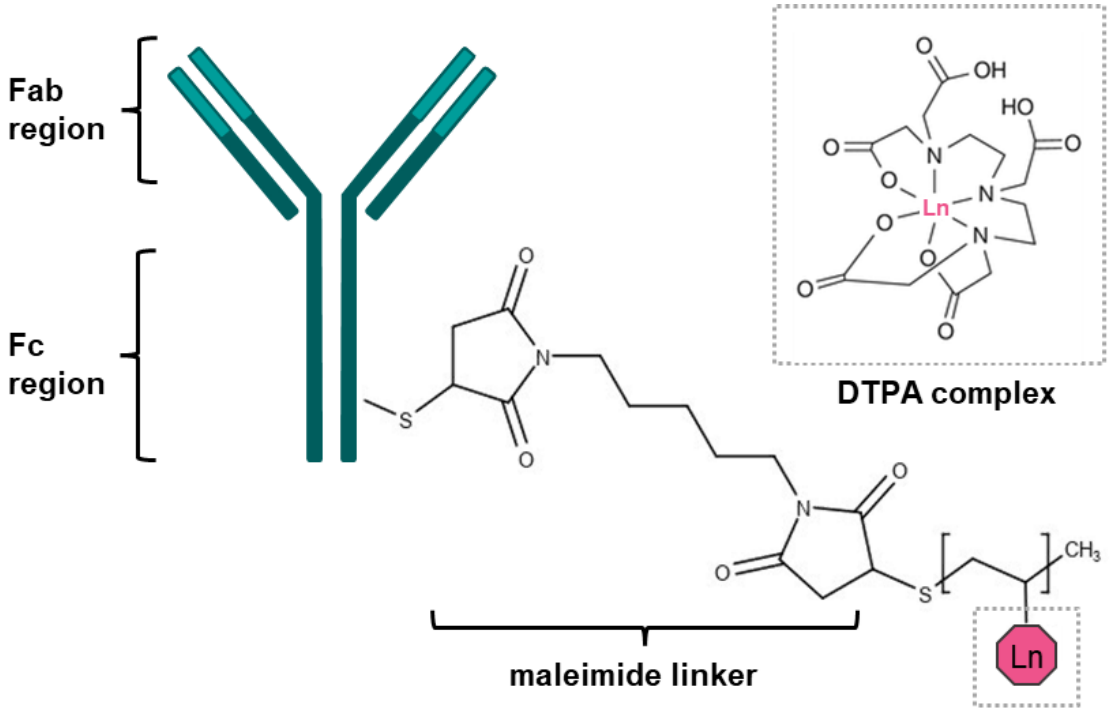

Figure 4-1: Schematic representation of a lanthanide labelled antibody. The DTPA polymer is conjugated with the antibody over a maleimide linker in the Fc region.

NP surfaces are functionalised with antibodies using two main conjugation mechanisms: adsorption or covalent binding, ideally on the Fc region of the antibody [257,258]. Ionic or physical absorption is a simple and gentle conjugation method, immobilising antibodies on NPs via hydrogen bonds, Van der Waals interactions, electrostatic forces, or hydrophobic interactions [259].

The physical stability of the conjugate is lower than covalent binding [260], rendering the latter as the preferred approach for strong molecular bonds with excellent reproducibility. Typical conjugation protocols consist of carbodiimide chemistry, maleimide linkers, or click chemistry for precise and correctly orientated antibody conjugations. However, as before, the relatively harsh reaction conditions may impact the antibodies' selectivity and/or structure [261].

Metal labelled antibodies with specific epitope affinity have excellent potential for the investigation of protein pathways in complex biological systems. Reliable quantification requires knowledge of the antibodies' integrity, degree of labelling and antibody-antigen affinity. Several suitable size exclusion chromatography (SEC)-ICP-MS methods have been proposed. Mueller *et al.* [262] investigated antibody structures after MeCAT tagging and measured sulfur and lanthanide concentrations with oxygen mass shifting. Mairinger *et al.* [263] monitored the labelling efficiency of lanthanide-DOTA complexes and determined the labelling degree using weighting factors for the lanthanide and sulfur signals. Pérez *et al.* [264] conjugated four monoclonal antibodies with different lanthanide polymer labels and determined the metal concentration via ICP-MS and the antibody content with a colorimetric assay using BSA as calibration standard. Clases *et al.* [256] used isotype dilution analysis to determine the labelling efficiency in lanthanide polymers and quantified the sulfur and lanthanide signals with mass shifting.

Despite these studies demonstrating the utility of SEC-ICP-MS for measuring antibody integrity and labelling efficiency, the technique is not ideal. The number of theoretical plates for SEC is relatively low when compared to other separation modalities, and more importantly, the method requires large injection volumes between 5-10 uL per analysis. This is a major drawback for biological standards which are limited in volume and often expensive. A promising alternative for simple and fast characterisation is CE coupled to ICP-MS. CE offers high separation efficiency over wide mass ranges and requires minimal injection volumes in the nanolitre scale. Hyphenation with an elemental selective detector

provides an opportunity for CIC making the selection of standard materials easy and accessible.

This chapter aims to assess the feasibility of applying CE-ICP-MS for the analysis metal labelled antibodies. Seven gadolinium tagged antibodies labelled with MAXPAR™ conjugation protocols were analysed and quantified via CIC. These concentrations were used to determine the labelling efficiency and number of gadolinium atoms per antibody. Subsequently, the CE-ICP-MS method was applied to the analysis of free and antibody-conjugated NPs.

4.2 Experimental section

4.2.1 Chemicals and consumables

Ultrapure water was obtained from an Arium® pro system from Sartorius Stedim Biotech (18.2 MU, Göttingen, Germany). Anti-rabbit IgG control antibody (02-6102) and anti-ZIP1 antibodies (PA5-21066) were purchased from Thermo Fisher (Waltham, MA, USA). Anti-Glial Fibrillary Acidic Protein (GFAP) antibody (ab218309) and anti-SLC30A10 (ab229954) antibodies were acquired from Abcam (Boston, MA, USA). Goat anti-rabbit IgG secondary antibody (AF008) was obtained from Novus Biologicals (Littleton, CO, USA). The antibodies were labelled with ^{156}Gd (95%) using a MAXPAR® antibody conjugation kits by Fluidigm, formerly DVS Sciences (San Francisco, CA, USA) according to the manufacturer's standard protocol (version 4 06/13). The antibody stabilizer based on phosphate buffered saline (PBS) was purchased from Candor Bioscience Gmbh (Wangen im Allgäu, Germany). An AuNP dispersion (NanoXact Nanospheres-Bare (Citrate), 99.99% purity) with a diameter of 15 ± 1.3 nm was obtained from nanoComposix (San Diego, CA, USA) in a 2 mM sodium citrate (pH 7.7) solution. An anti-rabbit IgG-AuNP conjugate with a diameter of 15 nm was purchased from Cytodiagnostics (Burlington, ON, Canada) in a 20 mM Tris (pH 8.0), 150 mM NaCl, 20% glycerol (v/v), 1% BSA solution. Both AuNP

dispersions were stored at 4 °C. The GBCA gadodiamide (Gd-DTPA-BMA, Omniscan®, 0.5 mol·L^{-1}) was acquired from GE Healthcare (Chalfont St Giles, United Kingdom). The high purity lutetium standard for ICP-MS was obtained at 10 mg·L^{-1} from Choice Analytical (Thornleigh, NSW, Australia). Sodium tetraborate decahydrate was purchased from Sigma Aldrich (Castle Hill, New South Wales, Australia). The BFS capillaries (50 µm ID, 365 µm OD; 75 µm ID, 150 µm OD; and 75 µm ID, 365 µm OD) were acquired from Polymicro Technologies (Phoenix, AZ, USA). MicroTee PEEK 1/32" and NanoTight™ Sleeves were obtained from IDEX Health & Science (Oak Harbour WA, USA). PEEK tubing was purchased from Trajan Scientific Australia Pty Ltd (Ringwood, Vic, Australia). The stainless-steel union acquired from (Agilent Technologies (Santa Clara, CA, USA).

4.2.2 Instrumentation and experimental parameters

All analyses were performed on an Agilent CE 7100 system (Agilent Technologies, Santa Clara, CA, USA) employing a 100 cm BFS capillary (Polymicro Technologies, Phoenix, AZ, USA) with 50 µM ID and 375 µM OD. The cassette temperature was 30 °C and the sample storage carousel was maintained at 20 °C. A 5 mM sodium tetraborate solution (pH 9.1) was used as BGE. For analysis, the capillary was rinsed for 3 minutes with the BGE, the samples were injected by applying -10 kV for 10 s, and the separation was performed at +30 kV producing an average current of 4 µA. Each analysis was performed in triplicate.

The CE system was hyphenated with an Agilent 8900 series ICP-MS system (Agilent Technologies, Santa Clara, CA, USA) using the in house-built CE-ICP-MS interface as discussed in Chapter 3. The make-up BGE consisting of 5 mM sodium tetraborate and 100 mg·L^{-1} lutetium was introduced at an optimised flow rate of 460 nL·min^{-1} (500 mbar) with an OB1 MK3+ system (Elveflow, Paris, France). The length of the peek tubing between make-up BGE reservoir and stainless-steel union was 22.8 cm; the BFS capillaries (75 µM ID, 375 µM OD)

connecting the stainless-steel union and the T-piece, and the nebulizer and the T-piece were 6.2 cm and 4.8 cm, respectively. A CEI-100 (Teledyne CETAC Technologies, Omaha, CE, USA) equipped with a 4.4 cm BFS capillary (75 µM ID, 150 µM OD) was used for nebulization.

The ICP-MS system was equipped with nickel cones, s-lenses, and a torch with an injector of 2.0 mm. The ICP-MS was operated in single quadrupole mode for the quantitative antibody labelling characterisation monitoring the isotopes ^{152}Gd, ^{154}Gd, ^{155}Gd, ^{156}Gd, ^{157}Gd, ^{158}Gd, ^{160}Gd, ^{175}Lu; and the NP analysis monitoring the isotopes ^{197}Au and ^{175}Lu. The sulfur analysis was conducted in MS/MS mode employing oxygen as reaction gas (ultra-high purity, BOC, North Ryde, NSW, Australia) monitoring the isotopes ^{32}S^{16}O, ^{34}S^{16}O, ^{156}Gd and ^{156}Gd^{16}O. The dwell time for all monitored isotopes was 100 ms. The applied tune parameters were the following: RF power: 1600 W; RF matching: 1.24 V; nebulizer gas flow: 1.2 L·min^{-1}.

4.2.3 Standard and sample preparation

The labelling characterisation was performed via compound-independent quantification utilising the GBCA gadodiamide. The standard solutions were diluted in ultrapure water to concentration of 0.5, 1, 5, 10, 15, 20 mg·L^{-1}. Ultrapure water used to obtain a blank value.

The antibodies were labelled with ^{156}Gd (isotope enriched) using the MAXPAR™ antibody conjugation kit according to the manufacturer's standard protocol (version 4 06/13). The labelled antibodies were diluted in PBS based antibody stabilizer and stored at 4 °C. Prior to analysis, the antibodies were diluted in ultrapure water to fit into the calibration range.

The free and antibody conjugated AuNP dispersions were diluted in 2 mM CA to maximise their stability and to avoid particle agglomeration.

4.2.4 Data analysis

Data evaluation was conducted with OriginPro (OriginLab, Version 9) and MassHunter software (Agilent Technologies). The recorded data for the antibody labelling characterisation was smoothed with a 10 data point Fast Fourier Transform (FFT) filter prior to integration. All remaining data collected in this study was visualized unprocessed unless stated otherwise.

4.3 Results and discussion

4.3.1 Isotopic abundance in natural and isotopic enriched gadolinium

MAXPAR™ antibody conjugation kits employ metal-chelating polymers that can be loaded with a variety of different lanthanide ions. They can be selected from a panel of over 40 distinct isotopically enriched tags and are marketed for routine use in mass cytometry and imaging applications. However, conventional calibration methods utilise standards with natural isotope ratios due to cost and availability. The altered isotope ratios of the MAXPAR™ reagents requires careful characterisation prior to calibration for accurate quantification. Accordingly, Figure 4-2 compares the abundance of individual gadolinium isotopes in natural gadolinium (teal) with the abundances in the MAXPAR™ isotopically enriched gadolinium (blue). The data was obtained via liquid introduction of the respective metal solutions into the ICP-MS. The most abundant isotopes in natural gadolinium were ^{158}Gd (24.0%), ^{156}Gd (22.4%), and ^{160}Gd (21.5%). The isotopically enriched gadolinium was mainly comprised of ^{156}Gd (95.0%).

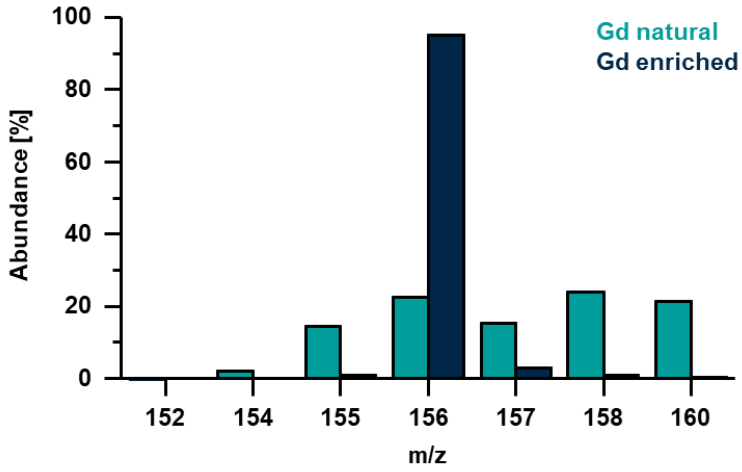

Figure 4-2: Comparison of the natural abundance and the abundance in the enriched gadolinium used in the MAXPAR™ reagents.

4.3.2 CE analysis of gadolinium-polymer labelled antibodies

Typical antibodies have a MW of 150 kDa and a pI of 6.0 (±1.0) [209]. Consideration of the CE separation guidelines from Chapter 2 indicated that the analysis should be conducted at pH values below 4.5 and a positively coated capillary, or alternatively at a pH value above 8.4 on negatively charged capillaries. The DTPA groups on the MAXPAR™ polymer eliminated the option of using a low pH range, as the metal coordinating groups on the DTPA complex become protonated leading to instability of the metal chelate. Accordingly, 5 mM sodium tetraborate was selected as the BGE for the analysis of the labelled antibodies in combination with a traditional BFS capillary.

The characterisation of metal labels per antibody requires the accurate determination of both the gadolinium and the sulfur concentration, assuming typical antibodies consist of 32 sulfur atoms [256]. While gadolinium may be analysed using standard ICP-MS modes, the detection of sulfur required a mass shift with oxygen from S^+ to SO^+. This was facilitated by operating the first quadrupole on m/z 32, adding oxygen as reaction gas to the second quadrupole, and filtering with the third quadrupole for the reaction product on m/z 48. The electropherograms depicted in Figure 4-3 were obtained with ICP-MS tunes that

maximised SO^+ formation. 90% of the sulfur was detected as SO^+ (teal) and 10% remained as S^+ (teal, dotted). The ratio of Gd^+ to GdO^+ was less biased towards one species under these conditions. About 60% of the gadolinium was detected as Gd^+ (blue), while GdO^+ was approximately 40% (blue, dotted).

Two peaks were observed in the gadolinium signal, one smaller peak at 6.8 minutes and the main signal at 7.8 minutes. The first peak likely consisted of antibody isoforms, partial antibody fragments, or loss of the loaded polymer. The SO^+ signal was detected at 7.3 minutes and did not correspond with any of the gadolinium peaks. The signal was presumably due to sulfur compounds present in the antibody stabilizer that was added in excess to the standards in the final step of the MAXPAR™ labelling protocol. This prevented accurate measurement and indicated that it was necessary to measure sulfur before the stabilizer was added to the sample. Measurement of stabilizer free conjugated antibodies was not feasible due to expense and timelines. Therefore, all antibody concentrations were assumed to remain at the manufacturer's specified concentration.

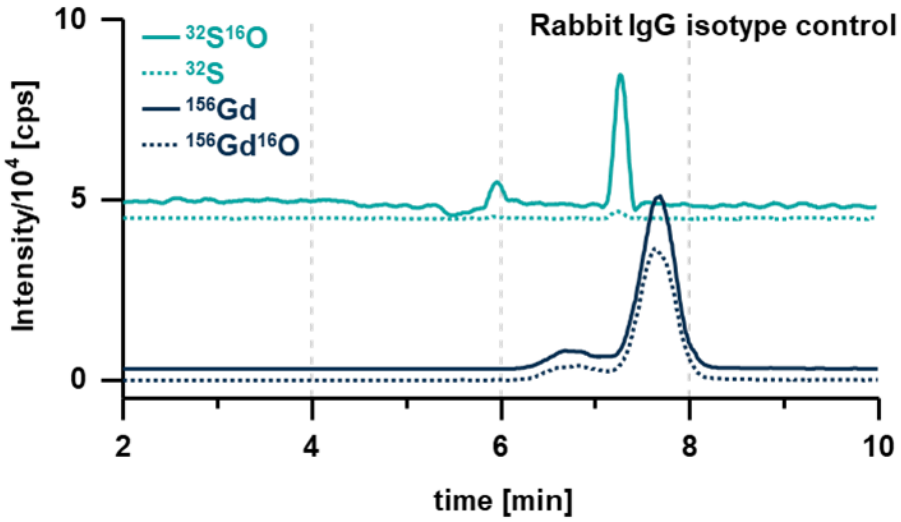

Figure 4-3: Electropherograms obtained in MS/MS mode. Adding oxygen gas induced a mass shift for S^+ to SO^+, the ratio of Gd^+ to GdO^+ was approximately 60:40 under these tune conditions. The sulfur signal did not overlap with the gadolinium signal and was caused by sulfur compounds present in the antibody stabilizer that was added to the standards.

The gadolinium concentration was determined via CIC employing gadodiamide, a GBCA used in MRI examinations. The complex's structure was similar to the lanthanide-DTPA complexes, also chelated one single central gadolinium atom, and was previously shown to be suitable as calibration standard in Chapter 3. Seven antibodies were labelled with ^{156}Gd using the manufacturer's protocol and consisted of an anti-rabbit IgG isotype control, two anti-SLC30A10 antibodies, two anti-ZIP1 antibodies, an anti-GFAP antibody, and an anti-goat secondary antibody. All analyses were quantified in standard mode CE-ICP-MS. The electropherograms for each antibody are shown in Figure 4-4 and show significant differences in their peak areas indicating variations in the number of metal labels per antibody.

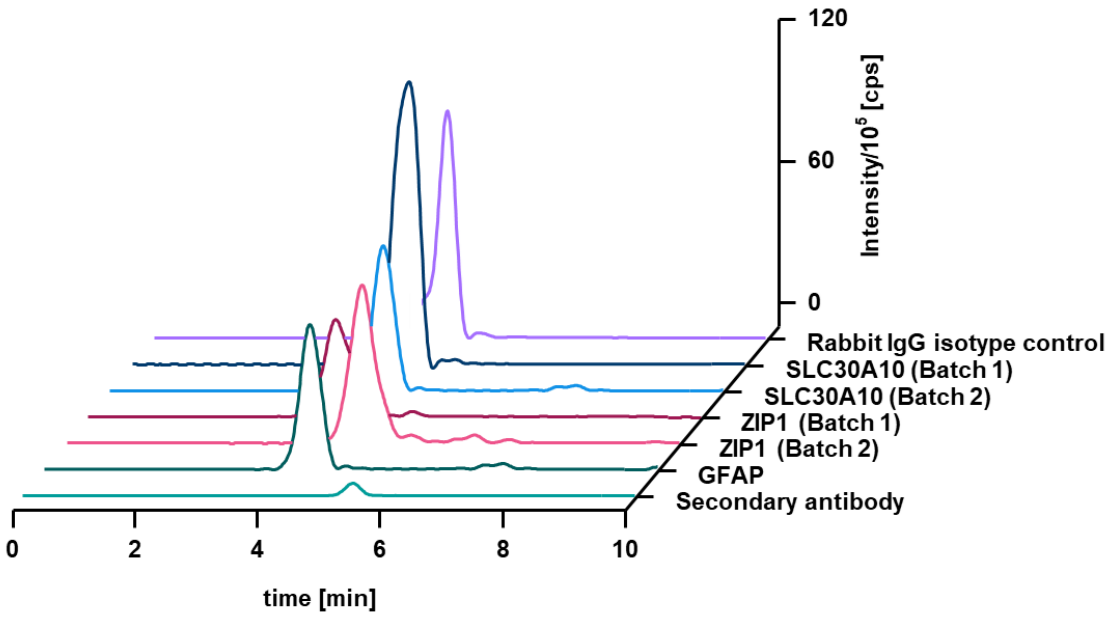

Figure 4-4: CE analysis of seven gadolinium labelled antibodies.

The number of lanthanide ions per antibody was calculated by recording the gadolinium and antibody concentrations in µmol·mL^{-1} and assuming the antibody remained at the original manufacturer's reported concentration, as would be expected after executing an ideal labelling procedure. For example, consider the anti-rabbit IgG isotype control at 1 mg·mL^{-1} (0.0066 µmol·mL^{-1}). After conjugation with enriched ^{156}Gd and a 2-times dilution after addition of the stabilizer, the

gadolinium concentration was measured at 0.54 µmol·mL^{-1}, whilst the antibody was 0.0033 µmol·mL^{-1}. This molar ratio represented an average number of 161 gadolinium atoms per anti-rabbit IgG isotype control. The same process was applied to the remaining six antibodies and are summarised in Figure 4-5.

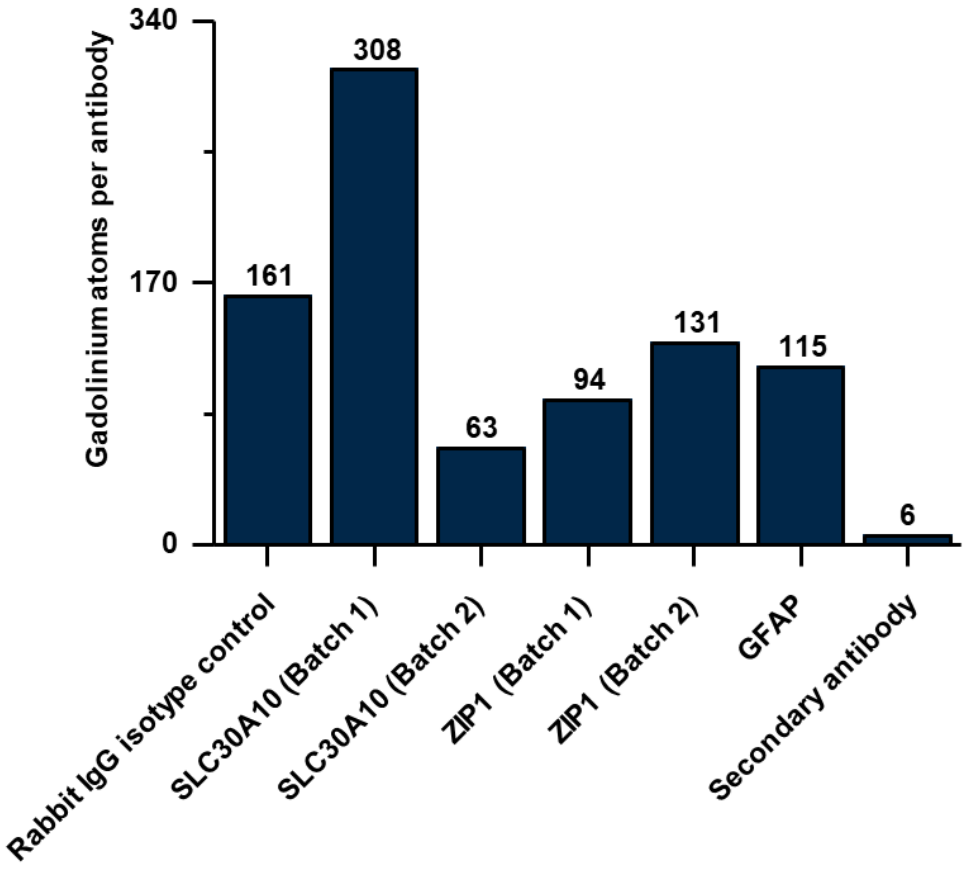

Figure 4-5: Overview of the determined number of gadolinium atoms per antibody.

The number of gadolinium labels per antibody ranged between 6 and 308. While the extreme values seem less realistic, the remaining values are comparable with the results of other groups, which obtained 60 to 157 metals per polymer chain in similar labelling strategies [255]. The metal to antibody ratio varied not only between different antibodies, but also between antibodies of the same kind. This was due to a range of factors influencing the labelling efficiency during the tagging procedure, such as the progress of the reduction step, incomplete tagging, or antibody loss during ultrafiltration. This variation underlines the importance of

antibody characterisations and highlights the necessity for simple characterisation methods, which are ideally performed prior to the antibodies' deployment in mass cytometry and imaging applications. The variations shown above would be expected in routine preparations of tagged antibodies and has important implications for all publications that have reported quantified spatial distributions of protein biomarkers without quality control checks of the labelling protocol.

4.3.3 CE analysis of nanoparticle conjugated antibodies

The suitability of the CE-ICP-MS method for measuring and characterising conjugated NPs was assessed by separation of a 15 nm dispersion of free and conjugated AuNPs. Figure 4-6 depicts the raw electropherograms obtained from a dispersion of un-conjugated AuNPs (blue) and secondary antibody conjugated AuNPs (teal). The electropherograms consisted of two signals, a wide main peak which was produced from the distribution of NP sizes in the dispersion, and a sharp signal after the main peak. The second signal may be caused by complexes of small gold colloids with citrate, since both AuNP dispersions were diluted in 2 mM CA for stabilization purposes [265].

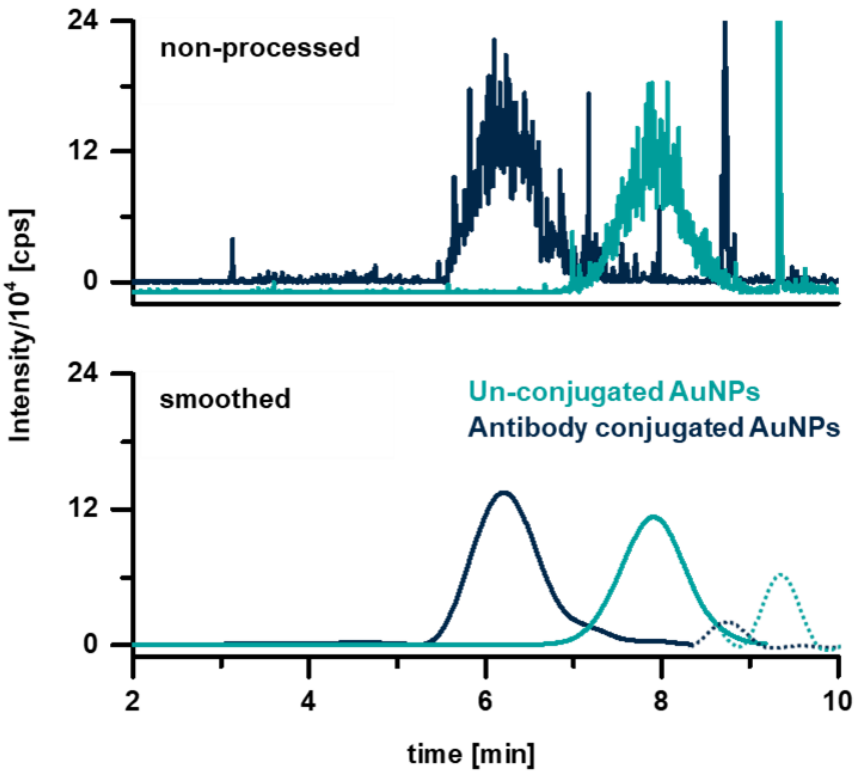

Figure 4-6: Electropherograms for a free 15 nm AuNP dispersion (blue) and a secondary antibody conjugated 15 nm AuNP dispersion (teal). Compared is the non-processed signal (**top**) with the signal obtained after smoothing with a 40-point FFT filter (**bottom**).

The conjugation of antibodies to the surface of NPs induced a shift in the NPs migration time, due to altered surface chemistry and charge-to-mass ratio. The un-conjugated NPs comprised of a citrate surface that carried more negative charge than NPs with an antibody corona. This resulted in a stronger migration opposite to that of the EOF and later registration at the detector. The increase in migration was also due to the smaller size of the un-conjugated nanoparticle.

Figure 4-6 also highlights the influence of signal processing. FFT filters are very effective at smoothing the electropherogram and representing particle distributions, however, caution must be applied when interpreting the second, sharp signal (dotted line). Here, the processed peaks have broadened significantly which erroneously suggest a wide distribution, in contrast, the raw electropherogram clearly indicates a narrow distribution. FFT filters are

smoothing functions used in electrophoresis or chromatography to improve peak resolution and signal-to-noise rations. The function uses Fourier transformation to analyse the frequency components in the signal, increases or decreases specific frequencies, and then re-constructs the signal.[266,267] The filter cut-offs were optimized for the main signal and were not suitable for the sharp signal.

4.4 Conclusion

In this chapter, the feasibility of applying CE-ICP-MS for the determination of labelling efficiencies of metal conjugated antibodies was evaluated.

Seven antibodies were labelled with isotopically enriched gadolinium following MAXPAR™ conjugation protocols. The metal polymer tagged antibodies were analysed via CE-ICP-MS and the gadolinium concentration in the diluted antibody solutions were determined via CIC. The number of gadolinium atoms per antibody varied between 6 and 308 for different antibodies and antibodies of the same kind, underlining the importance of reliable characterisation methods.

The CE-ICP-MS method was also applied to the analysis of nanoparticle-antibody conjugates and was suitable to distinguish 15 nm dispersions of un-labelled AuNPs and secondary antibody conjugated AuNPs. The altered surface chemistry and size of the NPs produced a shift in the NPs migration time, making the technique an interesting tool for quality control purposes.

The method shows promise for both the characterisation of lanthanide labelled antibodies, and NP conjugated antibodies, however, some further developments are required. Future work should focus on the optimization of the separation of individual antibody fragments, establishing antibody-antigen affinities, and the accurate determination of sulfur concentrations in MAXPAR™ labelled samples without added stabilizer and in antibody-NP conjugates.

Chapter

Characterisation of Nanoparticles by SP ICP-MS

Based on:

Sarah Meyer, Raquel Gonzalez de Vega, Xiaoxue Xu, Ziqing Du, Philip A. Doble, and David Clases, *Characterisation of Upconversion Nanoparticles by Single-Particle ICP-MS Employing a Quadrupole Mass Filter with Increased Bandpass*, Anal. Chem. (**2020**), 92, 22, 15007–15016

5.1 Introduction

NPs and particularly upconversion nanoparticles (UCNPs) have unique optical, electronic, and magnetic properties, which can be exploited for multimodal imaging. The labelling and application of UCNPs however requires an accurate measurement of the particle size, number concentrations, and particle-particle interactions. This chapter addresses Aim 4, the characterisation of NPs by SP ICP-MS; and sets the basis for integration of NPs and specifically UNCPs into the imaging workflow.

Nanomaterials comprise a large group of compounds containing structures on a scale between 1 and 100 nm and exhibiting properties that are quite different from their (non-nanostructured) bulk counterparts. They are attracting increasing interest as they can be exploited and customised for various chemical, biological, or physical applications. NPs are useful for medicine, numerous research disciplines, and industrial applications such as therapeutic agents, drug delivery vehicles, chemical sensors and probes, personal care products, catalysts, coatings, and paints [268–271]. Their manufacturing and application rely on methods to accurately and precisely characterise elemental compositions, size distributions, and stabilities [272,273].

Lanthanide-doped UCNPs have unique optical, electronic, and magnetic characteristics. The doped lanthanide ions in the host crystal allow electronic transitions, which can be harnessed for photon upconversion by consecutive absorption of low-energy photons. This can be exploited for high-resolution microscopy, biosensing, solar energy harvesting, deep-tissue optical bioimaging, and multimodal diagnostics [273–277]. The optical properties of UCNPs are tuneable and depend on the selection, combination, and amount of doped lanthanide ions, the stoichiometry, host structure, density, and size [278]. The understanding, control, and prediction of properties of UCNPs require versatile and dedicated analytical methods [279–282]. For example, it is essential to accurately measure the number and size of dispersed UCNPs to ensure efficient surface modifications for conjugation when using biomolecules with different

moieties, such as antibodies, ssDNA, or miRNA [283]. Furthermore, the dispersion and chemical stability must be considered for practical clinical applications.

ICP-MS emerged almost four decades ago and is a multifaceted technique for elemental analyses over a vast linear dynamic range [234]. In combination with secondary instrumentation like liquid chromatography and laser ablation it is possible to perform speciation analysis and EBI of various metal species, including NPs [91,103,284–287]. The progressive instrumental advancements for rapid detection and improved processing algorithms have opened new strategies for the detection and characterisation of individual NPs [170–173]. The principle of this SP ICP-MS relies on the individual detection of NPs in dilute dispersions. At low particle concentrations, NPs are individually transported into the ICP, where they are atomised. Subsequently, atoms are ionised, and the resulting ion cloud is extracted into the mass spectrometer to produce discrete signals when focused onto the detector [288]. Several thousand particles may be individually sampled per minute to calculate the particle number concentration and to construct models of size distributions and particle−particle interactions [176,288,289]. Ion transmission is relatively low in ICP-MS, which limits the observable size of NPs. After atomization, ionization, ion extraction, ion transport, and mass filtering, only a small fraction of isotopes per NP reaches the detector [290]. For particles with dimensions at the size detection limit (sDL), signals are within the standard deviation of the background signal, which is generated by ionic species of the targeted analyte and electronic noise. This limits the applicability of SP ICP-MS for the measurement of small diameter or low-mass-fraction particles [291,292].

Despite its excellent potential for NP characterisation [177], SP ICP-MS has not yet been applied to the investigation of UCNP dispersions. This is most likely related to small particle sizes and low concentrations of doped lanthanides requiring low sDL, which are often beyond the capability of conventional SP ICP-MS. Methods improving ion transmission to increase signal-to-noise ratios in ICP-

MS have the potential to overcome these limitations [290,291]. Different strategies to alter ion extraction, ion transport, and mass filtering may be applied to increase ion transmission and to improve the sDL in order to bring small UCNPs within the reach of SP ICP-MS. Tuoriniemi *et al.* employed sector-field-based ICP-MS that increased ion transmission by operating hard extraction conditions. The authors also suggested using a jet interface to further improve transmission [290]. Similarly, Fréchette-Viens *et al.* showed recently that the sDL of zinc NPs can be increased by operating sector-field-based ICP-MS [293]. Another option to improve ion transmission is the manipulation of the mass bandwidth of the quadrupole. Balcaen *et al.* employed ICP-MS/MS where the first quadrupole was operated with a large mass bandpass to allow the simultaneous transmission of S^+ and SO^+, whereas the third quadrupole was operated with a unit mass resolution [158]. A similar strategy was followed to improve the signal-to-noise ratios of endogenous elements in LA-ICP-MS/MS [65]. Recently, we employed (single quadrupole) LA-ICP-MS and altered the mass bandwidth to increase signal-to-noise ratios for the analysis of metal-labelled antibodies by a factor of 6.86 relative to the standard method [168].

This chapter details the development and application of a new method to enhance ion transmission and to decrease the sDLs for UCNPs. As proof of concept, dispersions of small AuNPs (10.9 nm) were initially investigated to demonstrate how ion extraction and transport may be altered for the detection of small NPs. We further manipulated the mass bandpass in ICP-MS to increase the transmission of a quadrupole mass filter while decreasing mass resolution. These approaches were combined to determine size distributions, stoichiometries, and particle−particle interactions of lanthanide-doped UCNPs.

5.2 Experimental section

5.2.1 Chemicals and consumables

Ultrapure water was obtained from an Arium® Pro system (Sartorius Stedim Plastics GmbH, Germany). The daily performance of the ICP-MS instrument was monitored using a tuning solution containing 1 $\mu g \cdot L^{-1}$ Li, Y, Tl, Ce, and Ba. The detector deadtime was determined by analysing diluted Er standards from high-purity standards (Charleston, SC, USA). AuNP dispersions (NanoXact Nanospheres-Bare (Citrate), 99.99% purity) with diameters of 4.4 ± 0.5, 10.9 ± 1.0, and 15.0 ± 1.3 nm were purchased from nanoComposix (San Diego, CA, USA) in a 2 mM sodium citrate solution and stored at 4 °C. Mass concentrations were determined by the supplier using ICP-MS (Thermo Fisher XSeries 2). The diameter and size statistics were undertaken using ICP-MS JEOL 1010 transmission electron microscope and a Malvern Zetasizer Nano ZS. Upon analysis, stock solutions were sonicated and diluted in containers made of polypropylene for SP ICP-MS. For the acquisition of mass spectra and elemental responses, certified Au, Y, Yb, Er, and Gd standard solutions for ICP-MS were obtained at 10 $\mu g \cdot mL^{-1}$ in 2% HNO_3 from high-purity standards and diluted to 1 $ng \cdot mL^{-1}$ for analysis.

Three types of UCNPs were manufactured in-house using yttrium chloride hexahydrate ($YCl_3 \cdot 6H_2O$, 99.99%), ytterbium chloride hexahydrate ($YbCl_3 \cdot 6H_2O$, 99.998%), erbium chloride hexahydrate ($ErCl_3 \cdot 6H2O$, 99.9%), gadolinium chloride hexahydrate ($GdCl_3 \cdot 6H_2O$, 99%) sodium hydroxide (NaOH, 98%), ammonium fluoride (NH_4F, 99.99%), oleic acid (OA, 90%), 1-octadecene (ODE, 90%), and hydrochloric acid (HCl, 37%). All reagents were purchased from Sigma-Aldrich and used as received without further purification.

5.2.2 UCNP synthesis and characterisation

Synthesis of NaYF4 host UCNPs

The typical synthesis procedure for the $NaYF_4$ host UCNPs doped with lanthanide ions of Yb and Er consisted of the following steps [294]: YCl_3, $YbCl_3$ and $ErCl_3$ (in total 1 mM) were dissolved in methanol base at a molar ratio of 78:20:2 (type I) or 79:20:1 (type II). Under a high purity argon flow, this solution was mixed with 6 ml oleic acid and 15 ml octadecene. In order to remove methanol and water, the mixture was heated to 150 °C for 30 minutes. After cooling to room temperature, 4 mM sodium hydroxide (NaOH) and 2.5 mM ammonium fluoride (NH_4F) in methanol were added and stirred for another 30 minutes at room temperature. The mixture was then heated at 90 °C for 20 minutes and at 150 °C for further 10 minutes to evaporate the methanol and water. The reaction solution was then heated to 300 °C for 90 minutes. Controlling the heating rate from 150 °C to 300 °C of the reaction mixture determined the size of the NPs [295]. A rate of 8.33 $°C \cdot min^{-1}$ produced 20 nm UCNPs and a rate of 25 $°C \cdot min^{-1}$ produced 90 nm UCNPs. The NPs were then washed using a mixture of oleic acid, cyclohexane, methanol and ethanol after the reaction solution was cooled to room temperature. Samples were dispersed in cyclohexane for Transmission Electron Microscopy (TEM) characterisation and stored at -20°C until further use. 0.1 M HCl solution was used to wash off the oleic acid from the UCNPs surface to disperse them in ultrapure water for ICP-MS characterisation. To avoid dissolution of UCNPs, analyses were performed directly after dispersion and dilution and samples were constantly cooled on ice. Additionally, the integrity and size of UCNP was confirmed performing TEM after their dispersion in water.

Synthesis of NaGdF4 host UCNPs

The procedure for the NaGdF4 host UCNPs doped with Yb and Er followed the protocol by Wang *et al*. [296]: $Gd(CH_3COO)_3$, $Er(CH_3COO)_3$ and $Yb(CH_3COO)_3$ (in total 1 mmol) were dissolved in ultrapure water at a molar ratio of 78:20:2 and

sonicated. Under a high purity argon flow, the lanthanide acetate solution was mixed with 4 ml of oleic acid and 6 mL of 1-octadecene. The mixture was heated to 150 °C for 30 minutes to remove water. After cooling to room temperature, 4 mmol NaOH and 3.3 mmol NH_4F in methanol solution was injected into the reaction solution and stirred for another 30 minutes. The mixture was heated at 50 °C for 30 minutes and then heated to 100 °C for further 10 minutes to evaporate the water and methanol. The reaction solution was then heated to 280 °C for 90 minutes. The washing process, storage, dispersion in water and characterisation were the same as for $NaYF_4$ UCNPs.

UCNPs characterisation

Transmission electron microscopy (TEM) images of all three types of UCNPs were recorded with an FEI Tecnai T20 transmission electron microscope and are shown in Figure 5-1 A. The dimensions and numbers of the NPs were determined, counted, and graphed with ImageJ 1.50I software. Crystal phase analysis of NPs was performed using a Bruker D8 Discover A25 X-ray diffractometer with Cu Kα1 radiation (40 kV, 40 mA, λ = 0.15406 nm). The results were compared against the PDF-4 + 2019 RDB database to identify the crystal phase and structure (Figure 5-1 B). In these cases, all UCNPs crystallised hexagonally, which allowed the calculation of UCNP densities according to Mackenzie *et al*. [297].

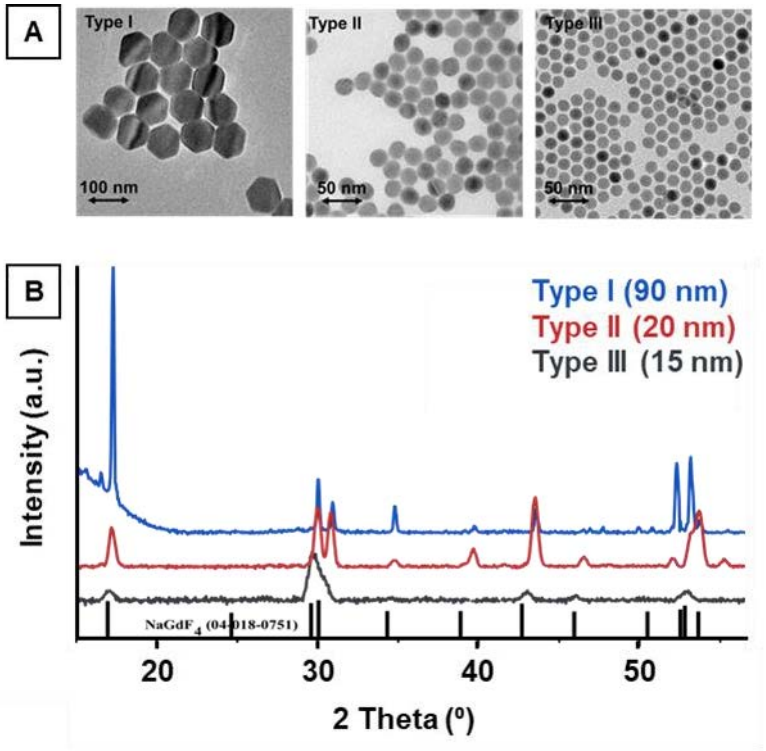

Figure 5-1: TEM (**A**) and XRD (**B**) characterisation of the synthesised UCNPs. Type I consisted of a 90 nm NaYF4 host structure which was doped with 20%Yb and 2% Er. Type II consists of a 20 nm NaYF4 host structure which was doped with 20%Yb and 1% Er. Type III consists of a 15 nm NaGdF4 host structure which was doped with 20%Yb and 2% Er. All UCNPs crystallised hexagonally.

5.2.3 SP ICP-MS analysis and experimental parameters

For SP ICP-MS, an 8900 series ICP-MS/MS system (Agilent Technologies) was equipped with Pt cones and s-lenses. The torch accommodated an injector with a diameter of 1.5 mm. Aerosols were generated via self-aspiration employing a concentric nebulizer and a Scott double-pass spray chamber cooled to 2 °C. The ICP-MS/MS instrument was operated in SQ mode, and the dwell time of the quadrupole was set to 100 µs. Elements were monitored consecutively with an acquisition time of 90 s, and data analysis was performed using MassHunter software (Agilent Technologies) and OriginPro (OriginLab, Version 9). The RF power was set to 1.6 kW, the sample depth (z-position) was set to 8.0 mm, and the nebulizer gas flow was tuned daily between 1.04 and 1.08 $L \cdot min^{-1}$. The oxide ratio ($^{157}Gd^{16}O^{+}/^{157}Gd^{+}$) was below 1.8%. The gradual optimization to enhance

transmission required modification of the ion optics and the quadrupole mass filter. Parameters for each acquisition mode are given in Table 5-1.

Table 5-1: Experimental Parameters. The standard method featured soft extraction parameters. Based on this method, ion extraction and transport were optimised for Yb, Au, and lanthanides (optimised ion lenses). Finally, a bandpass mode employing the quadrupole with increased mass bandpass was developed and applied to the analysis of Gd, Er, Y, and Au.

	Standard method [V]	**Optimised ion optics [V]**	**Bandpass mode [V]**
Extract 1	4.0	-200.0	-200.0
Extract 2	-230	-6.0	-6.0
Omega Bias	-150	-190	-200
Omega Lens	10.0	11.0	13.0
Q1 Entrance	-5.0	-5.0	-7.0
Q1 Exit	0.0	0.0	-1.0
Cell Focus	0.0	-14.0	-17.0
Cell Entrance	-50	-80	-80
Cell Exit	-50	-80	-90
Deflect	13	14	20
Plate Bias	-50	-50	-50
Q1 Bias	-5.0	-10.0	-20.0
Q1 Prefilter Bias	-10.0	-27.0	-27.0
Q1 Postfilter Bias	-10.0	-23.0	-23.0
OctP Bias	-8.0	-12.0	-13.0
ED	5.0	3.0	0.5
Q2 Bias	-3.0	-9.0	-12.5

Except for the bandpass mode, all masses were monitored at unit resolution with peak widths of 0.7 amu at 10% peak height, and Q1 was operated with a scanning line gain factor of 0.9. In the bandpass mode, the mass resolution was decreased for both quadrupoles to increase ion transmission.

5.2.4 Data analysis

The elemental responses and mass spectra were obtained by analysing ionic 1 $\mu g \cdot L^{-1}$ standards for ICP-MS. Ultrapure water was analysed as a blank, and the background intensity was subtracted. The rapid acquisition of the quadrupole provided four data points on average per individual NP, and the resulting peaks were integrated and depicted in a histogram. For the size calibration of AuNPs, particle diameters were calculated on the basis of a previously analysed 15 ± 1.3 nm AuNP dispersion as a custom reference material using MassHunter software. Au particle dispersions were characterised by the supplier regarding mass concentration, particle number concentration, and size distribution. For UCNPs, particle masses (m_p) and diameters (D_p) were calculated following equations 5.1 to 5.3 using MassHunter software. The sDL was calculated according to Lee *et al*. as shown in equation 5.4 [298]

$$\eta = \frac{N_m}{N_{th}} \tag{5.1}$$

$$m_p = \frac{I_p \, t_d \, m \, \eta \, f}{s} \tag{5.2}$$

$$D_p = \sqrt[3]{\frac{6 \, m_p}{\pi \, \rho_p}} \tag{5.3}$$

$$sDL = \sqrt[3]{\frac{6 \cdot 3 \, \sigma_{DI}}{\pi \, \rho_p \, f \, R}} \tag{5.4}$$

where η is the transport efficiency as the ratio of measured particles N_m to the theoretical number of particles N_{th} in a sampled volume. The transport efficiency

was determined to be 5.5%, and the value was confirmed by determining η via particle sizes [299]. I_p is the measured particle signal (integrated area), t_d is the dwell time (100 µs), V is the sample inlet flow (350 µL·min^{-1}), f is the molar mass fraction, s is the response factor of a 1 ng·mL^{-1} ionic standard, ρ_p is the particle density, and R is the mass-related response factor of a nanoparticle [298]. σ_{DI} is the standard deviation of a blank and was calculated from 225 000 integrations with integration intervals corresponding to the average NP signal duration (400 µs). To improve the comparison of histograms, signal distributions were fitted using a log-normal distribution model. A Poisson distribution model was used to estimate the number of events where two or more particles were detected simultaneously.

5.3 Results and discussion

5.3.1 Maximising ion transmission

Due to relatively low ion transmission in ICP-MS, only a small fraction of ionised masses generated within the ICP reaches the detector. This limits the observable size of individual NPs in the single-particle mode as the corresponding signals become indistinguishable from the background noise. Ion transmission may be improved by consideration of two aspects: optimization of ion lenses' parameters to improve ion extraction and transport and manipulation of quadrupole mass filtering. The former has been investigated in various studies and is accomplished by employing hard extraction conditions, which are applied in sector-field-based ICP-MS setups [290] but also in combination with cool and dry plasmas in quadrupole-based GC-ICP-MS [300] and LA-ICP-MS [168]. During hard extraction, the polarity of the first extraction lens is reversed to highly negative potentials (e.g., −200 V, Table 5-1), whereas the second extraction lens is operated closer to the ground potential (e.g., −6 V, Table 5-1) to increase the kinetic energy of ions [301]. This results in a more efficient ion extraction and transport, which simultaneously mitigates space charge effects. However,

increasing the kinetic energy of the extracted ions requires consideration of the potentials applied to the following ion lenses (e.g., omega lenses) to ensure maximum transmission. Table 5-1 lists the instrumental parameters of the standard method as well as a hard extraction method with modified ion lenses.

As discussed in Chapter 1.4.1, the transmission in quadrupole MS can further be manipulated and increased at the expense of selectivity [168]. A quadrupole analyser is operated with a set of RF and DC voltages that stipulate stable trajectories for specific m/z. The two-dimensional (x, y) motion of ions through the quadrupole can be described by the Mathieu equations and depends on the RF and DC voltages applied to the four metallic rods. The Mathieu equations are second-order differential equations and can be solved numerically. The graphical description is a popular way to describe the solution of these equations and is shown for m/z 197 in Figure 5-2 A and for the isotopes of Yb in Figure 5-2 C. Each m/z has a triangular-like stability region in which any DC and RF combination assigns a stable trajectory through the quadrupole. It is worth noting that all stability diagrams have a common overlap in the low-mass region. As such, selecting a combination of DC and RF in the overlap region allows the transmission of several m/z simultaneously. To maintain unit mass resolution (typically with a peak width of 0.7 amu at 10% peak height), quadrupoles operate RF/DC combinations that are located on a scan line truncating the stability diagrams in regions without overlap, as shown in Figure 5-2 C (purple line). The position of the line determines the mass resolution and ion transmission, which correlate inversely. Increasing the y intercept while maintaining the slope increases mass resolution but decreases ion transmission and vice versa. Changing the y intercept and the slope simultaneously allows manipulation of the mass bandpass for the selected mass ranges and increases ion transmission (compare magenta scan lines in Figure 5-2 A,C) [168]. This analysis mode is further referred to as the “bandpass mode”. In this study, the gain of the slope of the scan line was modified to transmit a mass range with a bandwidth between 8 and 9 amu.

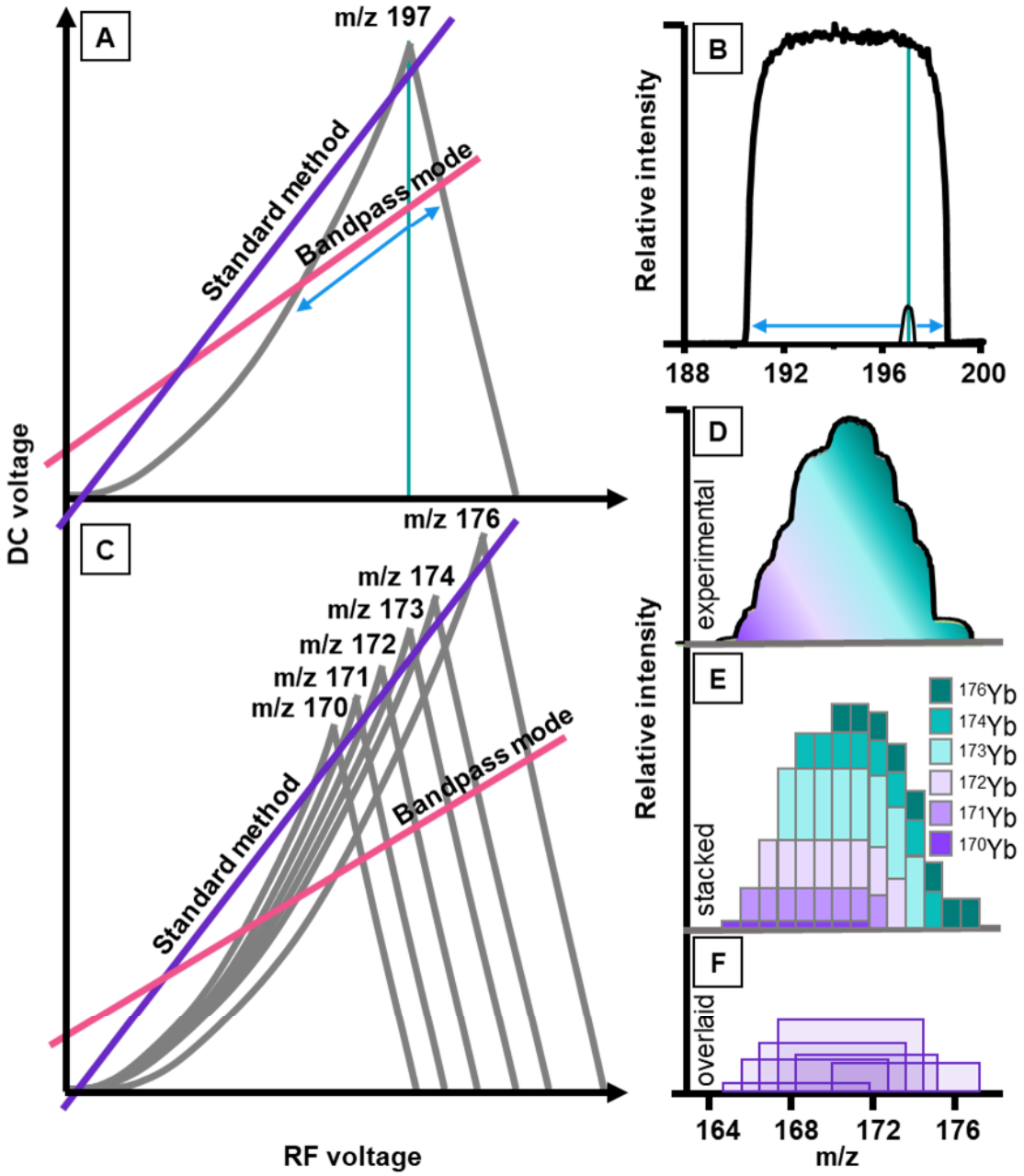

Figure 5-2: (**A**) Schematic stability diagram for m/z 197. The scan lines for standard operation (unit mass resolution) and for the bandpass mode are marked. (**B**) Mass spectrum of Au using a standard scan line and the bandpass mode. (**C**) Stability diagrams for all relevant Yb isotopes. Operating the bandpass mode results in a signal convolution. (**D**) Yb mass spectrum recorded in the bandpass mode. (**E, F**) Simulated convolution of Yb isotope signals.

Analysing a monoisotopic element like Au (^{197}Au) in bandpass mode had several observable effects, as shown in Figure 5-2 B. As the mass bandpass increased

to between 8 and 9 amu, the sensitivity at 197 amu increased due to improved ion transmission. In addition, the bandwidth expanded further toward lower masses than higher masses when increasing the ion transmission (see arrows in Figure 5-2 A,B). This asymmetry is a direct consequence of the nonsymmetrical Mathieu stability diagram (compare Figure 5-2 A, dark blue arrows and teal coloured line) [302].

Analysing an element with several isotopes has additional effects when the bandpass is as large as 8 amu. Due to the increasing mass peak widths, isotopic signals start to overlap and convolute. Figure 5-2 C shows a schematic stability diagram of all Yb isotopes with relevant abundances. Performing a standard quadrupole scan (purple line Figure 5-2 C) resolved each isotope. However, operating the bandpass mode (magenta line, Figure 5-2 C) resulted, on the one hand, in an increased transmission of individual isotopes, as previously shown for ^{197}Au, and, on the other hand, in the convolution of isotopic signals, which increased the sensitivity further. Figure 5-2 D shows the experimental mass spectrum of Yb in the bandpass mode, and Figure 5-2 E,F shows a simulation of how the different isotopes of Yb form one convoluted signal. Due to the asymmetry of the stability zone and mass peaks, signal convolution was also asymmetric and was more pronounced on the low-mass side. The effect of signal convolution was pronounced for elements with several evenly abundant isotopes like Gd, Er, and Yb.

Figure 5-3 shows the mass spectra of Gd, Er, Yb, and Au operating standard parameters and compares sensitivities as a measure of ion transmission and mass resolution against a method with increased ion extraction and operating the quadrupole in the bandpass mode.

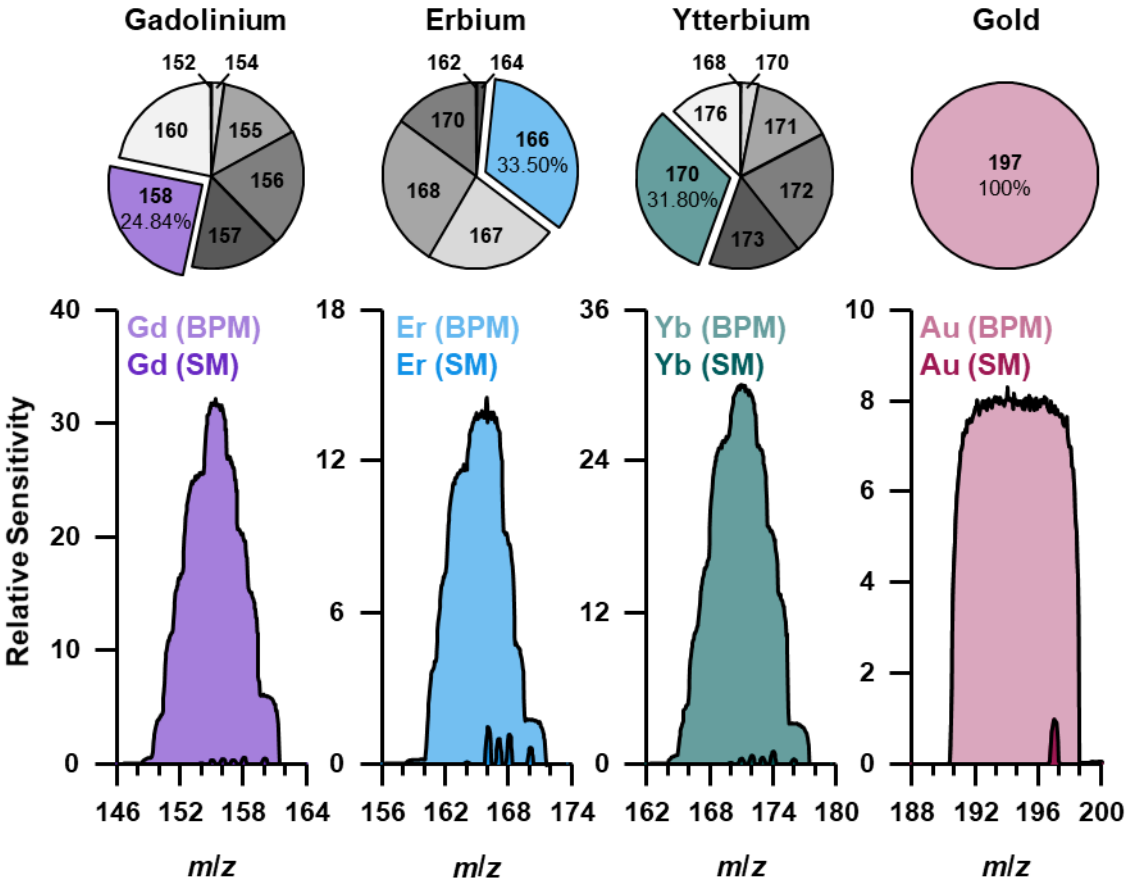

Figure 5-3: Gd, Er, Yb, and Au were analysed in the standard mode (SM) and bandpass mode (BPM) to compare mass resolution and sensitivity. Ion transmission in the bandpass mode was increased by two mechanisms: First, the quadrupole transmission of individual isotopes was enhanced, exemplified by the monoisotopic Au. Second, the transmission was further increased by the simultaneous acquisition of several isotopes as shown for Gd, Er, and Yb.

The sensitivity of the monoisotopic Au (^{197}Au) increased 8.4-fold relative to the standard method. Gd, Er, and Yb are lanthanides that have a broad isotope distribution, as shown in Figure 5-3 (top). In standard quadrupole mass filtering, only one isotope at a time and therefore only a fraction of the total ions of these elements are transmitted per dwell time, which limits the sensitivity. In contrast, operating the quadrupole with a larger mass bandwidth increased the sensitivity due to convoluted isotope signals. The highest intensities were obtained at 155 amu for Gd, 165 amu for Er, and 171 amu for Yb. However, due to spectral overlap of isotopes from Yb and Er, 172 amu and 163 amu were monitored to

determine the relative improvement in the sensitivity and later for SP ICP-MS. The bandpass mode increased sensitivities 33-, 12-, and 28-fold for Gd, Er, and Yb relative to the standard method that monitored the most abundant isotopes of these elements. Table 5-2 shows the factors of improvements after optimising ion extraction and transport and operating the bandpass mode.

Table 5-2: Relative Sensitivities Obtained for Y, Gd, Er, Yb,and Au. For the standard method and optimised ion optics method, the most abundant lanthanide isotopes (^{158}Gd, ^{166}Er, and ^{174}Yb) were monitored. For the bandpass mode, higher sensitivities were achieved monitoring Gd at 155 amu, Er at 163 amu, and Yb at 172 amu. All methods monitored ^{197}Au and ^{89}Y. Values are relative to the standard method for SP ICP-MS.

Element	**Optimised ion optics (sensitivity relative to the standard method)**	**Bandpass mode (sensitivity relative to the standard method)**
Y	4.2	
Gd	2.0	33
Er	1.4	12
Yb	2.4	28
Au	3.0	8.4

The bandpass mode demonstrated the potential to improve figures of merits for elements with several isotopes unlikely to be confounded by spectral interferences. Gd, Er, and Yb are critical elements for the photon upconversion in UCNPs and are incorporated into the $NaYF_4$ host structure by replacing Y^{3+}. UCNPs can also be analysed by targeting Y. While confounding interferences for Gd, Er and Yb are rather unlikely, they become more relevant for the monoisotopic ^{89}Y is a 4d element for which interferences become more relevant. Depending on the matrix and the plasma conditions, decreasing mass resolution can result in adverse figures of merit if targeted masses are close to the mass range of ubiquitous elements (e.g., Sr) and prominent spectral interferences (e.g., Ar^{2+}). Therefore, the bandpass mode was only applied to the analysis of Gd, Er,

Yb, and Au, while Y was analysed with optimised extraction and transport conditions increasing the sensitivity by a factor of 4.2 (Table 5-2).

5.3.2 Analysis of AuNPs

Stable dispersions of AuNPs are frequently investigated in various matrices and are an excellent model system for method development and subsequent comparison. The detection of Au in ICP-MS is hampered by its high first ionization potential, which leads to a low ion population within the plasma and restricts the sDL for single-particle detection. To differentiate a NP signal with reasonable certainty from the noise and ionic background signals, NP signals must be significantly higher (>3-times) than the standard deviation of the background signal. Typically, NP dispersions are not monodisperse but have characteristic size distributions, where fit functions were often used to describe and compare the distributions and maxima. Signal distributions that are interfered by background signals can only be partially fitted or require extrapolation.

Figure 5-4 A1 shows the signal distribution following the analysis of a 10.9 nm (±1 nm) AuNP dispersion employing a standard method (compare Table 5-1 for instrumental parameters).

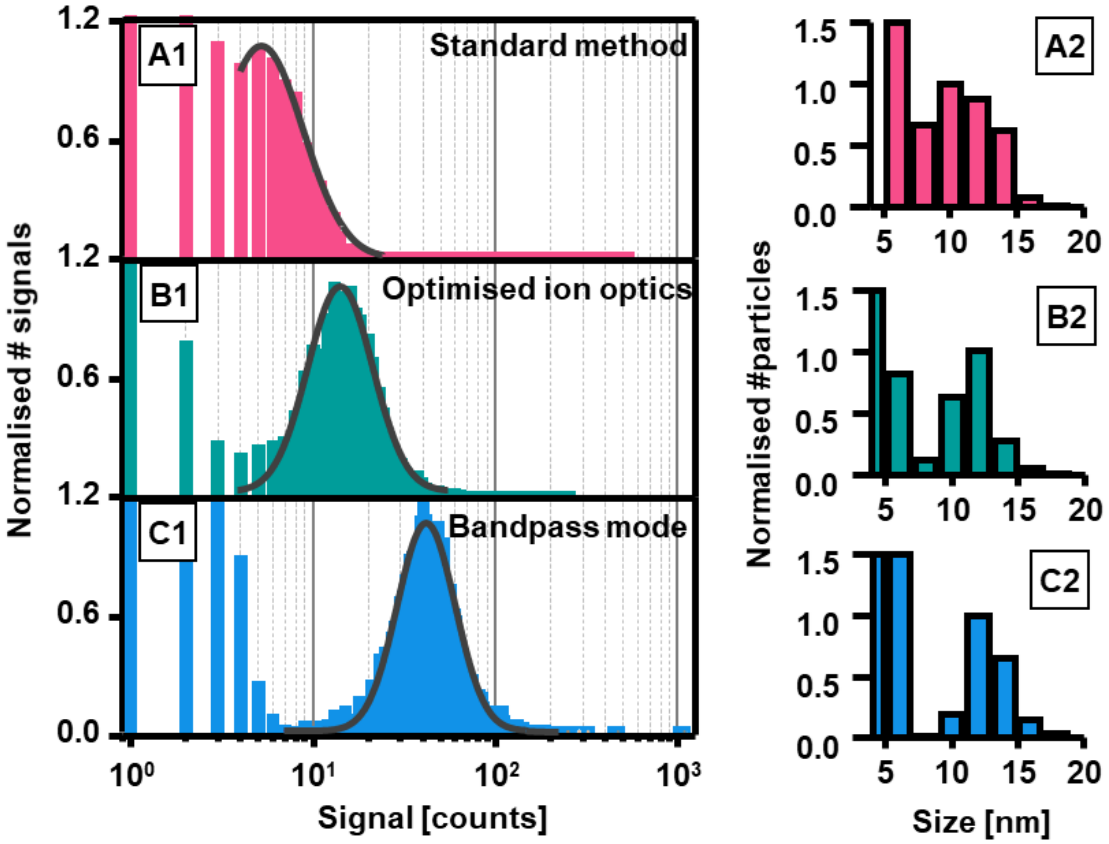

Figure 5-4: Analysis of a 10.9 nm AuNP dispersion. The standard method for SP ICP-MS (A1-2) is compared to a method with modified ion extraction and transport (B1-2). Operating the quadrupole additionally in the bandpass mode allows background-free NP detection (C1-2).

While a maximum in the NP signal distribution corresponding to the mean NP diameter could be resolved, lower NP diameters were not distinguishable from background signals. Figure 5-4 A2 shows the size distribution demonstrating interference of background signals with the size calculation. In this case, particles detected with sizes below the mean diameter were composed of signals originating from both background and NPs. The sDL was determined to be 7.0 nm. The optimization of ion extraction and transport increased transmission and translated into improved signal-to-noise ratios, as shown in Figure 5-4 B1, resulting in the improved differentiation of signals originating from AuNPs and background, which are composed of ions and noise. The improvement of the signal-to-noise ratio decreased the sDL from 7.0 to 4.7 nm. The corresponding

size distribution is displayed in Figure 5-4 B2. Further improvement was evident in the bandpass mode, which allowed complete resolution of AuNP signals from the ionic background and noise. This background-free detection of AuNP signals is shown in Figure 5-4 C1 and results in a higher accuracy of determined size distributions, as shown in Figure 5-4 C2. However, it needs to be considered that increasing the mass bandpass may have adverse effects on the background. Increasing noise concomitantly with ion transmission can therefore limit the improvement of signal-to-noise ratios. To monitor the effect of increasing transmission and mass bandpass on the background noise, a blank solution was analysed, and the standard deviation of signals was determined as a measure of noise. Values of 0.36, 0.46, and 0.83 counts were calculated for the standard method, the method with optimised ion optics, and the bandpass mode, respectively. The improvement in the signal-to-noise ratio using with the bandpass mode was therefore 3.7. Applying equation 6-4, the sDL was estimated to be 4.2 nm [298]. The sDLs for all elements and methods are shown in Table 5-3.

Table 5-3: sDLs for Y, Gd, Er, Yb, and Au for all types of NPs analyzed. Y was analyzed employing the optimised ion optics (OIO) method. Lanthanides were analyzed employing the bandpass mode (BPM). For comparisons, the sDL for Au was also determined with the standard SP ICP-MS method (SM).

	Y [nm]	**Gd [nm]**	**Er [nm]**	**Yb [nm]**	**Au [nm]**
AuNP					SM: 7.0 OIO: 4.7 BPM: 4.2
Type I UCNP	OIO: 13.6		BPM: 20.1	BPM: 12.2	
Type II UCNP	OIO: 13.6		BPM: 25.3	BPM: 12.2	
Type III UCNP		BPM: 5.7	BPM: 20.1	BPM: 12.2	

It was apparent that increasing ion transmission improved the sDL by enhancing the signal-to-noise ratios, allowing the characterisation of small AuNPs. Application of the method to other types of NPs must consider potential spectral interferences, the ionic background, and the background noise when increasing ion transmission, as the sDL is ultimately defined via the signal-to-noise ratio. Specifically, elements located in mass ranges where other elements are potentially interfering or likely to form polyatomic interferences (e.g., Y, Zn, and Fe) should be investigated with great care.

5.3.3 Characterisation of UCNPs

The properties of UCNPs depend largely on their size, dispersity, elemental composition, and stoichiometry as well as on their stability and the tendency to aggregate and to undergo species transformation. As such, the characterisation of UCNPs requires versatile methods. However, the analysis by SP ICP-MS is limited due to small particle sizes and low mass fractions of elements with broad isotope distributions.

Optimising ion extraction and transport and using the bandpass mode has the potential to improve sDL and to bring UCNPs within reach of SP ICP-MS. As a proof of concept, UCNPs with various diameters and elemental mass fractions were investigated; type I was a 90 nm $NaYF_4$ host structure in which 20% and 2% of Y lattice positions were substituted by Yb and Er, respectively; type II was a 20 nm sized $NaYF_4$ host structure in which 20% and 1% of Y lattice positions were replaced by Yb and Er, respectively; and type III was a 15 nm $NaGdF_4$ host structure in which 20% and 2% of the Gd lattice positions were replaced by Yb and Er, respectively.

Figure 5-5 shows the Yb signal distribution of the type II UCNP dispersion and clearly demonstrates the limitations of standard methods to provide background-free detection of small particles with low elemental mass fractions.

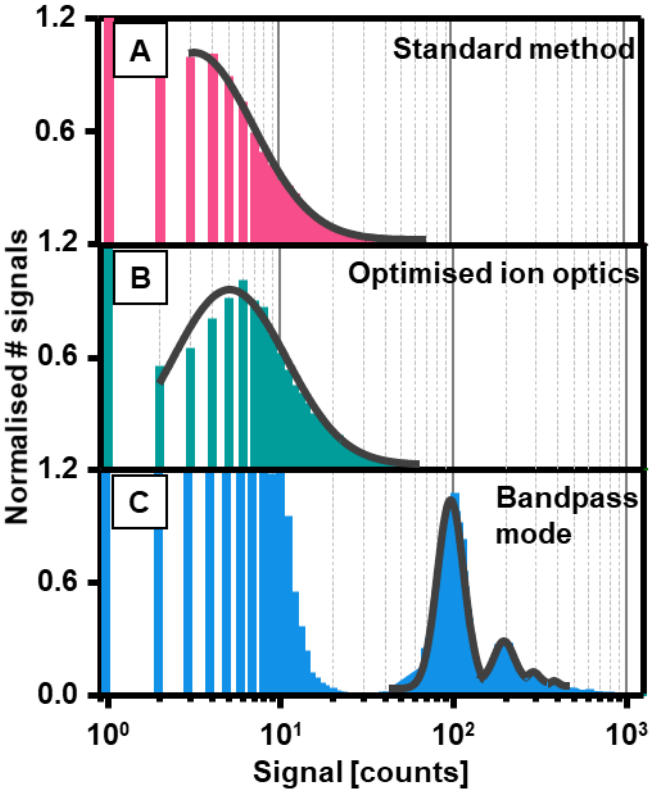

Figure 5-5: Yb signal distribution following single-particle analysis of dispersed 20 nm UCNPs ($NaYF_4$: 20% Yb, 1% Er, type II) using the standard method for SP ICP-MS (A). Particle registration was improved after optimising ion extraction and transport (B). The bandpass mode (C) allowed background-free detection of individual UCNPs and resolved several maxima corresponding to aggregated UCNPs.

Although the standard method did detect UCNP signals that were statistically distinguishable from the background (Figure 5-5 A), the smaller particles were confounded by the background. Modifying the ion lenses improved transmission and consequently the detection of individual UCNPs but did not provide background-free detection (Figure 5-5 B). For both signal distributions, neither Gaussian (not shown) nor lognormal (grey curve) functions provided an adequate fit. Figure 5-5 C featuring the operation of the bandpass mode shows several maxima in the signal distributions, which resulted from aggregation and the simultaneous detection of two or more particles. As these distributions could neither be resolved with the standard method nor with the method with optimised ion optics, simple Gaussian and log-normal fittings were not adequate. The bandpass mode was therefore critical to resolve signal distributions that resulted

from the simultaneous detection of two or more particles and may be utilised to describe particle−particle interactions as discussed later. As before, increasing ion transmission also increased the background noise. The standard deviation of the background for lanthanides increased from 0.06 counts for the standard method to 0.28 and 0.59 counts for the methods with optimised ion optics and the bandpass mode. Analysing Y with optimised ion optics increased the background noise from 0.37 to 0.93 counts.

The rapid sequential acquisition of several thousand NPs per minute was sufficient to construct statistically representative models for the size distribution of dispersed particles. Figure 5-6 shows the detection and characterisation of the three types of UCNPs.

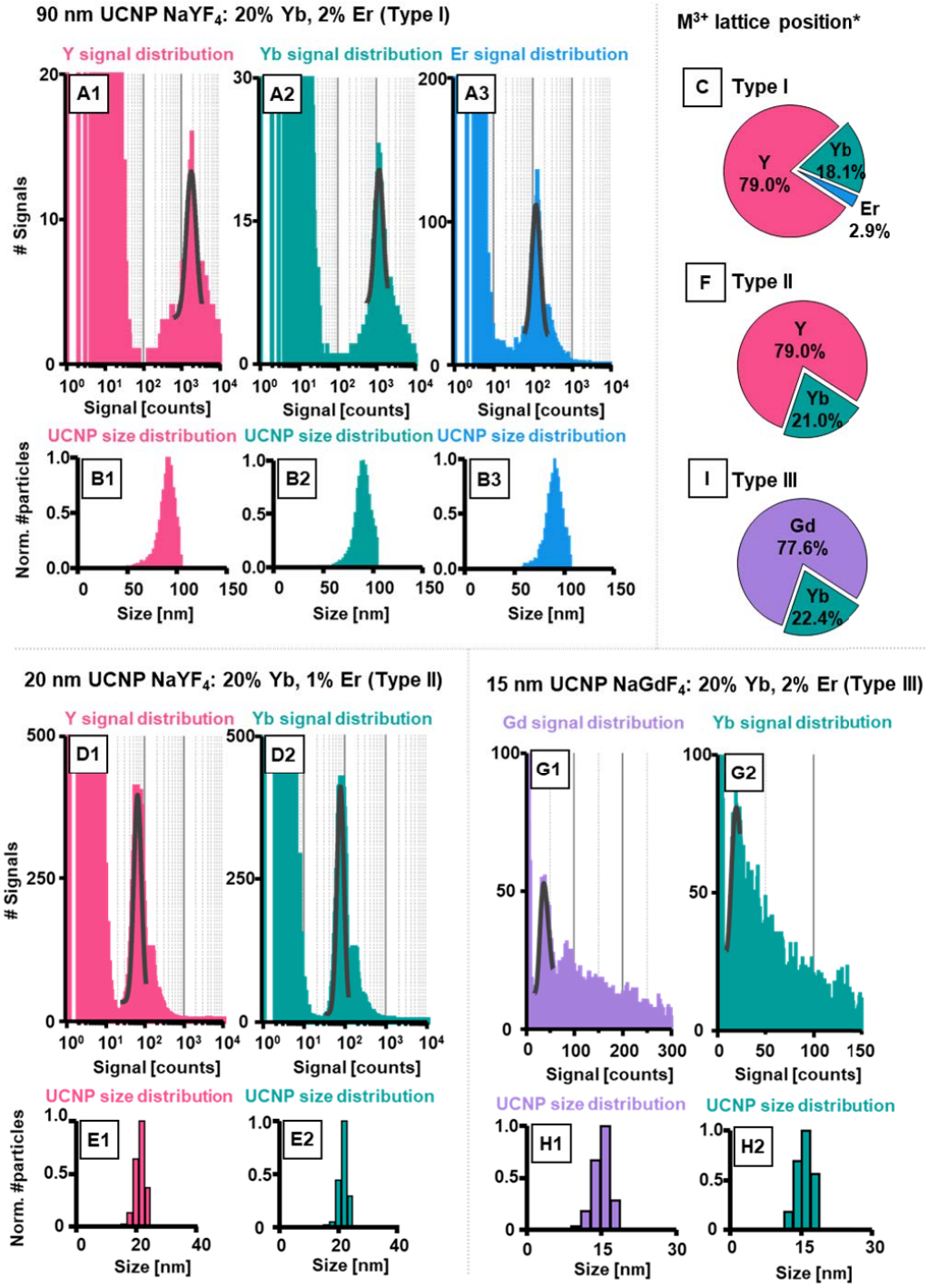

Figure 5-6: SP ICP-MS analyses of three types of UCNPs. Type I (top, (**A**)−(**C**)) consisted of a $NaYF_4$ host structure doped with 20% Yb and 2% Er. Type II (bottom left, (**D**)−(**F**)) consisted of a $NaYF_4$ host structure doped with 20% Yb and 1% Er. Type III (bottom right, (**G**)−(**I**)) consisted of a $NaGdF_4$ host structure doped with 20% Yb and 2% Er. The signal distributions for each type of UCNP and targeted elements are shown in (**A**), (**D**), and (**G**). Calibration allowed determination of the corresponding particle sizes as shown in (**B**), (**E**), and (**H**). The experimental molar ratios of targeted elements in detected UCNPs are shown in (**C**), (**F**), and (**I**). *For types II and III, Er was not detected and was not further considered.

The type I UCNP dispersion contained particles with mean sizes of 90 nm and consisted of a $NaYF_4$ host structure doped with Yb (theoretical doping degree, 0.2) and Er (theoretical doping degree, 0.02). Employing the high transmission methods provided background-free acquisition of signals from Y, Yb, and Er for individual NPs, as shown in Figure 5-6 A1−3. The targeting of various elements incorporated in UCNPs allowed determination of the stoichiometry and size distributions from different data sets, as shown in Figure 5-6 B1−3. Log-normal fit functions were used to find the first maxima of the signal distributions, which were subsequently used to determine the stoichiometry (0.79 Y:0.181 Yb:0.029 Er; Figure 5-6 C) considering the response of ionic elemental standards for ICP-MS. The type II UCNP dispersion consisted of a 20 nm $NaYF_4$ host structure doped with Yb (theoretical doping degree, 0.2) and Er (theoretical doping degree, 0.01). Modification of ion extraction and transport and increasing the mass bandwidth were essential to resolving signal distributions shown in Figure 5-6 D1−2. Due to the small diameters and low mass fractions, the doped Er was not observed for particles smaller than 25.3 nm and only Y and Yb were further considered for size distributions (Figure 5-6 E1−2). Figure 5-6 F shows the experimental ratio of Y to Yb (0.79:0.21). The type III 15 nm UCNPs ($NaGdF_4$ doped with Yb and Er) signal distributions are shown in Figure 5-6 G1−2. The optimization of ion transmission was again essential to resolve the first signal distribution maximum. The experimental ratio of Gd to Yb was 0.776:0.224, as shown in Figure 5-6 I (theoretical value, 0.8Gd:0.2Yb:0.02Er) and size distributions are shown in Figure 5-6 H1−2. The sDLs for each element, method, and particle type are shown in Table 5-3. For the analysis of UCNPs that contain Gd and Yb (e.g., type III UCNPs), oxide rates may impact accuracy. The oxide rate is mainly dependent on the solvent, the torch z-position and the nebulizer gas flow. If UCNPs consist of two elements with Δm=16 amu, oxides can interfere and bias results. In case of UCNP type I and II, which consisted of Er and Yb, a spectral overlap can be excluded. However, type III consisted of a GdF_4-host structure that was doped with Yb. The GdO formation and its impact on the Yb mass range was investigated by analysing an ionic Gd standard (1 $ng \cdot g^{-1}$) in bandpass mode. The GdO rate of 1.8% was detected as shown in Figure 5-7 and

was mathematically corrected for the calculation of the stoichiometry of UCNP type III.

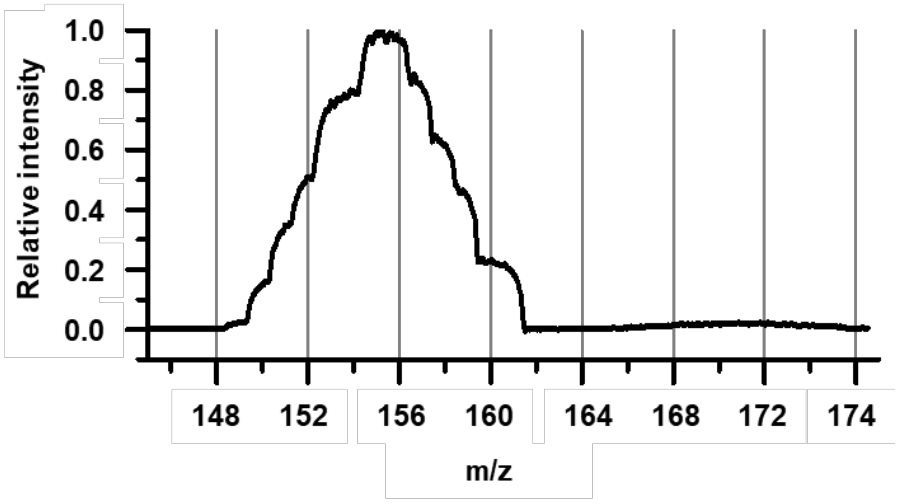

Figure 5-7: Mass spectrum covering the mass range for Gd and Yb isotopes in bandpass mode. For UCNP type III, GdO can interfere with the analysis of Yb. The oxide rate was determined to be 1.8% and its influence on the Yb determination was corrected mathematically.

5.3.4 Poisson model for UCNP interactions

Most of the UCNPs had two or more maxima in the signal distributions corresponding to the detection of two or more particles simultaneously. For an ideal NP dispersion with a sufficiently high particle concentration and no particle−particle interactions, the detection of none, one, or more particles may be described with a Poisson distribution [303]. Deviations from this distribution may be used to make an assessment about particle interactions, such as aggregation. Consider the type II UCNP dispersion (Figure 5-5 C). Here, the dispersion was freshly diluted by a factor of $3 \cdot 10^6$ and 0.525 mL was sampled. Overall, 37 862 particles were detected, of which 12 891 particles were detected individually. The high particle number concentration was chosen to demonstrate the utility of the Poisson statistics to predict the coincidental detection of two or more particles and for the comparison against a system that shows particle−particle interaction. The average signal duration of each signal was 400 µs (±19%), and the total acquisition time was 90 s. Based on these data, the

Poisson distribution was calculated with a variance of 0.3366 and is shown in Figure 5-8. From this model, it would be expected to within the model's standard deviation. Significantly increased frequencies were detected for three or more particles. The detection of three, four, and five particles occurred 4.4-times, 26.2-times, and 169-times more frequently, respectively, than that predicted by the Poisson model and were outside the model's standard deviation. The deviation from the Poisson distribution may be explained by particle−particle interactions that favour aggregation. Deviations from the Poisson model can therefore be used to make an assessment about the stability of dispersions in various matrices and solvents, which is an important factor for the utility of UCNPs in biosensing, deep-tissue optical bioimaging, and diagnostic techniques.

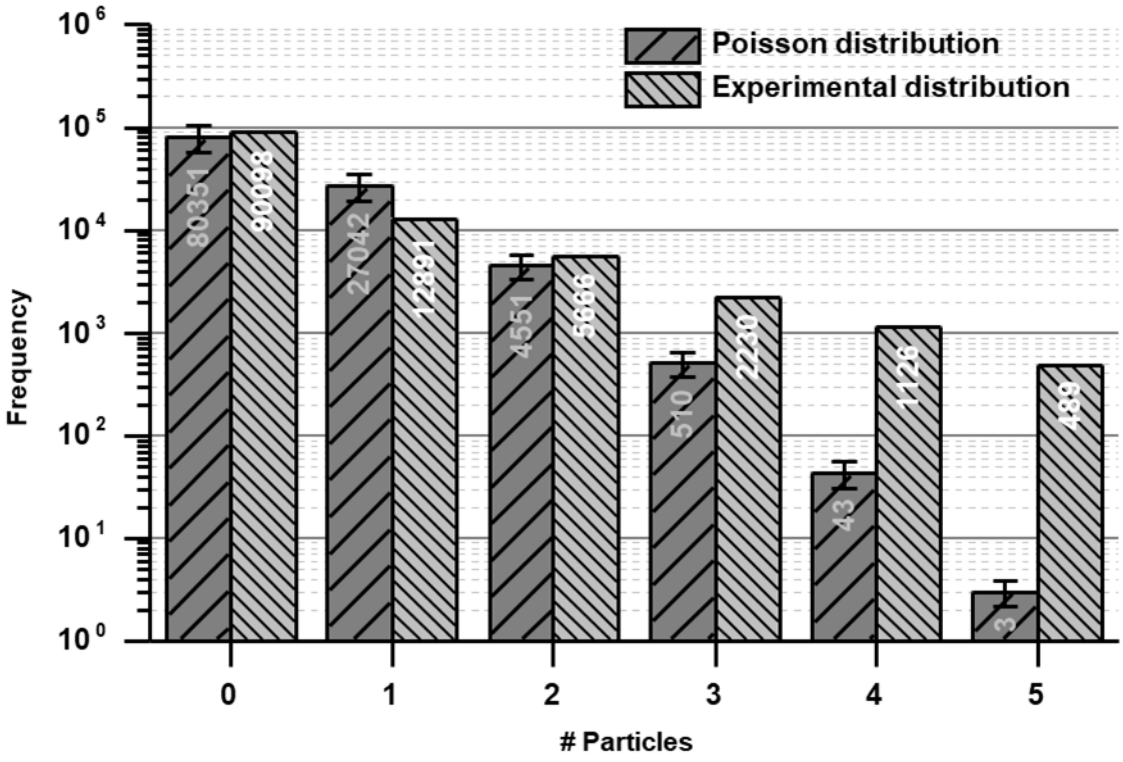

Figure 5-8: Comparison of the Poisson model and experimental results.

5.4 Conclusion

This chapter presented novel approaches to optimize ion transmission in SP ICP-MS for the analysis of small and low-mass-fraction NPs. Increasing the mass bandwidth of the quadrupole mass filter resulted in a decreased mass resolution and increased ion transmission, providing sDL as small as 4.2 nm for AuNPs and allowing the background-free size characterisation of a 10.9 nm (±1 nm) AuNP dispersion.

The developed methods were critical for the individual detection of UCNPs and the analysis of a variety of elements incorporated in these particles. Depending on masses, background equivalent concentrations, isotopic abundances, and spectral interferences, some elements required careful selection of transmission parameters. Y was confounded by spectral interferences and was therefore monitored with conventional quadrupole mass filtering and optimised ion extraction and transport parameters, achieving sDL as low as 13.6 nm. The bandpass mode improved the sensitivity for Gd, Er, and Yb substantially, providing sDLs as low as 5.7, 20.1, and 12.2 nm for the targeted UCNP compositions. This enabled the accurate characterisation of size distributions and particle doping degrees.

A Poisson model was developed to describe the aggregation of dispersed particles. The presented methods improved the detection of small or low-mass-fraction NPs and characterised UCNPs by SP ICP-MS for the first time. They can easily be adapted to the analysis of other NPs and have the potential to be used to study species transformation, particle number concentration, aggregation behaviour, doping degrees, and longitudinal stability.

Chapter

Elemental and Molecular Imaging of Manganese Transporters in Human Melanomas

6.1 Introduction

Rapid and uncontrolled growth of cancer may have altered metal uptake characteristics caused by varying expression of metal transporter proteins on the surface of the cells. A suitable technique to identify and map transporter proteins in the tumour microenvironment along with the metal distribution is LA-ICP-MS. This chapter demonstrates how the previously developed methods can be applied for the spatial investigation of metal-protein interactions, and addresses Aim 5, the imaging of manganese transporters and transition metals in human melanoma samples.

Cancer is one of the most common causes of death worldwide and accounted in 2016 for 22% off all globally recorded deaths [304,305]. The term categorises a range of diseases characterised by the uncontrolled growths and division of cells. Although most cancers are treated with radiotherapy its efficacy differs between and even within cancer types. The underlying principle which causes this widespread radioresistance in many human tumours remains, to this date, poorly understood. A novel hypothesis is that radioresistance is gained and maintained by non-enzymatic complexes of manganese with small molecule metabolites present in cells. These complexes are assumed to act as free radical scavengers, rendering cells variable resistant to the products of IR [9].

Manganese and other trace metals are essential for many physiological processes in the human body. These processes are highly regulated, and a variety of influx and efflux metal transporters are involved in their homeostasis. Considering the abnormality of cancerous tissue, these metal transporters might be differently expressed on the surface of cancer cells, leading to variable concentrations of manganese within tumours. Several transporter proteins are known to be involved in manganese uptake, including the proteins ZIP8 and ZIP14 which are expressed on the plasma membrane of cells. These transporter proteins are encoded by the SLC39 gene family, which consists of 14 members [25]. While most members only transport zinc, ZIP8 and ZIP14 are known to also transport manganese, iron and cadmium [26].

Elemental bioimaging by LA-ICP-MS is now a well-established instrumental method for elemental mapping of biological tissues [57,58]. The spatial analysis of biomolecules is also possible via incorporation of IHC [251,306] in the LA-ICP-MS imaging workflow, as known as iMSI. In iMSI, metal conjugated antibodies are used to determine the expression levels and location of proteins on the tissue sections. Several routinely used IHC protocols are available which either utilise directly labelled primary antibodies; or facilitate a two-step approach where an unlabelled primary antibody is first incubated to the tissue section and subsequently visualised with a labelled secondary antibody. The former offers the advantages of multiplexing and therefore the simultaneous visualization of multiple proteins. The latter provides more flexibility due to their applicability to a multitude of primary antibodies, and numerous pre-labelled and characterised secondary antibodies are available for purchase [83].

Lanthanide atoms are typically used as metal tags, due the advantage of a 100% ionization efficiency, a low background, and because they are usually not present in biological systems [83,86,307]. MAXPAR^{TM} labelling kits and protocols are commercially available and in the straightforward tagging procedure up to 100 isotopically enriched lanthanide atoms can be bound to a polymer that is conjugated with the antibody [93]. Silver and gold NPs are an interesting alternative to lanthanide tags, as they are biocompatible, inexpensive and easy to synthesise. Antibodies can be conjugated with NPs with a variety of mechanisms and conjugations kits are available for purchase. NPs are composed of several thousand atoms and can further improve the sensitivity for specific applications, however steric hindrance between antibody-NP conjugates can occur which limits multiplexing [83].

In scope of this work, we assess the feasibility of applying IMSI and EBI to spatially determine transporter proteins and transition elements to provide insights of the transporter pathway in human melanomas. A directly ^{153}Eu labelled anti-ZIP8 primary antibody was applied to image the ZIP8 expression levels, and on a successive slide, an unlabelled anti-ZIP14 primary antibody was visualised

with a secondary antibody-15 nm AuNP conjugate. The obtained protein transporter expressions were spatially compared with manganese, zinc, iron, and copper concentrations in a consecutive tissue sample.

6.2 Experimental Section

6.2.1 Chemicals and consumables

Ultrapure water was obtained from an Arium Pro system (Sartorius Stedim Plastics GmbH, Germany). An anti-ZIP8 antibody (PA5-21073) and an anti-ZIP14 antibody (PA-21077) were purchased from Thermo Fisher (Waltham, Massachusetts, USA). The former was labelled with ^{153}Eu using a by Fluidigm, formerly DVS Sciences (San Francisco, CA, USA) according to the manufacturer's standard protocol (version 4 06/13). An anti-rabbit IgG-AuNP conjugate with a diameter of 15 nm was acquired from Cytodiagnostics (Burlington, ON, Canada). All antibodies were stored at 4 °C. Seastar™ Baseline nitric acid and high purity manganese, iron, copper, and zinc standards (1000 mg·L^{-1}) for ICP-MS were obtained from Choice Analytical (Thornleigh, NSW, Australia). Iron(II) sulfate hydate (99.999% trace metal basis), zinc nitrate hydarate (99.999% trace metal basis), Tris-HCl (pH 7.4), ethylenediaminetetraacetic acid (EDTA; 10 mM), polyethylene glycol (Mn 400), gelatine from porcine skin (type A), xylenes (mixed isomers, IHC grade), ethanol (analytical grade), phosphate buffered saline, bovine serum albumin (fraction V), normal goat serum and triton X-100 were purchased from Sigma-Aldrich (Castle Hill, NSW, Australia). EnVision™ flex target retrieval solution high pH (50x) and serum-free protein block (0.25% casein) where acquired from Agilent Technologies Pathology (Dako) (Mulgrave, VIC, Australia). Bio-Rex 70 was obtained from Bio-Rad (Gladesville, NSW, Australia). HybriWell™ Sealing System were supplied by Grace Bio Labs (Bend, OR, USA)

6.2.2 Pathological material: tissue microarrays

The melanoma microarrays (ME481c) with a thickness of 5 µm were purchased from US Biomax, Inc (www.biomax.us). These microarrays contain cores of tumour and normal tissue of de-identified patients with data on the patients age, gender, pathology diagnosis and tumour stage available on the website; selected samples are listed in Table 6-1. Imaging of all H&E slides was performed with a Zeiss Axioscan Z1 (North Ryde, Australia) reviewed using ImageScope software from Aperio. The EBI and iMSI analyses were conducted at the UTS under the UTS HREC 2010-481 ethics approval.

Table 6-1: Specifications of the selected melanoma samples.

Sample	Age	Gender	Pathology diagnosis	Stage
1	45	M	Malignant melanoma of left foot	II
2	36	M	Malignant melanoma of left chest wall	II
3	77	F	Malignant melanoma of right toe	IIA
4	66	F	Malignant melanoma of chest wall	II
5	42	M	Malignant melanoma of chest wall	IV
6	44	F	Malignant melanoma of left heel	III
7	45	F	Malignant melanoma of left foot	IIB
8	37	M	Malignant melanoma of abdominal wall	II

6.2.3 Calibration standard preparation and quantification

Gelatine standard preparation

Porcine skin contains naturally abundant elements, such as manganese, iron, copper and zinc causing a background that needs to be removed to ensure a reliable quantification. Therefore, the gelatine standards for transition metals were prepared using a chelating resin as follows [308].

20% gelatine was prepared by dissolving 4 g of gelatine in 20 mL ultrapure water (45 °C, 110 rpm). 8 g of the chelating resin (Bio-Rex) was added to the liquid gelatine and mixed for 1 h (45 °C, 110 rpm). After centrifugation (1000 rpm, 5 minutes), the top layer was decanted and stored at room temperature. The transition metal standard solutions were prepared from either the 1000 ppm high-purity standard solutions for ICP-MS or from metal salts and diluted using a buffer solution compromised of 100 mM Tris-HCl buffer (pH 7.4), 10 mM EDTA and 1% w/w polyethylene glycol (Mn 400) in ultrapure water. The buffer solution is necessary to maintain the integrity of the gelatine at higher metal concentration. 500 uL chelated gelatine and 500 uL of the respective standard were mixed to obtain a gelatine concentration of 10%. 70 uL of the solutions were pipetted into commercially available HybriWell™ sealing system (6 moulds, 9.8 mm × 20 mm × 0.25 mm) and frozen at -80 °C for 5 minutes. After removing the mould, the gelatine standards were dried in the desiccator for 1 h and subsequently stored at room temperature. The final thickness of the gelatine standard was 26 µm as drying reduced the thickness tenfold.

Cross quantification via solution nebulization ICP-MS

For accurate concentration determination of the gelatine standards, 120 uL of each gelatine standard were pipetted into polyproylene tubes (previously weighed) and dried (100 °C, 1 h). After rehydration overnight, the tubes were weighed to determine the accurate gelatine mass. Subsequently 5 mL ultrapure nitric acid (2%) was added to each tube to digest the gelatine and the tubes were

placed into the Inccushaker (40 °C, 110 rpm, 1 h). For external calibration, an eight-point calibration curve ranging from 0 to 1.5-fold of the highest gelatine standard concentration was prepared in ultrapure nitric acid (2%). All gelatine standards were analysed in triplicate to calculate averages and standard deviations. The analysis was performed with two independently constructed external calibration curves, on two different instruments (Agilent 7700 series and Agilent 8900 series), and by employing Helium as collision/reaction gas when transition metals were analysed.

The determined concentrations of the gelatine standards listed in Table 6-2.

Table 6-2: Mn, Zn, Fe, Cu concentration levels [ppm] in the gelatine standards used for quantification of the tissue samples.

Level	**Mn [ppm]**	**Zn [ppm]**	**Fe [ppm]**	**Cu [ppm]**
0	0.0	1.6	1.4	0.1
1	0.1	3.4	5.8	0.3
2	0.2	9.6	17.6	0.7
3	0.8	37.8	76.7	2.5
4	2.8	140.7	421.8	9.2
5	11.3	397.1	1065.3	41.9

6.2.4 iMSI workflow

Antibody labelling and labelling characterisation

The primary anti-ZIP8 antibody was labelled with ^{153}Eu with a MAXPAR™ antibody conjugation kit (Fluidigm; formerly DVS Sciences, San Francisco, CA) according to the manufacturer's standard protocol. The average number of lanthanide tags per antibody was specified according to Clases *et al*. [309] using SEC-ICP-MS and on-line isotope dilution analysis and amounted to 89 metal tags per anti-ZIP8 antibody.

Immunohistochemical staining

Immunohistochemical staining was performed on Formalin Fixed Paraffin Embedded (FFPE) sections. The tissue sections were first heated to liquefy the paraffin (60 °C, 2 h) and then deparaffinised by immersing the slides in xylenes for 2 x 10 minutes, in 100% ethanol for 2 x 10 minutes, in 95% ethanol for 5 minutes, in 70% ethanol for 5 minutes and in PBS for 5 minutes. A heat induced epitope retrieval (HIER) was performed by heating the tissue section in citrate buffer, pH 6 (100 °C, 15 minutes). Subsequently, the slides were washed in PBS for 3 x 5 minutes before the staining procedure commenced.

Nonspecific binding of the antibody to other epitopes on the tissue was reduced by applying a blocking solution (500 µL 20% BSA, 300 µL NGS, 300 µL 10% Triton X-100 surfactant, 8900 µL PBS) onto the tissue sections for 30 minutes. For staining with the secondary antibody-AuNP conjugate, the tissue sections were additionally blocked with a Serum-Free Protein Block (0.25% Casein) for 10 minutes. The blocking solution was drained, and the tissue sections were incubated with a diluted antibody solution (1:300 for ^{153}Eu labelled anti-ZIP8, 1:100 for unlabelled anti-ZIP14) for 2 h. After 3 x 5 minutes PBS washes, a diluted solution (1:20) of a secondary antibody-15 nm AuNP conjugate was applied to the ZIP14 stained tissue section for 2 h. Following 3 x 5 minutes PBS washes,

the tissue sections were dried and stored at room temperature until LA-ICP-MS analysis.

6.2.5 LA-ICP-MS parameters

Standards and samples were analysed using a New Wave Research NWR193 ArF Laser Ablation System (Kenelec Scientific; Frenchs Forest, Australia), which was coupled to an Agilent 7900-series ICP-MS for iMSI and Agilent 8900-series ICP-MS for EBI. Both ICP-MS were equipped with Pt cones and x-lenses. High purity argon was used as plasma source and carrier gas. For EBI, 3.2 $mL \cdot min^{-1}$ ultra-high purity hydrogen gas was added as reaction gas to reduce polyatomic interferences. The LA-ICP-MS system was tuned for maximum sensitivity with the reference material NIST 612 Trace Elements in Glass. Minimum oxide formation was assured by monitoring m/z 248/232 (representing $^{232}Th^{16}O^{+}/^{232}Th^{+}$), which was required to be below 1%. The ICP-MS dwell times were set according to Lear et *al.* [59] to obtain square pixels maintaining the dimension of the sample.

The laser was driven with a frequency of 40 Hz, a spot size of 35 µm and a scan speed of 140 $\mu m \cdot s^{-1}$. The ICP-MS was operated with a radio frequency power of 1350 W, radio frequency matching was 1.14 V, sample depth was 4.0 mm, nebulizer gas was 1.15 L min, extraction lens 1 was 3.5 V, extraction lens 2 was -160.0 V, omega bias was -55 V and the omega lens was 10.4 V.

6.2.6 Data processing

The images were analysed and created with Pew^2 by Tom Lockwood (University of Technology, Sydney, Australia) [310]. The remaining figures were constructed with OriginPro (OriginLab, Version 9).

6.3 Results and Discussion

6.3.1 Comparison of protein visualization approaches

Proteins within tissue samples may be visualised with either labelled primary antibodies that are directly applied to the tissue, or alternatively, the tissue may be incubated with primary antibodies followed by incubation with labelled secondary antibodies. In both cases, the antibodies may be conjugated with a metal or NP of choice.

The feasibility of these visualization techniques for the spatial determination of metal transporter proteins in tissue samples was assessed via consideration of Figure 6-1. Here, the microscope image (left) and the images for the transporter proteins ZIP8 and ZIP14 were compared. The ZIP8 expression was visualised directly with ^{153}Eu labelled anti-ZIP8 primary antibody (middle), whilst the ZIP14 expression was visualised on a consecutive slide with an unlabelled anti-ZIP14 primary antibody and a secondary antibody-15 nm AuNP conjugate (right). Both images were obtained under the same conditions. Two tissue samples with similar ZIP8 and ZIP14 expression were initially selected to facilitate comparisons.

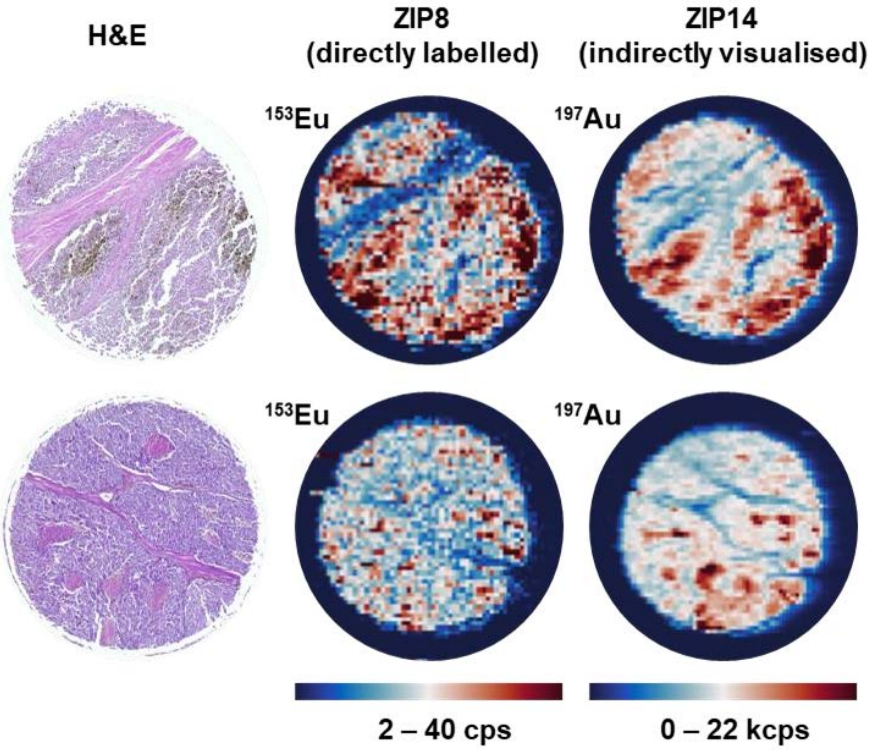

Figure 6-1: Microscope image (**left**) and iMSI images using two protein visualization approaches. The ZIP8 expression was visualised with a directly labelled ^{153}Eu-ZIP8 antibody (**middle**). The ZIP14 expression was visualised indirectly with an unlabelled ZIP14 antibody and a secondary antibody-15 nm AuNP conjugate (**right**).

Both approaches were suitable to spatially visualise the protein expression levels in the tissue samples. Areas of high and low expression were apparent in the tissue section and the regions show a good compliance with the cell structures in the microscope image. While both techniques are suitable to reflect a realistic distribution, a better sensitivity, signal-to-noise ratio, and image quality is achieved with the antibody-AuNP immunoassay. This is due to the significant differences in the numbers of atoms conjugated to the antibodies. AuNPs with a size of 15 nm consists of circa 104 076 Au atoms, while the anti-ZIP8 antibody was characterised to carry 89 ^{153}Eu labels per antibody. Furthermore, staining with secondary antibodies generally produces higher sensitivities as less steric hindrance occurs.

Nevertheless, both techniques offer advantages and disadvantages and may be selected with consideration of the application. Primary labelled antibodies save

time in the staining procedure and allow multiplexing. The actual labelling procedure is however lengthy, successful labelling is not guaranteed, and the number of tags per antibody differs widely between batches. The two-step approach with a pre-labelled secondary antibody produces higher intensities, allowing to visualise antigens present in small concentrations, they are easy to use, and can be applied to multiple primary antibodies. However, an additional step is necessary in the staining procedures, requires purchasing two antibodies, and multiplexing is impeded.

6.3.2 Elemental and molecular imaging of human melanomas

The same anti-ZIP8 and anti-ZIP14 antibodies were applied for concomitant iMSI and EBI of an array of 48 human melanoma samples to spatially determine transporter proteins and transition metals, and to investigate the link between protein expression and metal distribution. Consecutive tissue slides were used to image ZIP8, ZIP14 and the elemental composition as IHC staining is known to cause metal washouts. As expected, the results were quite diverse, and a summary of representative samples and regions of interest (ROIs) are summarised in Figure 6-2. Presented are the H&E image, ZIP8 and ZIP14 expressions, manganese, zinc, iron, and copper (left to right) in eight samples of human melanoma (top to bottom). The respective concentrations in the ROIs are listed in Table 6-3 and the maximum and minimum values are highlighted in red and blue.

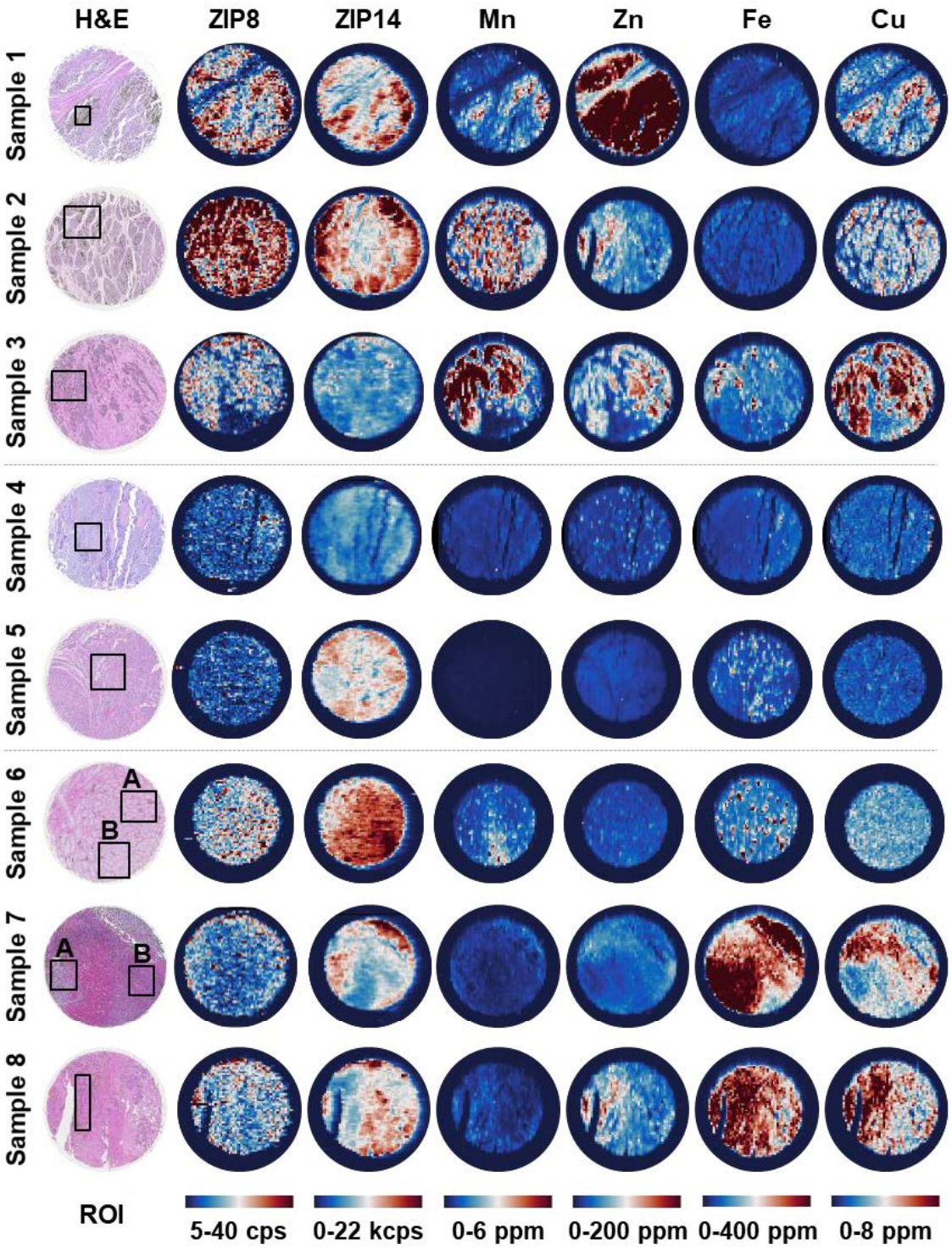

Figure 6-2: Comparison of the H&E image, ZIP8 and ZIP14 spatial distributions and transitions metals in eight samples of human melanoma.

Table 6-3: Signal intensities and concentrations in the selected ROIs. The maximum and minimum values are highlighted in red and blue.

	ZIP8 [cps]	ZIP14 [kcps]	Mn [ppm]	Zinc [ppm]	Fe [ppm]	Cu [ppm]
1	29.6 ± 4.2	**18.1 ± 1.5**	3.1 ± 0.5	**660.8 ± 90.8**	65.5 ± 8.7	5.3 ± 0.8
2	30.3 ± 4.3	12.3 ± 1.9	3.5 ± 0.8	131.9 ± 30.7	54.0 ± 10.5	3.3 ± 0.8
3	**37.1 ± 5.5**	6.9 ± 1.1	**7.1 ± 1.4**	71.0 ± 11.4	157.1 ± 47.7	6.4 ± 1.0
4	**11.6 ± 6.7**	**5.4 ± 0.6**	0.5 ± 0.1	**22.5 ± 4.7**	**44.7 ± 5.2**	1.8 ± 0.2
5	13.0 ± 2.5	9.6 ± 0.9	**0.1 ± 0.0**	25.4 ± 2.0	79.9 ± 23.1	**1.7 ± 0.2**
6A	19.8 ± 4.9	15.4 ± 0.8	2.3 ± 0.5	31.7 ± 3.8	125.3 ± 41.5	3.0 ± 0.3
6B	18.0 ± 6.2	16.7 ± 0.8	1.0 ± 0.2	27.3 ± 3.3	147.2 ± 57.9	2.8 ± 0.2
7A	26.7 ± 4.5	13.5 ± 1.0	0.5 ± 0.1	28.2 ± 5.1	**533.8 ± 127.2**	3.2 ± 0.7
7B	15.3 ± 2.4	8.7 ± 0.6	0.5 ± 0.0	42.7 ± 3.3	245.3 ± 21.5	4.7 ± 0.5
8	18.5 ± 3.8	7.6 ± 0.6	0.8 ± 0.2	93.2 ± 17.6	403.1 ± 43.3	**7.4 ± 1.1**

Sample 1 to 3 represent tumours with co-localisations between ZIP8, ZIP14 and (most) transition metals. The transporter proteins, manganese, and copper were high in the melanotic (dark) area of the tissue. Zinc and iron followed a different pattern in the first two melanomas but were similarly distributed in sample 3. Sample 4 and 5 were examples with low metal concentrations and corresponding low ZIP8 and ZIP14 levels. A co-localisation of iron and ZIP14 may be present in sample 5.

The remaining samples 6 to 8 illustrate special cases. Sample 6 was an example of varying manganese content within similar tissue structures of the same tumour (magnified in Figure 6-3). ROI A had an average of 2.3 ppm and ROI B and

average of 1.0 ppm manganese. The concentrations of the remaining transition metals were similar in the different ROIs and comparatively low for zinc, and in medium range for copper. ZIP8 correlated with iron in the melanotic areas.

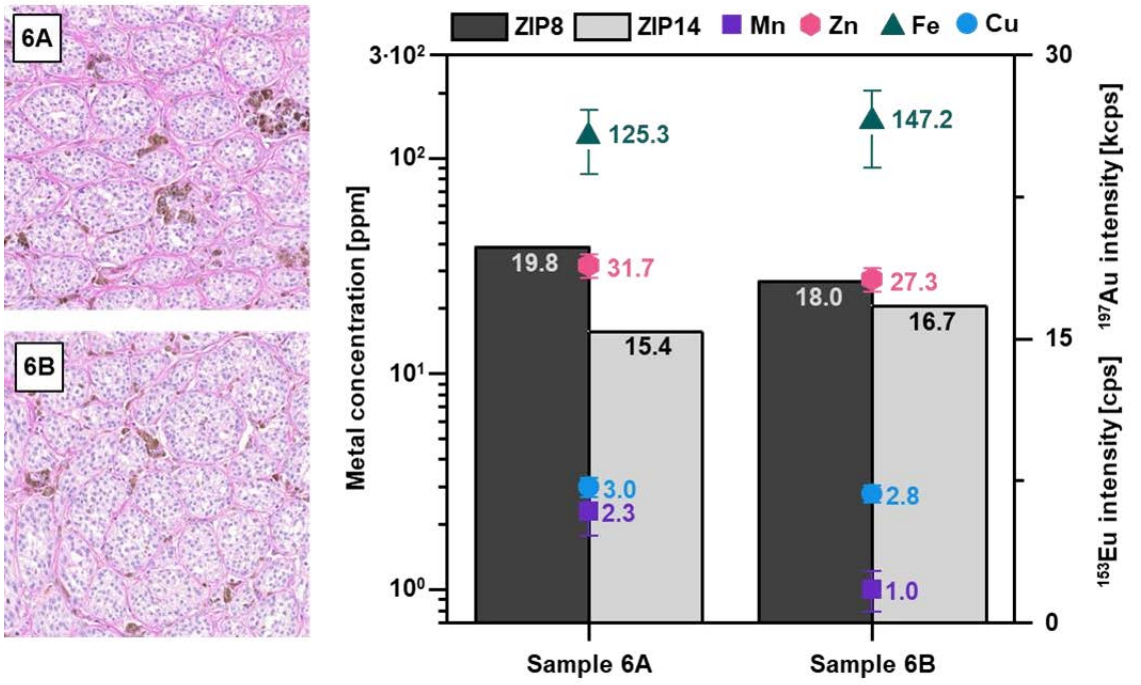

Figure 6-3: Light microscope image of ROI A and ROI B in sample 6 (left) and comparison of the average ZIP8 and ZIP14 expression levels as well as metal concentrations in the corresponding ROIs (right).

Sample 7 had varied ZIP8 and ZIP14 expressions in the different ROIs of the tumour (visualised in Figure 6-4), which were relatively high considering the low manganese concentration of only 0.5 ppm. ZIP14 and iron were somewhat co-localised, while copper had an opposite pattern.

A similar relation between manganese and transporter proteins was found in sample 8. The ZIP8 and ZIP14 expression levels were quite high which did not correlate with the low manganese concentration found in the tumour. These findings demonstrate the complex relationship between transporter proteins and metals. Seemingly multiple transporters were involved in manganese

homeostasis and particularly in this case, mechanisms facilitating the manganese export may be upregulated.

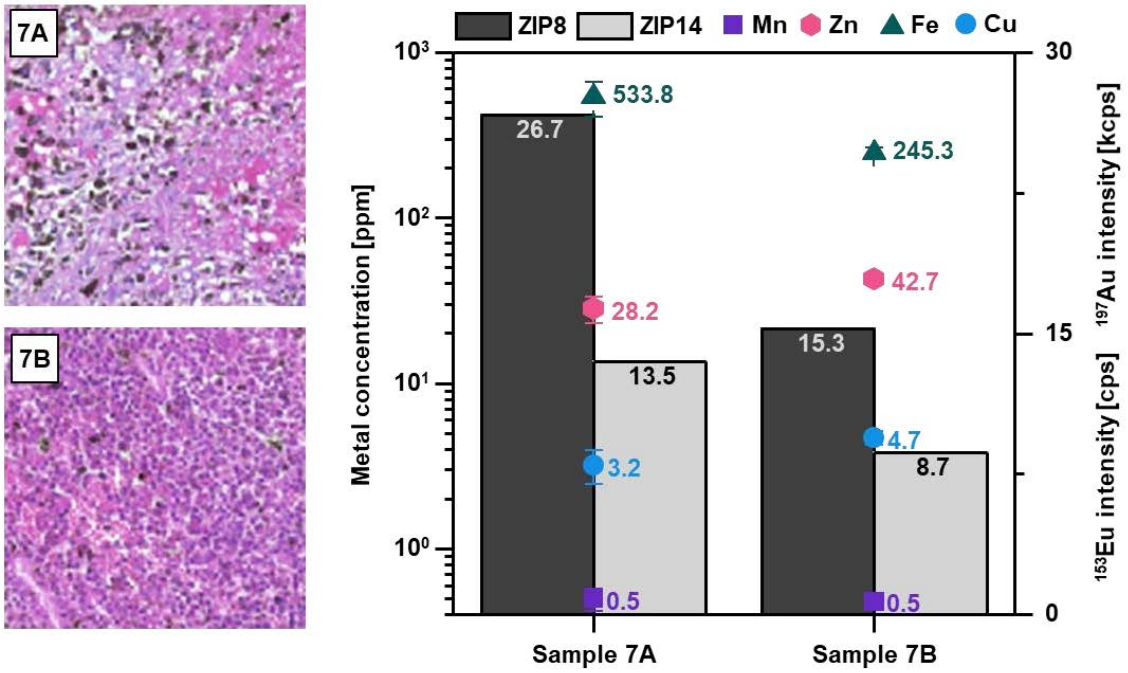

Figure 6-4: Light microscope image of ROI A and ROI B in sample 7 (left) and comparison of the average ZIP8 and ZIP14 expression levels as well as metal concentrations in the corresponding ROIs (right).

One consistent finding was the accumulation of manganese in melanotic tissues. This was mostly likely due to melanin's ability to chelate metal ions. Interestingly, ZIP8 and ZIP14 are also expressed in these areas, as the overlay in Figure 6-5 shows. The spatial overlap of manganese (red) and ZIP8 (blue) is shown as magenta, co-localisations of manganese (red) and ZIP14 (green) are yellow, and areas where all signals overlap are visualised in white.

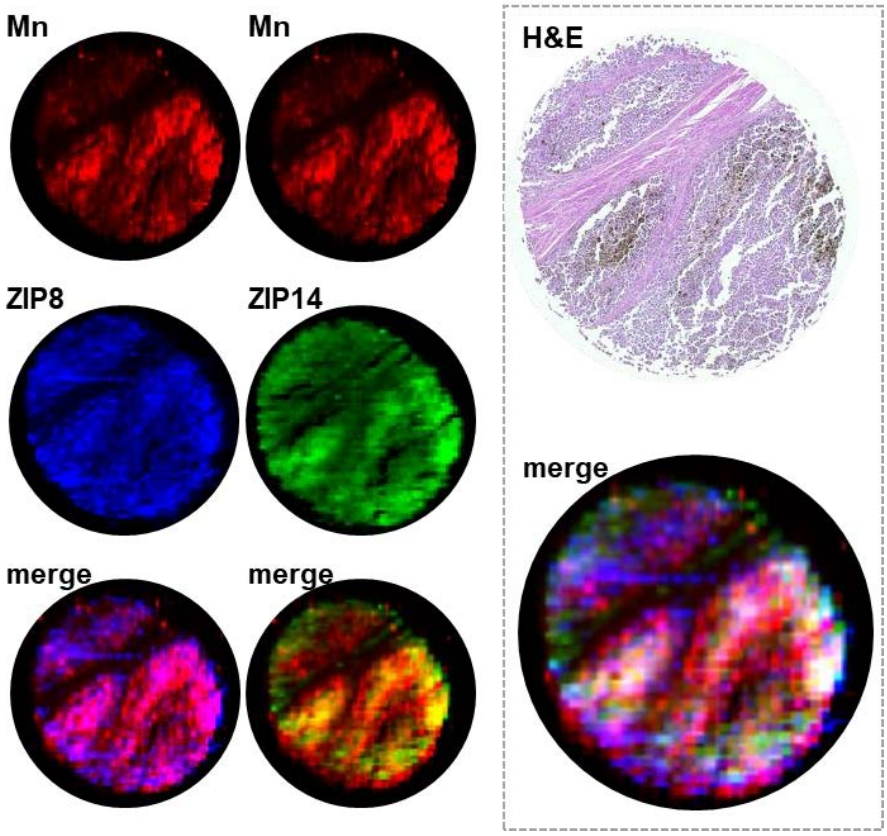

Figure 6-5: Co-localisation of manganese, ZIP8 and ZIP14 in melanotic tissues.

6.4 Conclusions

This chapter demonstrated the feasibility of applying concomitant iMSI and EBI to spatially localise the transporter proteins ZIP8 and ZIP14, and transition metals in samples of human melanoma.

Two antibody staining techniques were compared to visualise the ZIP8 and ZIP14 distribution within the tissue section. An anti-ZIP8 primary antibody was directly labelled with an ^{153}Eu loaded polymer, while an anti-ZIP14 antibody was envisioned with an antibody-AuNP immunoassay. Both techniques represented realistic protein distributions. Better sensitivity, signal-to-noise ratios and image quality was achieved with the NP immunoassay.

The proteins transporter expression levels were compared to manganese, iron, copper, and zinc concentrations in an array of human melanoma samples. The results were varied, due to the high number of importer and exporter proteins that regulate metal homeostasis in the human body. Some tumours had high manganese concentrations that were co-localised with high ZIP8 and ZIP14 levels. Others were found to be low in manganese, and ZIP8 and ZIP14 were sparsely expressed. A range of samples had less categorizable distributions with inconsistencies within tissue sections, or areas with high ZIP8 and ZIP14 expression, but low manganese levels.

Combining iMSI and EBI was a suitable approach to provide insights of the transporter pathway in human melanomas. Future research will be directed towards mapping a whole panel of manganese influx and efflux mechanisms in a range of human cancers.

6.5 Acknowledgements

Tom Lockwood, Raquel Gonzalez de Vega and David Clases are gratefully acknowledged for aid in the acquisition of the elemental bioimages and labelling characterisations.

Chapter

Summary and Future Perspectives

Understanding the underlying mechanisms of radioresistance and investigating the complex interplay between manganese and its transporter proteins requires the acquisition of reliable and high-quality interpretable data. This thesis presented several tools that addressed shortcomings of currently used techniques that are applicable to a variety of research pursuits in the biosciences.

In **Chapter 2**, a novel and universal workflow for the analysis of intact proteins with any pI and MW via CE was developed. The suitability of GC PDMS capillaries with dynamic coatings of cationic CTAB and anionic SDS, and BFS capillaries were evaluated for the analysis of seven model proteins in six BGEs with pH values ranging from 3.0 to 9.6. Multiple capillaries and BGE combination were applicable for the separation of each protein with the CTAB-PDMS capillary more suitable for low pH values, and the SDS-PDMS and BFS capillary superior in high pH values. The proteins electrophoretic mobility was dependent on the BGEs pH value and the optimal separation conditions may be estimated via knowledge of the proteins' pI. The illustrated guidelines were used to select the most suitable separation methods for the analysis of caseins and whey proteins in milk, including the isoforms of A1 and A2 β-casein and β-lactoglobulin A and B. The presented work shows high promise for the applicability in the proteomic field and future work will focus on the deployment of surfactants with longer carbon chains that will permanently absorb on the PDMS capillaries' surface, the use of zwitterionic surfactants which may provide alternate selectivities, and a systematic study on facilitating a total EOF control making CE analysis more customizable. Furthermore, tests on moving the protein solution through the capillary by pressure to prevent the adsorption of protein close to their pI will be conducted.

The sensitivity of CE analyses can be limited by the small injection volume. This issue was addresses in **Chapter 3** through the development of a simple, robust, and cost-effective interface for the hyphenation of CE and ICP-MS. The individual interface components were addressed, highlighting crucial factors that need to be considered during the assemblage of a CE-ICP-MS interface. This was

followed by the development of a method for the simultaneous analysis of five GBCAs which were selected as suitable model compounds. Finally, the interface's functionality, linearity, and robustness were evaluated with the compound-independent quantification of the liver specific GBCA gadoxetic acid in urine samples collected after MRI examination. On the technical side, future efforts will be guided toward developing a self-contained CE-ICP-MS interface that delivers the make-up flow through the outlet BGE vial of the CE system, as well as the design of a simple interface for the hyphenation of CE with a molecular MS. On the application site, development will be directed toward looking into metal contents and protein expressions on a cellular level.

In **Chapter 4**, the advancements made in the first two chapters were combined to characterise the labelling efficiencies of metal conjugated antibodies via CE-ICP-MS. Seven antibodies were conjugated with a gadolinium loaded polymer following a MAXPAR™ labelling protocol and the number of lanthanide ions per antibody was determined via CIC. Large variations in the labelling efficiency were found between different antibodies and antibodies of the same kind, emphasising the importance of reliable characterisation methods. The CE-ICP-MS method was further applied to 15 nm AuNPs and was feasible to distinguish between un-labelled and antibody conjugated NPs, making the technique an interesting approach for quality control aspects. Future work will be targeted towards optimising the CE method for the separation of individual antibody fragments, the conduction of a time study for antibody degradation, and the characterisation of labelling efficiencies before the antibody stabilizer is added. Furthermore, labelling degrees of antibody-NP conjugates will be determined by quantifying the metal and sulfur signal.

Chapter 5 presented novel methods for the characterisation of NPs regarding their composition, size distribution and particle-particle interactions by SP ICP-MS. Expanding the mass bandwidth of the quadruple mass filter resulted in an increased ion transmission and decreased mass resolution, allowing the background-free detection and size characterisation of 10.9 nm (±1 nm) AuNP

dispersions. The increased ion transmission was mandatory for the characterisation of UCNPs, which have multiple elements incorporated into their lattice structure. The transmission parameters had to be carefully optimised for each element and were dependent on the mass, isotopic abundances, and spectral interferences. The bandpass mode was for example not applicable to the element yttrium due to spectral interferences but suitable for the analysis of gadolinium, erbium, and ytterbium. The significant sensitivity improvements allowed the determination of size distributions and doping degrees of the targeted UNCPs. Lastly, a Poisson model was developed to describe the particle agglomeration in UCNP dispersions. The presented methods are adaptable to the characterisation of several other NPs, can be used for stability studies, or to monitor species transformations. Furthermore, future efforts will assess the feasibility of applying the developed approaches for the SP ICP-MS analysis of antibody-NP conjugates.

In **Chapter 6**, iMSI and EBI were concomitantly applied for the imaging of manganese transporters and transition metals in human melanomas. The ZIP8 transporter protein was visualised with an ^{153}Eu polymer labelled anti-ZIP8 antibody, while ZIP14 was envisioned over an immunoassay with a secondary antibody-AuNP conjugate. Both techniques represented realistic protein distributions, a better signal-to-noise ratio and image quality was achieved with the immunoassay. The protein transporter expression levels were compared with the manganese, iron, copper, and zinc concentration and variable results were observed underlining the complexity of metal homeostasis in biological systems. Some tumours had high manganese concentrations in areas with high ZIP8 and ZIP14 expression levels, other tumours were low in manganese and ZIP8 and ZIP14 were conjointly sparsely expressed. A variety of tumours showed no distinct relation indicating that other factors and mechanisms are involved in manganese transport. Future work will be directed toward the quantitative and multiplexed analysis of all identified manganese transporters in a variety of different cancer tissues and the expression levels will be compared to the transition metal concentration. An efficient statistical approach will be designed

for data analysis and an artificial intelligence-based recognition software will be developed to identify tumorous areas in H&E section which can then be compared to metal localisation and protein transporter expressions in the images.

Collectively this body of work has provided the foundation for the quantitative analysis of complex biological mechanisms. Over recent years, the imaging of biological specimens in terms of elemental and protein distributions has become extremely important. While elemental bioimaging by LA-ICP-MS is an established technique, the extension to the analysis of biomolecules via metal-tagged antibodies still has clear short comings. For example, the number of metal tags per antibody needs to be determined for each labelled antibody to allow quantitative assessments of the protein expression. Providing techniques that allow the determination of labelling efficiencies was the central aim of this PhD thesis and facilitated through the introduction of a series of methods based on CE and ICP-MS. In future work, these methods will be used to investigate the underlying mechanisms of tumour resistance to radiotherapy. Furthermore, they will have a wide applicability in different areas of the bioscientific field were a precise study of proteins, protein expression levels, and interactions of metals with biomolecules is required.

References

[1] G.M. Cooper, Elements of human cancer, Jones and Bartlett Publishers, 1992.

[2] I.R. Hart, A. Saini, Biology of tumour metastasis, Lancet. 339 (1992) 1453–1457. https://doi.org/10.1016/0140-6736(92)92039-I.

[3] F. Seif, M.R. Bayatiani, Cancer and Radiotherapy, J Arak Uni Med Sci. 21 (2015) 1–5.

[4] W. Schlegel, T. Bortfeld, A.-L. Grosu, New Technologies in Radiation Oncology, Springer Berlin Heidelberg, Berlin, Heidelberg, 2006. https://doi.org/10.1007/3-540-29999-8.

[5] D.E. Gerber, T.A. Chan, Recent Advances in Radiation Therapy, Am. Fam. Physician. 78 (2008) 1254–62.

[6] K. Kelley, J. Knisely, M. Symons, R. Ruggieri, Radioresistance of Brain Tumors, Cancers (Basel). 8 (2016) 42. https://doi.org/10.3390/cancers8040042.

[7] K. Rothkamm, M. Löbrich, Evidence for a lack of DNA double-strand break repair in human cells exposed to very low x-ray doses, Proc. Natl. Acad. Sci. 100 (2003) 5057–5062. https://doi.org/10.1073/pnas.0830918100.

[8] M. Goldstein, M.B. Kastan, The DNA Damage Response: Implications for Tumor Responses to Radiation and Chemotherapy, Annu. Rev. Med. 66 (2015) 129–143. https://doi.org/10.1146/annurev-med-081313-121208.

[9] P.A. Doble, G.L.G. Miklos, Distributions of manganese in diverse human cancers provide insights into tumour radioresistance, Metallomics. 10 (2018) 1191–1210. https://doi.org/10.1039/c8mt00110c.

[10] F.S. Archibald, I. Fridovich, Manganese and Defenses against Oxygen Toxicity in Lactobacillus plantarum, J. Bacteriol. 145 (1981) 442–451. https://doi.org/10.1128/jb.145.1.442-451.1981.

[11] F.S. Archibald, I. Fridovich, The scavenging of superoxide radical by manganous complexes: In vitro, Arch. Biochem. Biophys. 214 (1982) 452–

463. https://doi.org/10.1016/0003-9861(82)90049-2.

[12] M.J. Daly, E.K. Gaidamakova, V.Y. Matrosova, A. Vasilenko, M. Zhai, A. Venkateswaran, M. Hess, M. V. Omelchenko, H.M. Kostandarithes, K.S. Makarova, L.P. Wackett, J.K. Fredrickson, D. Ghosal, Accumulation of Mn(II) in Deinococcus radiodurans Facilitates Gamma-Radiation Resistance, Science (80-.). 306 (2004) 1025–1028. https://doi.org/10.1126/science.1103185.

[13] M.J. Daly, E.K. Gaidamakova, V.Y. Matrosova, A. Vasilenko, M. Zhai, R.D. Leapman, B. Lai, B. Ravel, S.-M.W. Li, K.M. Kemner, J.K. Fredrickson, Protein Oxidation Implicated as the Primary Determinant of Bacterial Radioresistance, PLoS Biol. 5 (2007) e92. https://doi.org/10.1371/journal.pbio.0050092.

[14] A. Krisko, M. Radman, Protein damage and death by radiation in Escherichia coli and Deinococcus radiodurans., Proc. Natl. Acad. Sci. U. S. A. 107 (2010) 14373–7. https://doi.org/10.1073/pnas.1009312107.

[15] V.C. Culotta, M.J. Daly, Manganese Complexes: Diverse Metabolic Routes to Oxidative Stress Resistance in Prokaryotes and Yeast, Antioxid. Redox Signal. 19 (2012) 933–944. https://doi.org/10.1089/ars.2012.5093.

[16] P. Gupta, M. Gayen, J.T. Smith, E.K. Gaidamakova, V.Y. Matrosova, O. Grichenko, B. Knollmann-Ritschel, M.J. Daly, J.G. Kiang, R.K. Maheshwari, MDP: A Deinococcus Mn2+-decapeptide complex protects mice from ionizing radiation, PLoS One. 11 (2016) 1–22. https://doi.org/10.1371/journal.pone.0160575.

[17] K.J. Horning, S.W. Caito, K.G. Tipps, A.B. Bowman, M. Aschner, Manganese Is Essential for Neuronal Health, Annu. Rev. Nutr. 35 (2015) 71–108. https://doi.org/10.1146/annurev-nutr-071714-034419.

[18] C. Au, A. Benedetto, M. Aschner, Manganese transport in eukaryotes: The role of DMT1, Neurotoxicology. 29 (2008) 569–576. https://doi.org/10.1016/j.neuro.2008.04.022.

[19] T.E. Gunter, B. Gerstner, K.K. Gunter, J. Malecki, R. Gelein, W.M. Valentine, M. Aschner, D.I. Yule, Manganese transport via the transferrin mechanism, Neurotoxicology. 34 (2013) 118–127. https://doi.org/10.1016/j.neuro.2012.10.018.

[20] H. Gunshin, B. Mackenzie, U. V Berger, Y. Gunshin, M.F. Romero, W.F. Boron, S. Nussberger, J.L. Gollan, M.A. Hediger, Cloning and characterization of a mammalian proton-coupled metal-ion transporter, Nature. 388 (1997) 482–488. https://doi.org/10.1038/41343.

[21] M.D. Garrick, K.G. Dolan, C. Horbinski, A.J. Ghio, D. Higgins, M. Porubcin,

E.G. Moore, L.N. Hainsworth, J.N. Umbreit, M.E. Conrad, L. Feng, A. Lis, J.A. Roth, S. Singleton, L.M. Garrick, DMT1: A mammalian transporter for multiple metals, BioMetals. 16 (2003) 41–54. https://doi.org/10.1023/A:1020702213099.

[22] J.R. Forbes, P. Gros, W. Dc, (Slc11a2) expressed at the plasma membrane Iron , manganese , and cobalt transport by Nramp1 (Slc11a1) and Nramp2 (Slc11a2) expressed at the plasma membrane, Transport. 102 (2011) 1884–1892. https://doi.org/10.1182/blood-2003-02-0425.

[23] J. Crossgrove, Manganese Distribution Across the Blood–Brain Barrier III The Divalent Metal Transporter-1 is not the Major Mechanism Mediating Brain Manganese Uptake, Neurotoxicology. 25 (2004) 451–460. https://doi.org/10.1016/j.neuro.2003.10.005.

[24] K.J. Horning, S.W. Caito, K.G. Tipps, A.B. Bowman, M. Aschner, Manganese Is Essential for Neuronal Health, Annu. Rev. Nutr. 35 (2015) 71–108. https://doi.org/10.1146/annurev-nutr-071714-034419.

[25] L. He, ZIP8, member of the solute-carrier-39 (SLC39) metal-transporter family: characterization of transporter properties, Mol. Pharmacol. 70 (2006) 171–180. https://doi.org/10.1124/mol.106.024521.

[26] S. Mukhopadhyay, Familial manganese-induced neurotoxicity due to mutations in SLC30A10 or SLC39A14, Neurotoxicology. 64 (2018) 278–283. https://doi.org/10.1016/j.neuro.2017.07.030.

[27] H. Fujishiro, Y. Yano, Y. Takada, M. Tanihara, S. Himeno, Roles of ZIP8, ZIP14, and DMT1 in transport of cadmium and manganese in mouse kidney proximal tubule cells, Metallomics. 4 (2012) 700–708. https://doi.org/10.1039/c2mt20024d.

[28] K. Girijashanker, L. He, M. Soleimani, J.M. Reed, H. Li, Z. Liu, B. Wang, T.P. Dalton, D.W. Nebert, Slc39a14 Gene Encodes ZIP14, A Metal/Bicarbonate Symporter: Similarities to the ZIP8 Transporter, Mol. Pharmacol. 73 (2008) 1413–1423. https://doi.org/10.1124/mol.107.043588.

[29] J.A. Kozak, M.D. Cahalan, MIC Channels Are Inhibited by Internal Divalent Cations but Not ATP, Biophys. J. 84 (2003) 922–927. https://doi.org/10.1016/s0006-3495(03)74909-1.

[30] M.K. Monteilh-Zoller, M.C. Hermosura, M.J.S. Nadler, A.M. Scharenberg, R. Penner, A. Fleig, TRPM7 Provides an Ion Channel Mechanism for Cellular Entry of Trace Metal Ions, J. Gen. Physiol. 121 (2003) 49–60. https://doi.org/10.1085/jgp.20028740.

[31] L.W. Runnels, L. Yue, D.E. Clapham, TRP-PLIK, a bifunctional protein with

kinase and ion channel activities, Science (80-.). 291 (2001) 1043–1047. https://doi.org/10.1126/science.1058519.

[32] L. V. Ryazanova, M. V. Dorovkov, A. Ansari, A.G. Ryazanov, Characterization of the Protein Kinase Activity of TRPM7/ChaK1, a Protein Kinase Fused to the Transient Receptor Potential Ion Channel, J. Biol. Chem. 279 (2004) 3708–3716. https://doi.org/10.1074/jbc.M308820200.

[33] K. Loutzenhiser, R. Loutzenhiser, Angiotensin II–Induced Ca 2+ Influx in Renal Afferent and Efferent Arterioles, Circ. Res. 87 (2000) 551–557. https://doi.org/10.1161/01.RES.87.7.551.

[34] J. Roth, S. Ponzoni, M. Aschner, Manganese Homeostasis and Transport, Coord. Chem. Rev. 257 (2013) 169–201. https://doi.org/10.1007/978-94-007-5561-1_6.

[35] M. Aschner, J.L. Aschner, Manganese transport across the blood-brain barrier: Relationship to iron homeostasis, Brain Res. Bull. 24 (1990) 857–860. https://doi.org/10.1016/0361-9230(90)90152-P.

[36] M. Aschner, M. Gannon, Manganese (Mn) transport across the rat blood-brain barrier: Saturable and transferrin-dependent transport mechanisms, Brain Res. Bull. 33 (1994) 345–349. https://doi.org/10.1016/0361-9230(94)90204-6.

[37] L. Davidsson, B. Lönnerdal, B. Sandström, C. Kunz, C.L. Keen, Identification of Transferrin as the Major Plasma Carrier Protein for Manganese Introduced Orally or Intravenously or After In Vitro Addition in the Rat, J. Nutr. 119 (1989) 1461–1464. https://doi.org/10.1093/jn/119.10.1461.

[38] A. Carmona, C.E. Zogzas, S. Roudeau, F. Porcaro, J. Garrevoet, K.M. Spiers, M. Salomé, P. Cloetens, S. Mukhopadhyay, R. Ortega, SLC30A10 Mutation Involved in Parkinsonism Results in Manganese Accumulation within Nanovesicles of the Golgi Apparatus, ACS Chem. Neurosci. 10 (2019) 599–609. https://doi.org/10.1021/acschemneuro.8b00451.

[39] D. Leyva-Illades, P. Chen, C.E. Zogzas, S. Hutchens, J.M. Mercado, C.D. Swaim, R.A. Morrisett, A.B. Bowman, M. Aschner, S. Mukhopadhyay, SLC30A10 Is a Cell Surface-Localized Manganese Efflux Transporter, and Parkinsonism-Causing Mutations Block Its Intracellular Trafficking and Efflux Activity, J. Neurosci. 34 (2014) 14079–14095. https://doi.org/10.1523/JNEUROSCI.2329-14.2014.

[40] C.A. Taylor, S. Hutchens, C. Liu, T. Jursa, W. Shawlot, M. Aschner, D.R. Smith, S. Mukhopadhyay, SLC30A10 transporter in the digestive system regulates brain manganese under basal conditions while brain SLC30A10 protects against neurotoxicity, J. Biol. Chem. 294 (2019) 1860–1876.

https://doi.org/10.1074/jbc.RA118.005628.

[41] Z. Yin, H. Jiang, E.-S.Y. Lee, M. Ni, K.M. Erikson, D. Milatovic, A.B. Bowman, M. Aschner, Ferroportin is a manganese-responsive protein that decreases manganese cytotoxicity and accumulation, J. Neurochem. 112 (2010) 1190–1198. https://doi.org/10.1111/j.1471-4159.2009.06534.x.

[42] M.S. Madejczyk, N. Ballatori, The iron transporter ferroportin can also function as a manganese exporter, Biochim. Biophys. Acta - Biomembr. 1818 (2012) 651–657. https://doi.org/10.1016/j.bbamem.2011.12.002.

[43] B. Waghorn, Y. Yang, A. Baba, T. Matsuda, A. Schumacher, N. Yanasak, T.C.C. Hu, Assessing manganese efflux using SEA0400 and cardiac T1-mapping manganese-enhanced MRI in a murine model, NMR Biomed. 22 (2009) 874–881. https://doi.org/10.1002/nbm.1414.

[44] B. Waghorn, A. Schumacher, J. Liu, S. Jacobs, A. Baba, T. Matsuda, N. Yanasak, T.C.-C. Hu, Indirectly probing Ca2+ handling alterations following myocardial infarction in a murine model using T1-mapping manganese-enhanced magnetic resonance imaging, Magn. Reson. Med. 65 (2011) 239–249. https://doi.org/10.1002/mrm.22597.

[45] A.M. Tidball, M.R. Bryan, M.A. Uhouse, K.K. Kumar, A.A. Aboud, J.E. Feist, K.C. Ess, M.D. Neely, M. Aschner, A.B. Bowman, A novel manganese-dependent ATM-p53 signaling pathway is selectively impaired in patient-based neuroprogenitor and murine striatal models of Huntington's disease, Hum. Mol. Genet. 24 (2015) 1929–1944. https://doi.org/10.1093/hmg/ddu609.

[46] S.P. Yu, D.W. Choi, Na+ - Ca2+ Exchange Currents in Cortical Neurons: Concomitant Forward and Reverse Operation and Effect of Glutamate, Eur. J. Neurosci. 9 (1997) 1273–1281. https://doi.org/10.1111/j.1460-9568.1997.tb01482.x.

[47] A. Lis, T.A. Barone, P.N. Paradkar, R.J. Plunkett, J.A. Roth, Expression and localization of different forms of DMT1 in normal and tumor astroglial cells, Mol. Brain Res. 122 (2004) 62–70. https://doi.org/10.1016/j.molbrainres.2003.11.023.

[48] M. Yang, W. Zhang, H. Dong, Y. Zhang, K. Lv, D. Wang, X. Lian, OsNRAMP3 is a vascular bundles-specific manganese transporter that is responsible for manganese distribution in rice, PLoS One. 8 (2013) 1–10. https://doi.org/10.1371/journal.pone.0083990.

[49] P. Chandler, B.S. Kochupurakkal, S. Alam, A.L. Richardson, D.I. Soybel, S.L. Kelleher, Subtype-specific accumulation of intracellular zinc pools is associated with the malignant phenotype in breast cancer, Mol. Cancer. 15 (2016) 1–19. https://doi.org/10.1186/s12943-015-0486-y.

[50] Z.K. Pinnix, L.D. Miller, W. Wang, R. D'Agostino, T. Kute, M.C. Willingham, H. Hatcher, L. Tesfay, G. Sui, X. Di, S. V. Torti, F.M. Torti, Ferroportin and Iron Regulation in Breast Cancer Progression and Prognosis, Sci. Transl. Med. 2 (2010) 43ra56-43ra56. https://doi.org/10.1126/scisignal.3001127.

[51] J.S. Becker, N. Jakubowski, The synergy of elemental and biomolecular mass spectrometry: New analytical strategies in life sciences, Chem. Soc. Rev. 38 (2009) 1969–1983. https://doi.org/10.1039/b618635c.

[52] P.A. Doble, R.G. de Vega, D.P. Bishop, D.J. Hare, D. Clases, Laser ablation-inductively coupled plasma-mass spectrometry imaging in biology, Chem. Rev. 121 (2021) 11769–11822. https://doi.org/10.1021/acs.chemrev.0c01219.

[53] K. Jurowski, B. Buszewski, W. Piekoszewski, Bioanalytics in Quantitive (Bio)imaging/Mapping of Metallic Elements in Biological Samples, Crit. Rev. Anal. Chem. 45 (2015) 334–347. https://doi.org/10.1080/10408347.2014.941455.

[54] Z. Qin, J.A. Caruso, B. Lai, A. Matusch, J.S. Becker, Trace metal imaging with high spatial resolution: Applications in biomedicine, Metallomics. 3 (2011) 28–37. https://doi.org/10.1039/c0mt00048e.

[55] A.L. Gray, Solid sample introduction by laser ablation for inductively coupled plasma source mass spectrometry, Analyst. 110 (1985) 551. https://doi.org/10.1039/an9851000551.

[56] S. Wang, R. Brown, D.J. Gray, Application of Laser Ablation-ICPMS to the Spatially Resolved Micro-Analysis of Biological Tissue, Appl. Spectrosc. 48 (1994) 1321–1325. https://doi.org/10.1366/0003702944028001.

[57] J. Koch, D. Günther, Review of the state-of- The-art of laser ablation inductively coupled plasma mass spectrometry, Appl. Spectrosc. 65 (2011) 155–162. https://doi.org/10.1366/11-06255.

[58] D. Hare, C. Austin, P. Doble, Quantification strategies for elemental imaging of biological samples using laser ablation-inductively coupled plasma-mass spectrometry, Analyst. 137 (2012) 1527–1537. https://doi.org/10.1039/c2an15792f.

[59] J. Lear, D. Hare, P. Adlard, D. Finkelstein, P. Doble, Improving acquisition times of elemental bio-imaging for quadrupole-based LA-ICP-MS, J. Anal. At. Spectrom. 27 (2012) 159–164. https://doi.org/10.1039/c1ja10301f.

[60] I. Konz, B. Fernández, M.L. Fernández, R. Pereiro, A. Sanz-Medel, Laser ablation ICP-MS for quantitative biomedical applications, Anal. Bioanal. Chem. 403 (2012) 2113–2125. https://doi.org/10.1007/s00216-012-6023-6.

[61] M.T. Westerhausen, T.E. Lockwood, R. Gonzalez De Vega, A. Röhnelt, D.P. Bishop, N. Cole, P.A. Doble, D. Clases, Low background mould-prepared gelatine standards for reproducible quantification in elemental bio-imaging, Analyst. 144 (2019) 6881–6888. https://doi.org/10.1039/c9an01580a.

[62] D. Hare, F. Burger, C. Austin, F. Fryer, R. Grimm, B. Reedy, R.A. Scolyer, J.F. Thompson, P. Doble, Elemental bio-imaging of melanoma in lymph node biopsies, Analyst. 134 (2009) 450–453. https://doi.org/10.1039/b812745j.

[63] D.J. Hare, J. Lear, D. Bishop, A. Beavis, P.A. Doble, Protocol for production of matrix-matched brain tissue standards for imaging by laser ablation-inductively coupled plasma-mass spectrometry, Anal. Methods. 5 (2013) 1915–1921. https://doi.org/10.1039/c3ay26248k.

[64] O. Reifschneider, K.S. Wentker, K. Strobel, R. Schmidt, M. Masthoff, M. Sperling, C. Faber, U. Karst, Elemental bioimaging of thulium in mouse tissues by laser ablation-icpms as a complementary method to heteronuclear proton magnetic resonance imaging for cell tracking experiments, Anal. Chem. 87 (2015) 4225–4230. https://doi.org/10.1021/ac504363q.

[65] D.P. Bishop, D. Clases, F. Fryer, E. Williams, S. Wilkins, D.J. Hare, N. Cole, U. Karst, P.A. Doble, Elemental bio-imaging using laser ablation-triple quadrupole-ICP-MS, J. Anal. At. Spectrom. 31 (2016) 197–202. https://doi.org/10.1039/C5JA00293A.

[66] R. González De Vega, M.L. Fernández-Sánchez, J. Pisonero, N. Eiró, F.J. Vizoso, A. Sanz-Medel, Quantitative bioimaging of Ca, Fe, Cu and Zn in breast cancer tissues by LA-ICP-MS, J. Anal. At. Spectrom. 32 (2017) 671–677. https://doi.org/10.1039/c6ja00390g.

[67] M. Šala, V.S. Šelih, J.T. Van Elteren, Gelatin gels as multi-element calibration standards in LA-ICP-MS bioimaging: Fabrication of homogeneous standards and microhomogeneity testing, Analyst. 142 (2017) 3356–3359. https://doi.org/10.1039/c7an01361b.

[68] C. Austin, D. Hare, T. Rawling, A.M. McDonagh, P. Doble, Quantification method for elemental bio-imaging by LA-ICP-MS using metal spiked PMMA films, J. Anal. At. Spectrom. 25 (2010) 722–725. https://doi.org/10.1039/b911316a.

[69] H.J. Stärk, R. Wennrich, A new approach for calibration of laser ablation inductively coupled plasma mass spectrometry using thin layers of spiked agarose gels as references, Anal. Bioanal. Chem. 399 (2011) 2211–2217. https://doi.org/10.1007/s00216-010-4413-1.

[70] S. Hoesl, B. Neumann, S. Techritz, M. Linscheid, F. Theuring, C. Scheler, N. Jakubowski, L. Mueller, Development of a calibration and standardization procedure for LA-ICP-MS using a conventional ink-jet printer for quantification of proteins in electro- and Western-blot assays, J. Anal. At. Spectrom. 29 (2014) 1282–1291. https://doi.org/10.1039/c4ja00060a.

[71] S. Hoesl, B. Neumann, S. Techritz, G. Sauter, R. Simon, H. Schlüter, M. W. Linscheid, F. Theuring, N. Jakubowski, L. Mueller, Internal standardization of LA-ICP-MS immuno imaging via printing of universal metal spiked inks onto tissue sections, J. Anal. At. Spectrom. 31 (2016) 801–808. https://doi.org/10.1039/c5ja00409h.

[72] C. Pickhardt, A. V. Izmer, M. V. Zoriy, D. Schaumlöffel, J. Sabine Becker, On-line isotope dilution in laser ablation inductively coupled plasma mass spectrometry using a microflow nebulizer inserted in the laser ablation chamber, Int. J. Mass Spectrom. 248 (2006) 136–141. https://doi.org/10.1016/j.ijms.2005.11.001.

[73] B. Fernández, P. Rodríguez-González, J.I. García Alonso, J. Malherbe, S. García-Fonseca, R. Pereiro, A. Sanz-Medel, On-line double isotope dilution laser ablation inductively coupled plasma mass spectrometry for the quantitative analysis of solid materials, Anal. Chim. Acta. 851 (2014) 64–71. https://doi.org/10.1016/j.aca.2014.08.017.

[74] D. Potter, A commercial perspective on the growth and development of the quadrupole ICP-MS market, J. Anal. At. Spectrom. 23 (2008) 690–693. https://doi.org/10.1039/b717322a.

[75] D. Pozebon, G.L. Scheffler, V.L. Dressler, M.A.G. Nunes, Review of the applications of laser ablation inductively coupled plasma mass spectrometry (LA-ICP-MS) to the analysis of biological samples, J. Anal. At. Spectrom. 29 (2014) 2204–2228. https://doi.org/10.1039/c4ja00250d.

[76] S.F. Durrant, N.I. Ward, Recent biological and environmental applications of laser ablation inductively coupled plasma mass spectrometry (LA-ICP-MS), J. Anal. At. Spectrom. 20 (2005) 821–829. https://doi.org/10.1039/b502206a.

[77] T.W. May, R.H. Wiedmeyer, A Table of Polyatomic Interferences in ICP-MS Isotope Abundance Interference, At. Spectrosc. 19 (1998) 150–155.

[78] D.S. Urgast, S. Hill, I.S. Kwun, J.H. Beattie, H. Goenaga-Infante, J. Feldmann, Zinc isotope ratio imaging of rat brain thin sections from stable isotope tracer studies by LA-MC-ICP-MS, Metallomics. 4 (2012) 1057–1063. https://doi.org/10.1039/c2mt20119d.

[79] J.S. Becker, M. Zoriy, A. Matusch, B. Wu, D. Salber, C. Palm, J.S. Becker,

Bioimaging of metals by laser ablation inductively coupled plasma mass spectrometry (LA-ICP-MS), Mass Spectrom. Rev. 29 (2010) 156–175. https://doi.org/10.1002/mas.20239.

[80] J. Lear, D.J. Hare, F. Fryer, P.A. Adlard, D.I. Finkelstein, P.A. Doble, High-resolution elemental bioimaging of Ca, Mn, Fe, Co, Cu, and Zn employing LA-ICP-MS and hydrogen reaction gas, Anal. Chem. 84 (2012) 6707–6714. https://doi.org/10.1021/ac301156f.

[81] S.D. Tanner, V.I. Baranov, D.R. Bandura, Reaction cells and collision cells for ICP-MS: a tutorial review, Spectrochim. Acta Part B At. Spectrosc. 57 (2002) 1361–1452. https://doi.org/https://doi.org/10.1016/S0584-8547(02)00069-1.

[82] C.D.B. Amaral, R.C. Machado, A. Virgilio, D. Schiavo, A.R.A. Nogueira, J.A. Nóbrega, Critical evaluation of internal standardization in ICP tandem mass spectrometry and feasibility of the oxygen reaction for boron determination in plants, J. Anal. At. Spectrom. 31 (2016) 1179–1184. https://doi.org/10.1039/c6ja00133e.

[83] D.P. Bishop, N. Cole, T. Zhang, P.A. Doble, D.J. Hare, A guide to integrating immunohistochemistry and chemical imaging, Chem. Soc. Rev. 47 (2018) 3770–3787. https://doi.org/10.1039/c7cs00610a.

[84] A.H. Coons, H.J. Creech, R.N. Jones, Immunological Properties of an Antibody Containing a Fluorescent Group, Proc. Soc. Exp. Biol. Med. 47 (1941) 200–202. https://doi.org/10.3181/00379727-47-13084P.

[85] J.A. Ramos-Vara, M.A. Miller, When Tissue Antigens and Antibodies Get Along: Revisiting the Technical Aspects of Immunohistochemistry-The Red, Brown, and Blue Technique, Vet. Pathol. 51 (2014) 42–87. https://doi.org/10.1177/0300985813505879.

[86] R.M. Levenson, A.D. Borowsky, M. Angelo, Immunohistochemistry and mass spectrometry for highly multiplexed cellular molecular imaging, Lab. Investig. 95 (2015) 397–405. https://doi.org/10.1038/labinvest.2015.2.

[87] C. Giesen, H.A.O. Wang, D. Schapiro, N. Zivanovic, A. Jacobs, B. Hattendorf, P.J. Schüffler, D. Grolimund, J.M. Buhmann, S. Brandt, Z. Varga, P.J. Wild, D. Günther, B. Bodenmiller, Highly multiplexed imaging of tumor tissues with subcellular resolution by mass cytometry, Nat. Methods. 11 (2014) 417–422. https://doi.org/10.1038/nmeth.2869.

[88] D.J. Hare, P. Lei, S. Ayton, B.R. Roberts, R. Grimm, J.L. George, D.P. Bishop, A.D. Beavis, S.J. Donovan, G. McColl, I. Volitakis, C.L. Masters, P.A. Adlard, R.A. Cherny, A.I. Bush, D.I. Finkelstein, P.A. Doble, An iron-dopamine index predicts risk of parkinsonian neurodegeneration in the substantia nigra pars compacta, Chem. Sci. 5 (2014) 2160–2169.

https://doi.org/10.1039/c3sc53461h.

[89] B. Paul, D.J. Hare, D.P. Bishop, C. Paton, V.T. Nguyen, N. Cole, M.M. Niedwiecki, E. Andreozzi, A. Vais, J.L. Billings, L. Bray, A.I. Bush, G. McColl, B.R. Roberts, P.A. Adlard, D.I. Finkelstein, J. Hellstrom, J.M. Hergt, J.D. Woodhead, P.A. Doble, Visualising mouse neuroanatomy and function by metal distribution using laser ablation-inductively coupled plasma-mass spectrometry imaging, Chem. Sci. 6 (2015) 5383–5393. https://doi.org/10.1039/C5SC02231B.

[90] D.J. Rowan, K.K. Mangalaparthi, S. Singh, R.K. Moreira, T. Mounajjed, L. Lamps, M. Westerhoff, J. Cheng, A.M. Bellizzi, D.S. Allende, A. Pandey, R.P. Graham, Metallothionein immunohistochemistry has high sensitivity and specificity for detection of Wilson disease, Mod. Pathol. (2021) 1–10. https://doi.org/10.1038/s41379-021-01001-7.

[91] R. González de Vega, D. Clases, M.L. Fernández-Sánchez, N. Eiró, L.O. González, F.J. Vizoso, P.A. Doble, A. Sanz-Medel, MMP-11 as a biomarker for metastatic breast cancer by immunohistochemical-assisted imaging mass spectrometry, Anal. Bioanal. Chem. 411 (2019) 639–646. https://doi.org/10.1007/s00216-018-1365-3.

[92] C. Giesen, L. Waentig, U. Panne, N. Jakubowski, History of inductively coupled plasma mass spectrometry-based immunoassays, Spectrochim. Acta - Part B At. Spectrosc. 76 (2012) 27–39. https://doi.org/10.1016/j.sab.2012.06.009.

[93] M. Tvrdonova, M. Vlcnovska, L.P. Vanickova, V. Kanicky, V. Adam, L. Ascher, N. Jakubowski, M. Vaculovicova, T. Vaculovic, Gold nanoparticles as labels for immunochemical analysis using laser ablation inductively coupled plasma mass spectrometry, Anal. Bioanal. Chem. 411 (2019) 559–564. https://doi.org/10.1007/s00216-018-1300-7.

[94] A. Tiselius, A new apparatus for electrophoretic analysis of colloidal mixtures, Trans. Faraday Soc. 33 (1937) 524–531. https://doi.org/10.1039/tf9373300524.

[95] A. Tiselius, The Moving Boundary Method of Studying the Electrophoresis of Proteins, Nov. Acta Regiae Soc. Sci. Uppsala, Ser. 4. (1930) 1–107.

[96] S. Hjertén, Free zone electrophoresis, Chromatogr. Rev. 9 (1967) 122–219. https://doi.org/10.1016/0009-5907(67)80003-6.

[97] K.D. Lukacs, J.W. Jorgenson, Capillary zone electrophoresis: Effect of physical parameters on separation efficiency and quantitation, J. High Resolut. Chromatogr. 8 (1985) 407–411. https://doi.org/10.1002/jhrc.1240080810.

[98] Y. Lu, N. Yeung, N. Sieracki, N.M. Marshall, Design of functional metalloproteins, Nature. 460 (2009) 855–862. https://doi.org/10.1038/nature08304.

[99] R.F.S. Lee, L. Menin, L. Patiny, D. Ortiz, P.J. Dyson, Versatile Tool for the Analysis of Metal − Protein Interactions Reveals the Promiscuity of Metallodrug − Protein Interactions, (2017) 11985–11989. https://doi.org/10.1021/acs.analchem.7b02211.

[100] P.B. Tchounwou, C.G. Yedjou, A.K. Patlolla, D.J. Sutton, Molecular, clinical and environmental toxicicology Volume 3: Environmental Toxicology, 2012. https://doi.org/10.1007/978-3-7643-8340-4.

[101] H. Cheng, P. Li, J. Liu, M. Ye, Coupling electrophoretic separation with inductively coupled plasma spectroscopic detection: Interfaces and applications from elemental speciation, metal-ligand interaction to indirect determination, J. Anal. At. Spectrom. 31 (2016) 1780–1810. https://doi.org/10.1039/c6ja00206d.

[102] D. Pröfrock, A. Prange, Inductively Coupled Plasma–Mass Spectrometry (ICP-MS) for Quantitative Analysis in Environmental and Life Sciences: A Review of Challenges, Solutions, and Trends, Appl. Spectrosc. 66 (2012) 843–868. https://doi.org/10.1366/12-06681.

[103] D.P. Bishop, D.J. Hare, D. Clases, P.A. Doble, Applications of liquid chromatography-inductively coupled plasma-mass spectrometry in the biosciences: A tutorial review and recent developments, TrAC - Trends Anal. Chem. 104 (2018) 11–21. https://doi.org/10.1016/J.TRAC.2017.09.017.

[104] A.L. Rosen, G.M. Hieftje, Inductively coupled plasma mass spectrometry and electrospray mass spectrometry for speciation analysis: Applications and instrumentation, Spectrochim. Acta - Part B At. Spectrosc. 59 (2004) 135–146. https://doi.org/10.1016/j.sab.2003.09.004.

[105] L. Ruzik, P. Kwiatkowski, Application of CE-ICP-MS and CE-ESI-MS/MS for identification of Zn-binding ligands in Goji berries extracts, Talanta. 183 (2018) 102–107. https://doi.org/10.1016/j.talanta.2018.02.040.

[106] H.U. Holtkamp, S.J. Morrow, M. Kubanik, C.G. Hartinger, A.H.U. Holtkamp, S.J. Morrow, C.G. Hartinger, H.U. Holtkamp, S.J. Morrow, M. Kubanik, C.G. Hartinger, Hyphenation of capillary electrophoresis to inductively coupled plasma mass spectrometry with a modified coaxial sheath-flow interface, J. Chromatogr. A. 1561 (2018) 76–82. https://doi.org/10.1016/j.chroma.2018.05.036.

[107] A. Prange, D. Schaumlöffel, Determination of element species at trace levels using capillary electrophoresis-inductively coupled plasma sector

field mass spectrometry, J. Anal. At. Spectrom. 14 (1999) 1329–1332. https://doi.org/10.1039/a901749f.

[108] J.W. Olesik, J.A. Kinzer, S. V Olesik, Capillary Electrophoresis Inductively Coupled Plasma Spectrometry for Rapid Elemental Speciation, Anal. Chem. 67 (1995) 1–12. https://doi.org/10.1021/ac00097a003.

[109] Y.Y. Chan, W.T. Chan, Interface for capillary electrophoresis coupled with inductively coupled plasma atomic emission spectrometry, J. Chromatogr. A. 853 (1999) 141–149. https://doi.org/10.1016/S0021-9673(99)00713-X.

[110] B. Deng, W.T. Chan, Simple interface for capillary electrophoresis-inductively coupled plasma atomic emission spectrometry, J. Chromatogr. A. 891 (2000) 139–148. https://doi.org/10.1016/S0021-9673(00)00622-1.

[111] K.L. Sutton, C. B'Hymer, J.A. Caruso, Ultraviolet absorbance and inductively coupled plasma mass spectrometric detection for capillary electrophoresis - A comparison of detection modes and interface designs, J. Anal. At. Spectrom. 13 (1998) 885–891. https://doi.org/10.1039/a801869c.

[112] G. Di Yang, X.Q. Xu, W. Wang, L.J. Xu, G.N. Chen, F.F. Fu, A new interface used to couple capillary electrophoresis with an inductively coupled plasma mass spectrometry for speciation analysis, Electrophoresis. 29 (2008) 2862–2868. https://doi.org/10.1002/elps.200700849.

[113] G. Di Yang, J.H. Xu, J.P. Zheng, X.Q. Xu, W. Wang, L.J. Xu, G.N. Chen, F.F. Fu, Speciation analysis of arsenic in Mya arenaria Linnaeus and Shrimp with capillary electrophoresis-inductively coupled plasma mass spectrometry, Talanta. 78 (2009) 471–476. https://doi.org/10.1016/j.talanta.2008.11.040.

[114] Y. Li, S.K. Sun, J.L. Yang, Y. Jiang, Label-free DNA hybridization detection and single base-mismatch discrimination using CE-ICP-MS assay, Analyst. 136 (2011) 5038–5045. https://doi.org/10.1039/c1an15592j.

[115] E. Mei, Interface for coupling capillary electrophoresis to inductively coupled plasma and on-column concentration technique, Anal. Chem. 69 (1997) 2187–2192. https://doi.org/10.1021/ac960950w.

[116] Y. Li, J.M. Liu, F. Han, Y. Jiang, X.P. Yan, Probing interactions of antimony species with DNA by short column capillary electrophoresis coupled with inductively coupled plasma mass spectrometry, J. Anal. At. Spectrom. 26 (2011) 94–99. https://doi.org/10.1039/c0ja00079e.

[117] V. Majidi, N.J. Miller-Ihli, Two simple interface designs for capillary electrophoresis-inductively coupled plasma mass spectrometry, Analyst. 123 (1998) 803–808. https://doi.org/10.1039/a707770j.

[118] H. Cheng, J. Liu, X. Yin, H. Shen, Z. Xu, Elimination of suction effect in interfacing microchip electrophoresis with inductively coupled plasma mass spectrometry using porous monolithic plugs, Analyst. 137 (2012) 3111–3118. https://doi.org/10.1039/c2an35050e.

[119] H. Cheng, C. Han, Z. Xu, J. Liu, Y. Wang, Sensitivity Enhancement by Field-Amplified Sample Injection in Interfacing Microchip Electrophoresis with Inductively Coupled Plasma Mass Spectrometry for Bromine Speciation in Bread, Food Anal. Methods. 7 (2014) 2153–2162. https://doi.org/10.1007/s12161-014-9848-0.

[120] J.A. Kinzer, J.W. Olesik, S. V. Olesik, Effect of Laminar Flow in Capillary Electrophoresis: Model and Experimental Results on Controlling Analysis Time and Resolution with Inductively Coupled Plasma Spectrometry Detection, Anal. Chem. 68 (1996) 3250–3257. https://doi.org/10.1021/ac951143k.

[121] Q. Lu, S.M. Bird, R.M. Barnes, Interface for Capillary Electrophoresis and Inductively Coupled Plasma Mass Spectrometry, Anal. Chem. 67 (1995) 2949–2956. https://doi.org/10.1021/ac00113a033.

[122] T.T.T.N. Nguyen, J. Østergaard, S. Stürup, B. Gammelgaard, Investigation of a liposomal oxaliplatin drug formulation by capillary electrophoresis hyphenated to inductively coupled plasma mass spectrometry (CE-ICP-MS), Anal. Bioanal. Chem. 402 (2012) 2131–2139. https://doi.org/10.1007/s00216-011-5651-6.

[123] T.T.T.N. Nguyen, J. Østergaard, S. Stürup, B. Gammelgaard, Metallomics in drug development: Characterization of a liposomal cisplatin drug formulation in human plasma by CE-ICP-MS, Anal. Bioanal. Chem. 405 (2013) 1845–1854. https://doi.org/10.1007/s00216-012-6355-2.

[124] B. Meermann, M. Bartel, A. Scheffer, S. Trümpler, U. Karst, Capillary electrophoresis with inductively coupled plasma-mass spectrometric and electrospray time of flight mass spectrometric detection for the determination of arsenic species in fish samples, Electrophoresis. 29 (2008) 2731–2737. https://doi.org/10.1002/elps.200700902.

[125] P.W. Kirlew, M.T.M. Castillano, J.A. Caruso, Evaluation of ultrasonic nebulizers as interfaces for capillary electrophoresis of inorganic anions and cations with inductively coupled plasma mass spectrometric detection, Spectrochim. Acta, Part B At. Spectrosc. 53 (1998) 221–237. https://doi.org/10.1016/S0584-8547(98)00079-2.

[126] J. Li, T. Umemura, T. Odake, K.I. Tsunoda, A high-efficiency cross-flow micronebulizer interface for capillary electrophoresis and inductively coupled plasma mass spectrometry, Anal. Chem. 73 (2001) 5992–5999. https://doi.org/10.1021/ac010595w.

[127] N. Kovachev, M.Á. Aguirre, M. Hidalgo, K. Simitchiev, V. Stefanova, V. Kmetov, A. Canals, Elemental speciation by capillary electrophoresis with inductively coupled plasma spectrometry: A new approach by Flow Focusing® nebulization, Microchem. J. 117 (2014) 27–33. https://doi.org/10.1016/j.microc.2014.06.005.

[128] X. Men, C. Wu, X. Zhang, X. Wei, M.L. Chen, T. Yang, J.H. Wang, Intracellular silver speciation by coupling capillary electrophoresis to ICP-MS integrating a high performance spiral flow spray chamber, Anal. Chim. Acta. 1166 (2021) 338540. https://doi.org/10.1016/j.aca.2021.338540.

[129] D. Zhou, Y. Lin, H. Long, Y. Xu, B. Wang, L. Xian, C. Xia, X. Hou, C. Zheng, Simultaneous total and speciation analysis of rhenium by capillary electrophoresis-inductively coupled plasma mass spectrometry, Spectrochim. Acta - Part B At. Spectrosc. 180 (2021) 106211. https://doi.org/10.1016/j.sab.2021.106211.

[130] A. Týčová, V. Ledvina, K. Klepárník, Recent advances in CE-MS coupling: Instrumentation, methodology, and applications, Electrophoresis. 38 (2017) 115–134. https://doi.org/10.1002/elps.201600366.

[131] J.E. Sonke, V.J.M. Salters, Capillary electrophoresis-high resolution sector field inductively coupled plasma mass spectrometry, J. Chromatogr. A. 1159 (2007) 63–74. https://doi.org/10.1016/j.chroma.2007.05.055.

[132] B. Michalke, Capillary electrophoresis-inductively coupled plasma-mass spectrometry: A report on technical principles and problem solutions, potential, and limitations of this technology as well as on examples of application, Electrophoresis. 26 (2005) 1584–1597. https://doi.org/10.1002/elps.200410314.

[133] A. Prange, D. Pröfrock, Application of CE-ICP-MS and CE-ESI-MS in metalloproteomics: Challenges, developments, and limitations, Anal. Bioanal. Chem. 383 (2005) 372–389. https://doi.org/10.1007/s00216-005-3420-0.

[134] S.S. Kannamkumarath, K. Wrobel, K. Wrobel, C. B'Hymer, J.A. Caruso, Capillary electrophoresis-inductively coupled plasma-mass spectrometry: An attractive complementary technique for elemental speciation analysis, J. Chromatogr. A. 975 (2002) 245–266. https://doi.org/10.1016/S0021-9673(02)01218-9.

[135] C. Duroux, A. Hagège, Interactions between copper (II) and β-amyloid peptide using capillary electrophoresis–ICP–MS: Kd measurements at the nanogram scale, Anal. Bioanal. Chem. (2021). https://doi.org/10.1007/s00216-021-03769-8.

[136] P. Švecová, D. Baron, K.A. Schug, T. Pluháček, J. Petr, Ultra-trace

determination of oxaliplatin impurities by sweeping-MEKC-ICP-MS, Microchem. J. 172 (2022). https://doi.org/10.1016/j.microc.2021.106967.

[137] T.T.T.N. Nguyen, J. Østergaard, B. Gammelgaard, A method for studies on interactions between a gold-based drug and plasma proteins based on capillary electrophoresis with inductively coupled plasma mass spectrometry detection, Anal. Bioanal. Chem. 407 (2015) 8497–8503. https://doi.org/10.1007/s00216-015-8997-3.

[138] L. Labied, P. Rocchi, T. Doussineau, J. Randon, O. Tillement, H. Cottet, F. Lux, A. Hagège, Biodegradation of metal-based ultra-small nanoparticles: A combined approach using TDA-ICP-MS and CE-ICP-MS, Anal. Chim. Acta. 1185 (2021). https://doi.org/10.1016/j.aca.2021.339081.

[139] Z. Zhang, E.H. Peuchen, N.J. Dovichi, Surface-Confined Aqueous Reversible Addition-Fragmentation Chain Transfer (SCARAFT) Polymerization Method for Preparation of Coated Capillary Leads to over 10 000 Peptides Identified from 25 ng HeLa Digest by Using Capillary Zone Electrophoresis-Tandem Ma, Anal. Chem. 89 (2017) 6774–6780. https://doi.org/10.1021/acs.analchem.7b01147.

[140] C. Huhn, R. Ramautar, M. Wuhrer, G.W. Somsen, Relevance and use of capillary coatings in capillary electrophoresis-mass spectrometry, Anal. Bioanal. Chem. 396 (2010) 297–314. https://doi.org/10.1007/s00216-009-3193-y.

[141] A. Staub, S. Comte, S. Rudaz, J.L. Veuthey, J. Schappler, Use of organic solvent to prevent protein adsorption in CE-MS experiments, Electrophoresis. 31 (2010) 3326–3333. https://doi.org/10.1002/elps.201000245.

[142] A.L. Marie, E. Dominguez-Vega, F. Saller, J.L. Plantier, R. Urbain, D. Borgel, N.T. Tran, G.W. Somsen, M. Taverna, Characterization of conformers and dimers of antithrombin by capillary electrophoresis-quadrupole-time-of-flight mass spectrometry, Anal. Chim. Acta. 947 (2016) 58–65. https://doi.org/10.1016/j.aca.2016.10.016.

[143] S. Hjertén, High-performance electrophoresis, J. Chromatogr. A. 347 (1985) 191–198. https://doi.org/10.1016/S0021-9673(01)95485-8.

[144] X. Han, Y. Wang, A. Aslanian, B. Fonslow, B. Graczyk, T.N. Davis, J.R. Yates, In-line separation by capillary electrophoresis prior to analysis by top-down mass spectrometry enables sensitive characterization of protein complexes, J. Proteome Res. 13 (2014) 6078–6086. https://doi.org/10.1021/pr500971h.

[145] C. Berardet, J. Kaffy, S. Ongeri, M. Taverna, A capillary zone electrophoresis method to investigate the oligomerization of the human

Islet Amyloid Polypeptide involved in Type 2 Diabetes, J. Chromatogr. A. 1578 (2018) 83–90. https://doi.org/10.1016/j.chroma.2018.10.006.

[146] Y. Li, P.D. Compton, J.C. Tran, I. Ntai, N.L. Kelleher, Optimizing capillary electrophoresis for top-down proteomics of 30-80 kDa proteins, Proteomics. 14 (2014) 1158–1164. https://doi.org/10.1002/pmic.201300381.

[147] A. Stolz, Y. Hedeland, L. Salzer, J. Römer, R. Heiene, L. Leclercq, H. Cottet, J. Bergquist, C. Neusüß, Capillary Zone Electrophoresis-Top-Down Tandem Mass Spectrometry for In-Depth Characterization of Hemoglobin Proteoforms in Clinical and Veterinary Samples, Anal. Chem. 92 (2020) 10531–10539. https://doi.org/10.1021/acs.analchem.0c01350.

[148] E. Dominguez-Vega, T. De Vijlder, E.P. Romijn, G.W. Somsen, Capillary electrophoresis-tandem mass spectrometry as a highly selective tool for the compositional and site-specific assessment of multiple peptide-deamidation, Anal. Chim. Acta. 982 (2017) 122–130. https://doi.org/10.1016/j.aca.2017.06.021.

[149] J.R. Catai, J. Sastre Toraño, P.M.J.M. Jongen, G.J. de Jong, G.W. Somsen, Analysis of recombinant human growth hormone by capillary electrophoresis with bilayer-coated capillaries using UV and MS detection, J. Chromatogr. B Anal. Technol. Biomed. Life Sci. 852 (2007) 160–166. https://doi.org/10.1016/j.jchromb.2007.01.007.

[150] J. Horvath, V. Dolník, Polymer wall coatings for capillary electrophoresis, Electrophoresis. 22 (2001) 644–655. https://doi.org/10.1002/1522-2683(200102)22:4<644::AID-ELPS644>3.0.CO;2-3.

[151] T. Soga, Y. Inoue, G.A. Ross, Analysis of halides, oxyhalides and metal oxoacids by capillary electrophoresis with suppressed electroosmotic flow, J. Chromatogr. A. 718 (1995) 421–428. https://doi.org/10.1016/0021-9673(95)00704-0.

[152] G.W. Tindall, R.L. Perry, Separation of fast anions by capillary electrophoresis without flow reversal, J. Chromatogr. A. 696 (1995) 349–352. https://doi.org/10.1016/0021-9673(94)01229-8.

[153] T. Soga, Y. Ueno, H. Naraoka, K. Matsuda, M. Tomita, T. Nishioka, Pressure-assisted capillary electrophoresis electrospray ionization mass spectrometry for analysis of multivalent anions, Anal. Chem. 74 (2002) 6224–6229. https://doi.org/10.1021/ac0202684.

[154] E. Katsivela, M.G. Höfle, Low-molecular-mass RNA fingerprinting of bacteria by capillary electrophoresis using entangled polymer solutions, J. Chromatogr. A. 717 (1995) 91–103. https://doi.org/10.1016/0021-9673(95)00628-5.

[155] J.H. Lee, O.K. Choi, H.S. Jung, K.R. Kim, D.S. Chung, Capillary electrophoresis of nonprotein and protein amino acids without derivatization, Electrophoresis. 21 (2000) 930–934. https://doi.org/10.1002/(SICI)1522-2683(20000301)21:5<930::AID-ELPS930>3.0.CO;2-8.

[156] T. Soga, Y. Ohashi, Y. Ueno, H. Naraoka, M. Tomita, T. Nishioka, Quantitative Metabolome Analysis Using Capillary Electrophoresis Mass Spectrometry, J. Proteome Res. 2 (2003) 488–494. https://doi.org/10.1021/pr034020m.

[157] M. Kinoshita, E. Murakami, Y. Oda, T. Funakubo, D. Kawakami, K. Kakehi, N. Kawasaki, K. Morimoto, T. Hayakawa, Comparative studies on the analysis of glycosylation heterogeneity of sialic acid-containing glycoproteins using capillary electrophoresis, J. Chromatogr. A. 866 (2000) 261–271. https://doi.org/10.1016/S0021-9673(99)01080-8.

[158] L. Balcaen, G. Woods, M. Resano, F. Vanhaecke, Accurate determination of S in organic matrices using isotope dilution ICP-MS/MS, J. Anal. At. Spectrom. 28 (2013) 33–39. https://doi.org/10.1039/C2JA30265A.

[159] L. Balcaen, E. Bolea-Fernandez, M. Resano, F. Vanhaecke, Inductively coupled plasma - Tandem mass spectrometry (ICP-MS/MS): A powerful and universal tool for the interference-free determination of (ultra)trace elements - A tutorial review, Anal. Chim. Acta. 894 (2015) 7–19. https://doi.org/10.1016/j.aca.2015.08.053.

[160] D.P. Bishop, D.J. Hare, F. Fryer, R. V. Taudte, B.R. Cardoso, N. Cole, P.A. Doble, Determination of selenium in serum in the presence of gadolinium with ICP-QQQ-MS, Analyst. 140 (2015) 2842–2846. https://doi.org/10.1039/c4an02283a.

[161] Y. Anan, Y. Hatakeyama, M. Tokumoto, Y. Ogra, Chromatographic behavior of selenoproteins in rat serum detected by inductively coupled plasma mass spectrometry, Anal. Sci. 29 (2013) 787–192. https://doi.org/10.2116/analsci.29.787.

[162] S.D. Fernández, N. Sugishama, J.R. Encinar, A. Sanz-Medel, Triple quad ICPMS (ICPQQQ) as a new tool for absolute quantitative proteomics and phosphoproteomics, Anal. Chem. 84 (2012) 5851–5857. https://doi.org/10.1021/ac3009516.

[163] M. Tanimizu, N. Sugiyama, E. Ponzevera, G. Bayon, Determination of ultra-low 236U/238U isotope ratios by tandem quadrupole ICP-MS/MS, J. Anal. At. Spectrom. 28 (2013) 1372–1376. https://doi.org/10.1039/c3ja50145k.

[164] L. Balcaen, E. Bolea-Fernandez, M. Resano, F. Vanhaecke, Accurate determination of ultra-trace levels of Ti in blood serum using ICP-MS/MS,

Anal. Chim. Acta. 809 (2014) 1–8. https://doi.org/10.1016/j.aca.2013.10.017.

[165] J. Zheng, W. Bu, K. Tagami, Y. Shikamori, K. Nakano, S. Uchida, N. Ishii, Determination of 135Cs and 135Cs/137Cs Atomic Ratio in Environmental Samples by Combining Ammonium Molybdophosphate (AMP)-Selective Cs Adsorption and Ion-Exchange Chromatographic Separation to Triple-Quadrupole Inductively Coupled Plasma–Mass Spectrom, Anal. Chem. 86 (2014) 7103–7110. https://doi.org/10.1021/ac501712m.

[166] S. Meyer, R.G. De Vega, X. Xu, Z. Du, P.A. Doble, D. Clases, Characterization of Upconversion Nanoparticles by Single-Particle ICP-MS Employing a Quadrupole Mass Filter with Increased Bandpass, Anal. Chem. 92 (2020) 15007–15016. https://doi.org/10.1021/acs.analchem.0c02925.

[167] R. Pedder, Practical quadrupole theory: graphical theory, Extrel Appl. Note RA_2010A. (2001) 1–5. http://www.ardaratech.com/document-library/technical-notes/5-ra-2010a-practical-quadrupole-theory-graphical-theory.

[168] D. Clases, R. Gonzalez De Vega, S. Funke, T.E. Lockwood, M.T. Westerhausen, R.V. Taudte, P.A. Adlard, P.A. Doble, Matching sensitivity to abundance: High resolution immuno-mass spectrometry imaging of lanthanide labels and endogenous elements in the murine brain, J. Anal. At. Spectrom. 35 (2020) 728–735. https://doi.org/10.1039/c9ja00405j.

[169] M. Horstmann, R. Gonzalez De Vega, D.P. Bishop, U. Karst, P.A. Doble, D. Clases, Determination of gadolinium MRI contrast agents in fresh and oceanic waters of Australia employing micro-solid phase extraction, HILIC-ICP-MS and bandpass mass filtering, J. Anal. At. Spectrom. 36 (2021) 767–775. https://doi.org/10.1039/d0ja00493f.

[170] I. Strenge, C. Engelhard, Single particle inductively coupled plasma mass spectrometry: Investigating nonlinear response observed in pulse counting mode and extending the linear dynamic range by compensating for dead time related count losses on a microsecond timescale, J. Anal. At. Spectrom. 35 (2020) 84–99. https://doi.org/10.1039/C9JA00327D.

[171] R. Álvarez-Fernández García, M. Corte-Rodríguez, M. Macke, K.L. Leblanc, Z. Mester, M. Montes-Bayón, J. Bettmer, Addressing the presence of biogenic selenium nanoparticles in yeast cells: Analytical strategies based on ICP-TQ-MS, Analyst. 145 (2020) 1457–1465. https://doi.org/10.1039/C9AN01565E.

[172] B. Meermann, F. Laborda, Analysis of nanomaterials by field-flow fractionation and single particle ICP-MS, J. Anal. At. Spectrom. 30 (2015) 1226–1228. https://doi.org/10.1039/C5JA90019K.

[173] B. Franze, I. Strenge, C. Engelhard, Separation and detection of gold nanoparticles with capillary electrophoresis and ICP-MS in single particle mode (CE-SP-ICP-MS), J. Anal. At. Spectrom. 32 (2017) 1481–1489. https://doi.org/10.1039/C7JA00040E.

[174] C. Degueldre, P.Y. Favarger, Colloid analysis by single particle inductively coupled plasma-mass spectroscopy: A feasibility study, Colloids Surfaces A Physicochem. Eng. Asp. 217 (2003) 137–142. https://doi.org/10.1016/S0927-7757(02)00568-X.

[175] D. Mozhayeva, C. Engelhard, A critical review of single particle inductively coupled plasma mass spectrometry-A step towards an ideal method for nanomaterial characterization, J. Anal. At. Spectrom. 35 (2020) 1740–1783. https://doi.org/10.1039/C9JA00206E.

[176] K. Flores, R.S. Turley, C. Valdes, Y. Ye, J. Cantu, J.A. Hernandez-Viezcas, J.G. Parsons, J.L. Gardea-Torresdey, Environmental applications and recent innovations in single particle inductively coupled plasma mass spectrometry (SP-ICP-MS), Appl. Spectrosc. Rev. 56 (2021) 1–26. https://doi.org/10.1080/05704928.2019.1694937.

[177] M.D. Montaño, J.W. Olesik, A.G. Barber, K. Challis, J.F. Ranville, Single Particle ICP-MS: Advances toward routine analysis of nanomaterials, Anal. Bioanal. Chem. 408 (2016) 5053–5074. https://doi.org/10.1007/S00216-016-9676-8.

[178] F. Laborda, E. Bolea, J. Jiménez-Lamana, Single Particle Inductively Coupled Plasma Mass Spectrometry: A Powerful Tool for Nanoanalysis, Anal. Chem. 86 (2014) 2270–2278. https://doi.org/10.1021/ac402980q.

[179] E. Bolea, M.S. Jimenez, J. Perez-Arantegui, J.C. Vidal, M. Bakir, K. Ben-Jeddou, A.C. Gimenez-Ingalaturre, D. Ojeda, C. Trujillo, F. Laborda, Analytical applications of single particle inductively coupled plasma mass spectrometry: A comprehensive and critical review, Anal. Methods. 13 (2021) 2742–2795. https://doi.org/10.1039/D1AY00761K.

[180] J.A. Tainer, V.A. Roberts, E.D. Getzoff, Protein metal-binding sites, Curr. Opin. Biotechnol. 3 (1992) 378–387. https://doi.org/10.1016/0958-1669(92)90166-G.

[181] C.E. Outten, T. V. O'Halloran, Femtomolar sensitivity of metalloregulatory proteins controlling zinc homeostasis, Science (80-.). 292 (2001) 2488–2492. https://doi.org/10.1126/science.1060331.

[182] Y. Zhang, B.R. Fonslow, B. Shan, M.-C. Baek, J.R. Yates, Protein Analysis by Shotgun/Bottom-up Proteomics, Chem. Rev. 113 (2013) 2343–2394. https://doi.org/10.1021/cr3003533.

[183] I. Rodriguez, S.F.Y. Li, Surface deactivation in protein and peptide analysis by capillary electrophoresis, Anal. Chim. Acta. 383 (1999) 1–26. https://doi.org/10.1016/S0003-2670(98)00485-1.

[184] M. Rabe, D. Verdes, S. Seeger, Understanding protein adsorption phenomena at solid surfaces, Adv. Colloid Interface Sci. 162 (2011) 87–106. https://doi.org/10.1016/j.cis.2010.12.007.

[185] B.P. Salmanowicz, Capillary electrophoresis of seed albumins from Vicia species using uncoated and surface-modified fused silica capillaries, Chromatographia. 41 (1995) 99–106. https://doi.org/10.1007/BF02688007.

[186] H. Lindner, W. Helliger, B. Sarg, C. Meraner, Effect of buffer composition on the migration order and separation of histone H1 subtypes, Electrophoresis. 16 (1995) 604–610. https://doi.org/10.1002/elps.1150160197.

[187] F. Bedia Erim, Effect of cationic polymer on the separation of phenols by capillary electrophoresis, J. Chromatogr. A. 768 (1997) 161–167. https://doi.org/10.1016/S0021-9673(96)01063-1.

[188] H. Katayama, Y. Ishihama, N. Asakawa, Stable cationic capillary coating with successive multiple ionic polymer layers for capillary electrophoresis, Anal. Chem. 70 (1998) 5272–5277. https://doi.org/10.1021/ac980522l.

[189] C. Stathakis, E.A. Arriaga, D.F. Lewis, N.J. Dovichi, Cationic and anionic polymeric additives for wall deactivation and selectivity control in the capillary electrophoretic separation of proteins in food samples, J. Chromatogr. A. 817 (1998) 227–232. https://doi.org/10.1016/S0021-9673(98)00371-9.

[190] C.A. Lucy, A.M. MacDonald, M.D. Gulcev, Non-covalent capillary coatings for protein separations in capillary electrophoresis, J. Chromatogr. A. 1184 (2008) 81–105. https://doi.org/10.1016/j.chroma.2007.10.114.

[191] C. Berardet, J. Kaffy, S. Ongeri, M. Taverna, A capillary zone electrophoresis method to investigate the oligomerization of the human Islet Amyloid Polypeptide involved in Type 2 Diabetes, J. Chromatogr. A. 1578 (2018) 83–90. https://doi.org/10.1016/j.chroma.2018.10.006.

[192] A. Marie, E. Dominguez-vega, F. Saller, J. Plantier, D. Borgel, N.T. Tran, G.W. Somsen, Analytica Chimica Acta Characterization of conformers and dimers of antithrombin by capillary electrophoresis-quadrupole-time-of- fl ight mass spectrometry, Anal. Chim. Acta J. 947 (2016) 58–65. https://doi.org/10.1016/j.aca.2016.10.016.

[193] S.H. Kang, J.W. Kim, D.S. Chung, Determination of homocysteine and other thiols in human plasma by capillary electrophoresis, J. Pharm.

Biomed. Anal. 15 (1997) 1435–1441. https://doi.org/10.1016/S0731-7085(96)02051-1.

[194] M. Dizy, L.F. Bisson, White wine protein analysis by capillary zone electrophoresis, Am. J. Enol. Vitic. 50 (1999) 120–127.

[195] S. Kamoda, C. Nomura, M. Kinoshita, S. Nishiura, R. Ishikawa, K. Kakehi, N. Kawasaki, T. Hayakawa, Profiling analysis of oligosaccharides in antibody pharmaceuticals by capillary electrophoresis, J. Chromatogr. A. 1050 (2004) 211–216. https://doi.org/10.1016/j.chroma.2004.08.049.

[196] D. Heiger, High performance capillary electrophoresis, Agilent Technologies, 2000. http://www.colby.edu/chemistry/CH332/laboratory/Agilent CE Primer.pdf.

[197] X. Shen, Z. Yang, E.N. McCool, R.A. Lubeckyj, D. Chen, L. Sun, Capillary zone electrophoresis-mass spectrometry for top-down proteomics, TrAC Trends Anal. Chem. 120 (2019) 115644. https://doi.org/10.1016/j.trac.2019.115644.

[198] H.M. Mcnair, J.M. Miller, Basic Gas Chromatography, John Wiley & Sons, Inc., New York, 1967.

[199] A.S. Pérez, F.L. Conde, J.H. Méndez, Polarographic determination of phenylalanine, tyrosine, methionine, glutamic acid and histidine with a dropping copper amalgam electrode, J. Electroanal. Chem. Interfacial Electrochem. 74 (1976) 339–346. https://doi.org/10.1016/S0022-0728(76)80117-9.

[200] T. Marquardt, J. Denecke, Congenital disorders of glycosylation: Review of their molecular bases, clinical presentations and specific therapies, Eur. J. Pediatr. 162 (2003) 359–379. https://doi.org/10.1007/s00431-002-1136-0.

[201] T. Barz, V. Löffler, H. Arellano-Garcia, G. Wozny, Optimal determination of steric mass action model parameters for β-lactoglobulin using static batch experiments, J. Chromatogr. A. 1217 (2010) 4267–4277. https://doi.org/10.1016/j.chroma.2010.04.001.

[202] J. Zaia, R.S. Annan, K. Biemann, The correct molecular weight of myoglobin, a common calibrant for mass spectrometry, Rapid Commun. Mass Spectrom. 6 (1992) 32–36. https://doi.org/10.1002/rcm.1290060108.

[203] M. Graf, R. Galera García, H. Wätzig, Protein adsorption in fused-silica and polyacrylamide-coated capillaries, Electrophoresis. 26 (2005) 2409–2417. https://doi.org/10.1002/elps.200410360.

[204] Z. Xia, E.R. Williams, Protein-Glass Surface Interactions and Ion Desalting in Electrospray Ionization with Submicron Emitters, J. Am. Soc. Mass Spectrom. 29 (2018) 194–202. https://doi.org/10.1007/s13361-017-1825-6.

[205] I.M. Vlasova, A.M. Saletsky, Study of the denaturation of human serum albumin by sodium dodecyl sulfate using the intrinsic fluorescence of albumin, J. Appl. Spectrosc. 76 (2009) 536–541. https://doi.org/10.1007/s10812-009-9227-6.

[206] B.T. Bruno Giometto, Paolo Gallo, 7 - Transferrin Receptors in the Central Nervous System, Methods Neurosci. 11 (1993) 122–134. https://doi.org/https://doi.org/10.1016/B978-0-12-185271-9.50012-5.

[207] S.H. Grossman, Electrophoresis of creatine kinase: A laboratory experiment in isoenzymes, Biochem. Educ. 10 (1982) 8–10.

[208] M. Herrera, G. León, A. Segura, F. Meneses, B. Lomonte, J.P. Chippaux, J.M. Gutiérrez, Factors associated with adverse reactions induced by caprylic acid-fractionated whole IgG preparations: Comparison between horse, sheep and camel IgGs, Toxicon. 46 (2005) 775–781. https://doi.org/10.1016/j.toxicon.2005.08.004.

[209] M.A. Clauss, R.K. Jain, Interstitial Transport of Rabbit and Sheep Antibodies in Normal and Neoplastic Tissues, Cancer Res. 50 (1990) 3487–3492.

[210] R.J. P. Walstra, Dairy chemistry and physics, John Wiley and Sons, New York, 1984. https://research.wur.nl/en/publications/dairy-chemistry-and-physics (accessed October 10, 2021).

[211] M. Strickland, M.E. Johnson, J.R. Broadbent, Qualitative and quantitative analysis of proteins and peptides in milk products by capillary electrophoresis, Electrophoresis. 22 (2001) 1510–1517. https://doi.org/10.1002/1522-2683(200105)22:8<1510::AID-ELPS1510>3.0.CO;2-4.

[212] J. Zhao, Z. Xu, Capillary electrophoresis with dual C4D/UV detection for simultaneously determining major metal cations and whey proteins in milk, Anal. Methods. 13 (2021) 801–808. https://doi.org/10.1039/d0ay02092c.

[213] W.N. Eigel, J.E. Butler, C.A. Ernstrom, H.M. Farrell, V.R. Harwalkar, R. Jenness, R.M.L. Whitney, Nomenclature of Proteins of Cow's Milk: Fifth Revision, J. Dairy Sci. 67 (1984) 1599–1631. https://doi.org/10.3168/jds.S0022-0302(84)81485-X.

[214] X. Ding, Y. Yang, S. Zhao, Y. Li, Z. Wang, Analysis of α-lactalbumin, β-lactoglobulin A and B in whey protein powder, colostrum, raw milk, and

infant formula by CE and LC, Dairy Sci. Technol. 91 (2011) 213–225. https://doi.org/10.1007/s13594-011-0006-9.

[215] M. Elmaoğlu, A. Çelik, A Brief History of Magnetic Resonance Imaging, in: MRI Handb., Springer US, Boston, MA, 2011: pp. 3–6. https://doi.org/10.1007/978-1-4614-1096-6_1.

[216] J. Lohrke, T. Frenzel, J. Endrikat, F.C. Alves, T.M. Grist, M. Law, J.M. Lee, T. Leiner, K.C. Li, K. Nikolaou, M.R. Prince, H.H. Schild, J.C. Weinreb, K. Yoshikawa, H. Pietsch, 25 Years of Contrast-Enhanced MRI: Developments, Current Challenges and Future Perspectives, Adv. Ther. 33 (2016) 1–28. https://doi.org/10.1007/s12325-015-0275-4.

[217] B.E. Van Beers, C.M. Pastor, H.K. Hussain, Primovist, eovist: What to expect?, J. Hepatol. 57 (2012) 421–429. https://doi.org/10.1016/j.jhep.2012.01.031.

[218] S. Gschwend, W. Ebert, M. Schultze-Mosgau, J. Breuer, Pharmacokinetics and imaging properties of Gd-EOB-DTPA in patients with hepatic and renal impairment, Invest. Radiol. 46 (2011) 556–566. https://doi.org/10.1097/RLI.0b013e31821a218a.

[219] B.E. Van Beers, B. Gallez, J. Pringot, Contrast-enhanced MR imaging of the liver., Radiology. 203 (1997) 297–306. https://doi.org/10.1148/radiology.203.2.9114076.

[220] G. Schuhmann-Giampieri, H. Schmitt-Willich, W.R. Press, C. Negishi, H.J. Weinmann, U. Speck, Preclinical evaluation of Gd-EOB-DTPA as a contrast agent in MR imaging of the hepatobiliary system, Radiology. 183 (1992) 59–64. https://doi.org/10.1148/radiology.183.1.1549695.

[221] M.F. Tweedle, Gadolinium Retention in Human Brain, Bone, and Skin, Radiology. 300 (2021) 570–571. https://doi.org/10.1148/radiol.2021210957.

[222] S. Fingerhut, A.C. Niehoff, M. Sperling, A. Jeibmann, W. Paulus, T. Niederstadt, T. Allkemper, W. Heindel, M. Holling, U. Karst, Spatially resolved quantification of gadolinium deposited in the brain of a patient treated with gadolinium-based contrast agents, J. Trace Elem. Med. Biol. 45 (2018) 125–130. https://doi.org/10.1016/j.jtemb.2017.10.004.

[223] S. Fingerhut, M. Sperling, M. Holling, T. Niederstadt, T. Allkemper, A. Radbruch, W. Heindel, W. Paulus, A. Jeibmann, U. Karst, Gadolinium-based contrast agents induce gadolinium deposits in cerebral vessel walls, while the neuropil is not affected: An autopsy study, Acta Neuropathol. 136 (2018) 127–138. https://doi.org/10.1007/s00401-018-1857-4.

[224] B.R. Duncan, M. Hasegawa, D.A. Marshall, L.F. Gonzalez-Cuyar, M.

Paulsen, M. Kobayashi, K.R. Maravilla, C.D. Simpson, Variability in hair gadolinium concentrations among decedents who received gadolinium-based contrast agents, Anal. Bioanal. Chem. 413 (2021) 1571–1582. https://doi.org/10.1007/s00216-020-03116-3.

[225] M. Hasegawa, B.R. Duncan, D.A. Marshall, L.F. Gonzalez-Cuyar, M. Paulsen, M. Kobayashi, C. Simpson, K.R. Maravilla, Human Hair as a Possible Surrogate Marker of Retained Tissue Gadolinium: A Pilot Autopsy Study Correlating Gadolinium Concentrations in Hair with Brain and Other Tissues among Decedents Who Received Gadolinium-Based Contrast Agents, Invest. Radiol. 55 (2020) 636–642. https://doi.org/10.1097/RLI.0000000000000681.

[226] D. Clases, S. Fingerhut, A. Jeibmann, M. Sperling, P. Doble, U. Karst, LA-ICP-MS/MS improves limits of detection in elemental bioimaging of gadolinium deposition originating from MRI contrast agents in skin and brain tissues, J. Trace Elem. Med. Biol. 51 (2019) 212–218. https://doi.org/10.1016/j.jtemb.2018.10.021.

[227] J. Lohrke, A.L. Frisk, T. Frenzel, L. Schöckel, M. Rosenbruch, G. Jost, D.C. Lenhard, M.A. Sieber, V. Nischwitz, A. Küppers, H. Pietsch, Histology and gadolinium distribution in the rodent brain after the administration of cumulative high doses of linear and macrocyclic gadolinium-based contrast agents, Invest. Radiol. 52 (2017) 324–333. https://doi.org/10.1097/RLI.0000000000000344.

[228] H. Richter, P. Bücker, C. Dunker, U. Karst, P.R. Kircher, Gadolinium deposition in the brain of dogs after multiple intravenous administrations of linear gadolinium based contrast agents, PLoS One. 15 (2020) 1–16. https://doi.org/10.1371/journal.pone.0227649.

[229] Y.O. Uca, D. Hallmann, B. Hesse, C. Seim, N. Stolzenburg, H. Pietsch, J. Schnorr, M. Taupitz, Microdistribution of Magnetic Resonance Imaging Contrast Agents in Atherosclerotic Plaques Determined by LA-ICP-MS and SR-μXRF Imaging, Mol. Imaging Biol. 23 (2021) 382–393. https://doi.org/10.1007/s11307-020-01563-z.

[230] I. Strzeminska, C. Factor, P. Robert, A.L. Grindel, P.O. Comby, J. Szpunar, C. Corot, R. Lobinski, Long-Term Evaluation of Gadolinium Retention in Rat Brain after Single Injection of a Clinically Relevant Dose of Gadolinium-Based Contrast Agents, Invest. Radiol. 55 (2020) 138–143. https://doi.org/10.1097/RLI.0000000000000623.

[231] J. Künnemeyer, L. Terborg, S. Nowak, C. Brauckmann, L. Telgmann, A. Albert, F. Tokmak, B.K. Krämer, A. Günsel, G.A. Wiesmüller, U. Karst, Quantification and excretion kinetics of a magnetic resonance imaging contrast agent by capillary electrophoresis-mass spectrometry, Electrophoresis. 30 (2009) 1766–1773.

https://doi.org/10.1002/elps.200800831.

[232] M. Andrási, A. Gáspár, O. Kovács, Z. Baranyai, Á. Klekner, E. Brücher, Determination of gadolinium-based magnetic resonance imaging contrast agents by micellar electrokinetic capillary chromatography, Electrophoresis. 32 (2011) 2223–2228. https://doi.org/10.1002/elps.201100185.

[233] C. Campa, M. Rossi, A. Flamigni, E. Baiutti, A. Coslovi, L. Calabi, Analysis of gadobenate dimeglumine by capillary zone electrophoresis coupled with electrospray-mass spectrometry, Electrophoresis. 26 (2005) 1533–1540. https://doi.org/10.1002/elps.200410111.

[234] D. Pröfrock, A. Prange, Inductively coupled plasma-mass spectrometry (ICP-MS) for quantitative analysis in environmental and life sciences: A review of challenges, solutions, and trends, Appl. Spectrosc. 66 (2012) 843–868. https://doi.org/10.1366/12-06681.

[235] A. Pereira Navaza, J. Ruiz Encinar, A. Sanz-Medel, Absolute and accurate quantification of protein phosphorylation by using an elemental phosphorus standard and element mass spectrometry, Angew. Chemie - Int. Ed. 46 (2007) 569–571. https://doi.org/10.1002/anie.200602517.

[236] D. Pröfrock, A. Prange, Compensation of gradient related effects when using capillary liquid chromatography and inductively coupled plasma mass spectrometry for the absolute quantification of phosphorylated peptides, J. Chromatogr. A. 1216 (2009) 6706–6715. https://doi.org/10.1016/j.chroma.2009.08.002.

[237] D. Pröfrock, P. Leonhard, A. Prange, Determination of sulfur and selected trace elements in metallothionein-like proteins using capillary electrophoresis hyphenated to inductively coupled plasma mass spectrometry with an octopole reaction cell, Anal. Bioanal. Chem. 377 (2003) 132–139. https://doi.org/10.1007/s00216-003-2041-8.

[238] D. Schaumlöffel, A. Prange, A new interface for combining capillary electrophoresis with inductively coupled plasma-mass spectrometry, Fresenius. J. Anal. Chem. 364 (1999) 452–456. https://doi.org/10.1007/s002160051366.

[239] L. Liu, Z. Yun, B. He, G. Jiang, Efficient interface for online coupling of capillary electrophoresis with inductively coupled plasma-mass spectrometry and its application in simultaneous speciation analysis of arsenic and selenium, Anal. Chem. 86 (2014) 8167–8175. https://doi.org/10.1021/ac501347d.

[240] Y. Zhao, J. Zheng, L. Fang, Q. Lin, Y. Wu, Z. Xue, F. Fu, Speciation analysis of mercury in natural water and fish samples by using capillary

electrophoresis-inductively coupled plasma mass spectrometry, Talanta. 89 (2012) 280–285. https://doi.org/10.1016/j.talanta.2011.12.029.

[241] B. Deng, Y. Wang, P. Zhu, X. Xu, X. Ning, Study of the binding equilibrium between Zn(II) and HSA by capillary electrophoresis-inductively coupled plasma optical emission spectrometry, Anal. Chim. Acta. 683 (2010) 58–62. https://doi.org/10.1016/j.aca.2010.10.018.

[242] S. Leguay, T. Vercouter, S. Topin, J. Aupiais, D. Guillaumont, M. Miguirditchian, P. Moisy, C. Le Naour, New insights into formation of trivalent actinides complexes with DTPA, Inorg. Chem. 51 (2012) 12638–12649. https://doi.org/10.1021/ic3011019.

[243] C. Møller, S. Stürup, H.R. Hansen, B. Gammelgaard, Comparison of two CE-ICP-MS interfaces and quantitative measurements of carboplatin in plasma samples using an internal standard, J. Anal. At. Spectrom. 24 (2009) 1208–1212. https://doi.org/10.1039/b822857d.

[244] D. Profrock, P. Leonhard, A. Prange, Determination of phosphorus in phosphorylated deoxyribonucleotides using capillary electrophoresis and high performance liquid chromatography hyphenated to inductively coupled plasma mass spectrometry with an octopole reaction cell, J. Anal. At. Spectrom. 18 (2003) 708–713. https://doi.org/10.1039/b302445h.

[245] S. ichiro Fujii, K. Inagaki, A. Takatsu, T. Yarita, K. Chiba, Determination of phosphorus using capillary electrophoresis and micro-high-performance liquid chromatography hyphenated with inductively coupled plasma mass spectrometry for the quantification of nucleotides, J. Chromatogr. A. 1216 (2009) 7488–7492. https://doi.org/10.1016/j.chroma.2009.05.019.

[246] M.W. Yang, W.H. Wu, Y.J. Ruan, L.M. Huang, Z. Wu, Y. Cai, F.F. Fu, Ultra-sensitive quantification of lysozyme based on element chelate labeling and capillary electrophoresis-inductively coupled plasma mass spectrometry, Anal. Chim. Acta. 812 (2014) 12–17. https://doi.org/10.1016/j.aca.2014.01.003.

[247] K. Shigeta, K. Sato, N. Furuta, Determination of selenoprotein P in submicrolitre samples of human plasma using micro-affinity chromatography coupled with low flow ICP-MS, J. Anal. At. Spectrom. 22 (2007) 911–916. https://doi.org/10.1039/b701206c.

[248] J. Davies, P. Siebenhandl-Wolff, F. Tranquart, P. Jones, P. Evans, Gadolinium: pharmacokinetics and toxicity in humans and laboratory animals following contrast agent administration, Arch. Toxicol. 96 (2022) 403–429. https://doi.org/10.1007/s00204-021-03189-8.

[249] S. Mounicou, J. Szpunar, R. Lobinski, Metallomics: The concept and methodology, Chem. Soc. Rev. 38 (2009) 1119–1138.

https://doi.org/10.1039/b713633c.

[250] X. Lou, G. Zhang, I. Herrera, R. Kinach, O. Ornatsky, V. Baranov, M. Nitz, M.A. Winnik, Polymer-based elemental tags for sensitive bioassays, Angew. Chemie - Int. Ed. 46 (2007) 6111–6114. https://doi.org/10.1002/anie.200700796.

[251] C. Zhang, F. Wu, Y. Zhang, X. Wang, X. Zhang, A novel combination of immunoreaction and ICP-MS as a hyphenated technique for the determination of thyroid-stimulating hormone (TSH) in human serum, J. Anal. At. Spectrom. 16 (2001) 1393–1396. https://doi.org/10.1039/b106387c.

[252] C. Zhang, Z. Zhang, B. Yu, J. Shi, X. Zhang, Application of the biological conjugate between antibody and colloid Au nanoparticles as analyte to inductively coupled plasma mass spectrometry, Anal. Chem. 74 (2002) 96–99. https://doi.org/10.1021/ac0103468.

[253] G. Schwarz, L. Mueller, S. Beck, M.W. Linscheid, DOTA based metal labels for protein quantification: A review, J. Anal. At. Spectrom. 29 (2014) 221–233. https://doi.org/10.1039/c3ja50277e.

[254] M.L. Chiu, D.R. Goulet, A. Teplyakov, G.L. Gilliland, Antibody Structure and Function: The Basis for Engineering Therapeutics, Antibodies. 8 (2019) 55. https://doi.org/10.3390/antib8040055.

[255] D. Majonis, O. Ornatsky, R. Kinach, M.A. Winnik, Curious results with palladium- and platinum-carrying polymers in mass cytometry bioassays and an unexpected application as a dead cell stain, Biomacromolecules. 12 (2011) 3997–4010. https://doi.org/10.1021/bm201011t.

[256] D. Clases, R. Gonzalez de Vega, D. Bishop, P. Doble, SEC-ICP-MS and on-line isotope dilution analysis for characterisation and quantification of immunochemical assays, Anal. Bioanal. Chem. 411 (2019) 3553–3560. https://doi.org/10.1007/s00216-019-01836-9.

[257] A. El-Sayed, M. Kamel, Advances in nanomedical applications: diagnostic, therapeutic, immunization, and vaccine production, Environ. Sci. Pollut. Res. 27 (2020) 19200–19213. https://doi.org/10.1007/s11356-019-06459-2.

[258] A. Juan, F.J. Cimas, I. Bravo, A. Pandiella, A. Ocaña, C. Alonso-Moreno, An overview of antibody conjugated polymeric nanoparticles for breast cancer therapy, Pharmaceutics. 12 (2020) 1–20. https://doi.org/10.3390/pharmaceutics12090802.

[259] M. Tallawi, E. Rosellini, N. Barbani, M. Grazia Cascone, R. Rai, G. Saint-Pierre, A.R. Boccaccini, Strategies for the chemical and biological

functionalization of scaffolds for cardiac tissue engineering: A review, J. R. Soc. Interface. 12 (2015). https://doi.org/10.1098/rsif.2015.0254.

[260] A.C. Marques, P.J. Costa, S. Velho, M.H. Amaral, Functionalizing nanoparticles with cancer-targeting antibodies: A comparison of strategies, J. Control. Release. 320 (2020) 180–200. https://doi.org/10.1016/j.jconrel.2020.01.035.

[261] X. Lin, A. O'Reilly Beringhs, X. Lu, Applications of Nanoparticle-Antibody Conjugates in Immunoassays and Tumor Imaging, AAPS J. 23 (2021). https://doi.org/10.1208/s12248-021-00561-5.

[262] L. Mueller, T. Mairinger, G. Hermann, G. Koellensperger, S. Hann, Characterization of metal-tagged antibodies used in ICP-MS-based immunoassays, Anal. Bioanal. Chem. 406 (2014) 163–169. https://doi.org/10.1007/s00216-013-7416-x.

[263] T. Mairinger, G. Wozniak-Knopp, F. Rüker, G. Koellensperger, S. Hann, Element labeling of antibody fragments for ICP-MS based immunoassays, J. Anal. At. Spectrom. 31 (2016) 2330–2337. https://doi.org/10.1039/c6ja00252h.

[264] J.F. Pérez, J. Llanos, C. Sáez, C. López, P. Cañizares, M.A. Rodrigo, Electrochemical jet-cell for the in-situ generation of hydrogen peroxide, Electrochem. Commun. 71 (2016) 65–68. https://doi.org/10.1016/j.elecom.2016.08.007.

[265] J. Kunze, I. Burgess, R. Nichols, C. Buess-Herman, J. Lipkowski, Electrochemical evaluation of citrate adsorption on Au(111) and the stability of citrate-reduced gold colloids, J. Electroanal. Chem. 599 (2007) 147–159. https://doi.org/10.1016/j.jelechem.2005.12.020.

[266] T. O'Haver, P. Emeritus, Pragmatic Introduction to Signal Processing: Applications in scientific measurement, Maryland, 2022.

[267] Philip D. Anderson, Method of improving signal-to-noise in electropherogram, 5098536, 1992.

[268] L.A. Kolahalam, I. V. Kasi Viswanath, B.S. Diwakar, B. Govindh, V. Reddy, Y.L.N. Murthy, Review on nanomaterials: Synthesis and applications, Mater. Today Proc. 18 (2019) 2182–2190. https://doi.org/10.1016/J.MATPR.2019.07.371.

[269] J. Gao, B. Xu, Applications of nanomaterials inside cells, Nano Today. 4 (2009) 37–51. https://doi.org/10.1016/J.NANTOD.2008.10.009.

[270] A. Fernandez-Fernandez, R. Manchanda, A.J. McGoron, Theranostic applications of nanomaterials in cancer: Drug delivery, image-guided therapy, and multifunctional platforms, Appl. Biochem. Biotechnol. 165

(2011) 1628–1651. https://doi.org/10.1007/S12010-011-9383-Z.

[271] J. Jeevanandam, A. Barhoum, Y.S. Chan, A. Dufresne, M.K. Danquah, Review on nanoparticles and nanostructured materials: History, sources, toxicity and regulations, Beilstein J. Nanotechnol. 9 (2018) 1050–1074. https://doi.org/10.3762/BJNANO.9.98.

[272] S. Mourdikoudis, R.M. Pallares, N.T.K. Thanh, Characterization techniques for nanoparticles: Comparison and complementarity upon studying nanoparticle properties, Nanoscale. 10 (2018) 12871–12934. https://doi.org/10.1039/C8NR02278J.

[273] Z. Du, A. Gupta, C. Clarke, M. Cappadona, D. Clases, D. Liu, Z. Yang, S. Karan, W.S. Price, X. Xu, Porous Upconversion Nanostructures as Bimodal Biomedical Imaging Contrast Agents, J. Phys. Chem. C. 124 (2020) 12168–12174. https://doi.org/10.1021/acs.jpcc.0c03945.

[274] Y. Liu, F. Wang, H. Lu, G. Fang, S. Wen, C. Chen, X. Shan, X. Xu, L. Zhang, M. Stenzel, D. Jin, Super-Resolution Mapping of Single Nanoparticles inside Tumor Spheroids, Small. 16 (2020) 1–6. https://doi.org/10.1002/smll.201905572.

[275] J. Zhou, Y. Sun, X. Du, L. Xiong, H. Hu, F. Li, Dual-modality in vivo imaging using rare-earth nanocrystals with near-infrared to near-infrared (NIR-to-NIR) upconversion luminescence and magnetic resonance properties, Biomaterials. 31 (2010) 3287–3295. https://doi.org/10.1016/j.biomaterials.2010.01.040.

[276] D. Ma, Y. Shen, T. Su, J. Zhao, N.U. Rahman, Z. Xie, F. Shi, S. Zheng, Y. Zhang, Z. Chi, Performance enhancement in up-conversion nanoparticle-embedded perovskite solar cells by harvesting near-infrared sunlight, Mater. Chem. Front. 3 (2019) 2058–2065. https://doi.org/10.1039/C9QM00311H.

[277] S. Hao, Y. Shang, D. Li, H. Ågren, C. Yang, G. Chen, Enhancing dye-sensitized solar cell efficiency through broadband near-infrared upconverting nanoparticles, Nanoscale. 9 (2017) 6711–6715. https://doi.org/10.1039/C7NR01008G.

[278] A.N. Generalova, B.N. Chichkov, E. V. Khaydukov, Multicomponent nanocrystals with anti-Stokes luminescence as contrast agents for modern imaging techniques, Adv. Colloid Interface Sci. 245 (2017) 1–19. https://doi.org/10.1016/J.CIS.2017.05.006.

[279] M. Wang, G. Abbineni, A. Clevenger, C. Mao, S. Xu, Upconversion nanoparticles: Synthesis, surface modification and biological applications, Nanomedicine Nanotechnology, Biol. Med. 7 (2011) 710–729. https://doi.org/10.1016/J.NANO.2011.02.013.

[280] Y. Liu, Y. Lu, X. Yang, X. Zheng, S. Wen, F. Wang, X. Vidal, J. Zhao, D. Liu, Z. Zhou, C. Ma, J. Zhou, J.A. Piper, P. Xi, D. Jin, Amplified stimulated emission in upconversion nanoparticles for super-resolution nanoscopy, Nature. 543 (2017) 229–233. https://doi.org/10.1038/NATURE21366.

[281] G. Chen, H. Qiu, P.N. Prasad, X. Chen, Upconversion nanoparticles: Design, nanochemistry, and applications in Theranostics, Chem. Rev. 114 (2014) 5161–5214. https://doi.org/10.1021/CR400425H.

[282] X. Li, F. Zhang, D. Zhao, Lab on upconversion nanoparticles: Optical properties and applications engineering via designed nanostructure, Chem. Soc. Rev. 44 (2015) 1346–1378. https://doi.org/10.1039/C4CS00163J.

[283] A. Gee, X. Xu, Surface Functionalisation of Upconversion Nanoparticles with Different Moieties for Biomedical Applications, Surfaces. 1 (2018) 96–121. https://doi.org/10.3390/SURFACES1010009.

[284] D. Clases, M. Sperling, U. Karst, Analysis of metal-based contrast agents in medicine and the environment, TrAC Trends Anal. Chem. 104 (2018) 135–147. https://doi.org/10.1016/j.trac.2017.12.011.

[285] J. Soto-Alvaredo, M. Montes-Bayón, J. Bettmer, Speciation of silver nanoparticles and silver(I) by reversed-phase liquid chromatography coupled to ICPMS, Anal. Chem. 85 (2013) 1316–1321. https://doi.org/10.1021/AC302851D.

[286] B. Meermann, V. Nischwitz, ICP-MS for the analysis at the nanoscale-a tutorial review, J. Anal. At. Spectrom. 33 (2018) 1432–1468. https://doi.org/10.1039/C8JA00037A.

[287] D. Metarapi, M. Šala, K. Vogel-Mikuš, V.S. Šelih, J.T. van Elteren, Nanoparticle Analysis in Biomaterials Using Laser Ablation−Single Particle−Inductively Coupled Plasma Mass Spectrometry, Anal. Chem. 91 (2019) 6200–6205. https://doi.org/10.1021/acs.analchem.9b00853.

[288] D. Mozhayeva, C. Engelhard, Separation of Silver Nanoparticles with Different Coatings by Capillary Electrophoresis Coupled to ICP-MS in Single Particle Mode, Anal. Chem. 89 (2017) 9767–9774. https://doi.org/10.1021/acs.analchem.7b01626.

[289] C.A. Sötebier, D.J. Kutscher, L. Rottmann, N. Jakubowski, U. Panne, J. Bettmer, Combination of single particle ICP-QMS and isotope dilution analysis for the determination of size, particle number and number size distribution of silver nanoparticles, J. Anal. At. Spectrom. 31 (2016) 2045–2052. https://doi.org/10.1039/C6JA00137H.

[290] J. Tuoriniemi, G. Cornelis, M. Hassellöv, A new peak recognition algorithm for detection of ultra-small nano-particles by single particle ICP-MS using

rapid time resolved data acquisition on a sector-field mass spectrometer, J. Anal. At. Spectrom. 30 (2015) 1723–1729. https://doi.org/10.1039/C5JA00113G.

[291] R. Peters, Z. Herrera-Rivera, A. Undas, M. Van Der Lee, H. Marvin, H. Bouwmeester, S. Weigel, Single particle ICP-MS combined with a data evaluation tool as a routine technique for the analysis of nanoparticles in complex matrices, J. Anal. At. Spectrom. 30 (2015) 1274–1285. https://doi.org/10.1039/C4JA00357H.

[292] D. Mozhayeva, C. Engelhard, A quantitative nanoparticle extraction method for microsecond time resolved single-particle ICP-MS data in the presence of a high background, J. Anal. At. Spectrom. 34 (2019) 1571–1580. https://doi.org/10.1039/C9JA00042A.

[293] L. Fréchette-Viens, M. Hadioui, K.J. Wilkinson, Quantification of ZnO nanoparticles and other Zn containing colloids in natural waters using a high sensitivity single particle ICP-MS, Talanta. 200 (2019) 156–162. https://doi.org/10.1016/j.talanta.2019.03.041.

[294] D. Liu, X. Xu, Y. Du, X. Qin, Y. Zhang, C. Ma, S. Wen, W. Ren, E.M. Goldys, J.A. Piper, S. Dou, X. Liu, D. Jin, Three-dimensional controlled growth of monodisperse sub-50 nm heterogeneous nanocrystals, Nat. Commun. 7 (2016) 10254. https://doi.org/10.1038/ncomms10254.

[295] C. Ma, X. Xu, F. Wang, Z. Zhou, S. Wen, D. Liu, J. Fang, C.I. Lang, D. Jin, Probing the Interior Crystal Quality in the Development of More Efficient and Smaller Upconversion Nanoparticles, J. Phys. Chem. Lett. 7 (2016) 3252–3258. https://doi.org/10.1021/acs.jpclett.6b01434.

[296] F. Wang, R. Deng, X. Liu, Preparation of core-shell NaGdF4 nanoparticles doped with luminescent lanthanide ions to be used as upconversion-based probes, Nat. Protoc. 9 (2014) 1634–1644. https://doi.org/10.1038/nprot.2014.111.

[297] L.E. Mackenzie, J.A. Goode, A. Vakurov, P.P. Nampi, S. Saha, G. Jose, P.A. Millner, The theoretical molecular weight of NaYF 4 :RE upconversion nanoparticles, Sci. Rep. 8 (2018) 1–11. https://doi.org/10.1038/s41598-018-19415-w.

[298] S. Lee, X. Bi, R.B. Reed, J.F. Ranville, P. Herckes, P. Westerhoff, Nanoparticle size detection limits by single particle ICP-MS for 40 elements, Environ. Sci. Technol. 48 (2014) 10291–10300. https://doi.org/10.1021/es502422v.

[299] H.E. Pace, N.J. Rogers, C. Jarolimek, V.A. Coleman, C.P. Higgins, J.F. Ranville, Determining Transport Efficiency for the Purpose of Counting and Sizing Nanoparticles via Single Particle Inductively Coupled Plasma Mass

Spectrometry, Anal. Chem. 83 (2011) 9361–9369. https://doi.org/10.1021/ac201952t.

[300] D. Clases, M. Ueland, R. Gonzalez de Vega, P. Doble, D. Pröfrock, Quantitative speciation of volatile sulphur compounds from human cadavers by GC-ICP-MS, Talanta. 221 (2021). https://doi.org/10.1016/J.TALANTA.2020.121424.

[301] A. González-Gago, D. Pröfrock, A. Prange, Optimizing GC-ICP-MS for ultra-trace quantification of PBDEs in natural water samples using species-specific isotope dilution, J. Anal. At. Spectrom. 30 (2015) 180–190. https://doi.org/10.1039/C4JA00112E.

[302] K.L. Linge, K.E. Jarvis, Quadrupole ICP-MS: Introduction to instrumentation, measurement techniques and analytical capabilities, Geostand. Geoanalytical Res. 33 (2009) 445–467. https://doi.org/10.1111/J.1751-908X.2009.00039.X.

[303] J.W. Olesik, P.J. Gray, Considerations for measurement of individual nanoparticles or microparticles by ICP-MS: Determination of the number of particles and the analyte mass in each particle, J. Anal. At. Spectrom. 27 (2012) 1143–1155. https://doi.org/10.1039/C2JA30073G.

[304] R.L. Siegel, K.D. Miller, A. Jemal, Cancer statistics, 2019., CA. Cancer J. Clin. 69 (2019) 7–34. https://doi.org/10.3322/caac.21551.

[305] W.H. Organisation, World Health Statistics 2018: Monitoring health for the SDGs, World Health Organization, 2018. https://www.who.int/data/gho/publications/world-health-statistics (accessed June 27, 2019).

[306] V.I. Baranov, Z. Quinn, D.R. Bandura, S.D. Tanner, A sensitive and quantitative element-tagged immunoassay with ICPMS detection, Anal. Chem. 74 (2002) 1629–1636. https://doi.org/10.1021/ac0110350.

[307] C. Giesen, T. Mairinger, L. Khoury, L. Waentig, N. Jakubowski, U. Panne, Multiplexed Immunohistochemical Detection of Tumor Markers in Mass Spectrometry, Anal. Chem. 83 (2011) 8177–8183.

[308] M.T. Westerhausen, T.E. Lockwood, R. Gonzalez De Vega, A. Röhnelt, D.P. Bishop, N. Cole, P.A. Doble, D. Clases, Low background mould-prepared gelatine standards for reproducible quantification in elemental bio-imaging, Analyst. 144 (2019) 6881–6888. https://doi.org/10.1039/c9an01580a.

[309] D. Clases, R. Gonzalez de Vega, D. Bishop, P. Doble, SEC-ICP-MS and on-line isotope dilution analysis for characterisation and quantification of immunochemical assays, Anal. Bioanal. Chem. (2019).

https://doi.org/10.1007/s00216-019-01836-9.

[310] T.E. Lockwood, R. Gonzalez De Vega, D. Clases, An interactive Python-based data processing platform for single particle and single cell ICP-MS, J. Anal. At. Spectrom. 36 (2021) 2536–2544. https://doi.org/10.1039/d1ja00297j.